The Dissertation Committee for Qiang Xu Certifies that this is the approved version of the following dissertation:

THEORETICAL AND EXPERIMENTAL STUDY OF FOAM FOR ENHANCED OIL RECOVERY AND ACID DIVERSION

Committee:

William. R. Rossen, Supervisor

Mukul M. Sharma

Kamy Sepehrnoori

Russell T. Johns

Roger T. Bonnecaze

THEORETICAL AND EXPERIMENTAL STUDY OF FOAM FOR ENHANCED OIL RECOVERY AND ACID DIVERSION

by

Qiang Xu, B.S., M. S.

Dissertation

Presented to the Faculty of the Graduate School of
The University of Texas at Austin
in Partial Fulfillment
of the Requirements
for the Degree of

Doctor of Philosophy

The University of Texas at Austin
May 2003

Dedication

To my wife

Xinxia Wu;

also to our son Simon Xu and our parents

Acknowledgements

It has been my great pleasure to be supervised by Dr. William R. Rossen during my stay at the University of Texas at Austin. I like to thank Dr. Rossen for his guidance and help in this research, I am grateful for the advices, discussions, and support he offered me throughout these years. My work reflects his vast knowledge and experience of foams.

I would also like to thank the faculty and staffs in the Department, especially Dr. Gray and Dr. Peters for their excellent teaching and helps. My thanks also go to Tony Bermudez, Glen Baum, Bob Savicki, and Roger, Terzian. Their help were essential in performing my researches successfully.

I want to thank my fellow students, Seung Ihl Kam, Jiann Gwo Rong for the helps they offered me especially at the start of my laboratory experiments.

THEORETICAL AND EXPERIMENTAL STUDY OF FOAM FOR ENHANCED OIL RECOVERY AND ACID DIVERSION

Publication No._____________

Qiang Xu, Ph. D
The University of Texas at Austin, 2003

Supervisor: William R. Rossen

This dissertation comprises three studies of foam in porous media. The first study is a theoretical model for apparent viscosity of foam in porous media. This represents the first dynamic model for the movement of bubbles through constricted tubes in 2D, accounting for the drag on lamellae (soap films) along pore walls and the capillary forces that govern bubble shape in constricted tubes. At low velocities behavior fits earlier quasi-static and approximate models. At higher velocities, behavior is complex; for instance, pressure gradient can decrease with increasing bubble velocity. This work could provide a component to a fully mechanistic foam simulator.

The second study is an experimental investigation of SAG foam processes for enhanced oil recovery, where gas and surfactant solution are injected in alternating slugs. Experimental fractional-flow curves are presented for two surfactant formulations in Berea sandstone, with no oil present. Results are then scaled-up using fractional-flow theory to a hypothetical 1D field-scale application. In one case the data suggest an abrupt jump from a strong-foam fractional-flow curve to a weaker-foam curve, as has been reported elsewhere. In both cases the data suggest successful mobility control on the field scale.

The third study is an experimental investigation of post-foam liquid injection, which is the key to the success of foam-acid diversion for matrix-acid well stimulation. Results indicate that with high foam quality pressure gradient can be higher during liquid injection than during foam injection; this may require reconsideration of the optimal foam quality for foam-acid diversion. It appears that the water relative-permeability function obtained during foam injection also applies to liquid injection after foam, until trapped gas begins to dissolve into injected liquid. The extent of gas trapping and liquid mobility after foam varied with foam quality here, which means earlier models that exclude this effect may need to be revised.

In both experimental studies, pressure gradient was monitored along the core and liquid saturation was determined by weighing the core continuously during the experiment. Strengths and shortcomings of this technique for determining water saturation are discussed, along with suggestions for improving the technique.

Table of Contents

List of Tables

List of Figures

Chapter 1: Introduction

1.1 APPLICATIONS OF FOAMS IN PETROLEUM ENGINEERING

Foams are widely used in many different ways in the petroleum industry. Bulk foams are used in under-balanced drilling, cementing, and fracturing operations (Scott *et al.*, 1995; Techrob and Manuel, 1997; Picket and Cole, 1994; Toney and Mack, 1991; Harris, 1992). Foams are injected directly into the formation in enhanced oil recovery (EOR) and near-well treatments. These latter two applications of foams are the subjects of this work.

1.1.1 Foams in EOR

EOR, primarily by means of steam and carbon dioxide, contributes 700,000 b/d or about 9% (calculated based on data in BP statistical review of world energy 2002) to the US total oil production in 2002 (Moritis, 2002). Both steam and carbon dioxide can be very efficient in displacing oil it contacts. However, due to high gas mobility, reservoir heterogeneity, and gravity segregation, early break-through of gas often occurs, and injected gas often sweeps only a small part of the reservoir (Lake, 1989).

Foam directly addresses the problem of high gas mobility in porous media. Injected foam appears to be a much more viscous fluid, which helps increase sweep efficiency. The decrease in gas mobility also indirectly reduces gravity segregation, if injection-well pressure can be increased (Shi and Rossen, 1998; Shan and Rossen, 2002).

Poor sweep efficiency caused by reservoir heterogeneity can also be reduced by using foams, thus increasing sweep efficiency. Foams are stronger (with higher apparent viscosity) in high-permeability layers compared to lower-permeability layers (Hirasaki, 1989; Rossen, 1996). This feature helps to divert injected flow into lower-permeability layers.

Different foam-injection strategies have been used in field trials due to stratigraphic differences, foam behavior and operational concerns (Holm, 1969; Chad *et al.*, 1988; Liu and Besserer, 1988; Jonas *et al.*, 1988; Kuehne *et al.*, 1990; Chou *et al.*, 1992; Krause *et al.*, 1992; Hoefner *et al.*, 1994; Aarra *et al.*, 1995; Martin *et al.*, 1995; Svorstol *et al.*, 1996; Blaker *et al.*, 1999, 2002; Aarra *et al.*, 2002). Among these field trials, some used co-injection of surfactant solution and gas, while others used surfactant-alternating-gas (SAG).

In a SAG process, slugs of surfactant and slugs of gas are injected alternately into the reservoir. During the injection of gas, the near-well region gets extremely dry, and foam weakens or even collapses. The success of a SAG process may hinge on foam behavior under these dry conditions as discussed in Chapter 4. Chapter 4 introduces experimental work on SAG processes and a fractional-flow analysis for scale-up of laboratory results. The experimental work suggests a method for evaluating SAG processes in the laboratory. Experimental results suggest a successful hypothetical SAG process at field scale under the experimental conditions.

1.1.2 Foams in near-well treatments

Foams have been used to control gas-oil ratio (GOR) in some oil-production wells (Chukwueke, 1998; Ligthelm, *et al.*, 2000). High GOR occurs due to an expanding gas cap or to coning, which causes gas to invade the production zone. To promote oil production, foam can be placed near the well to block gas inflow. In Ligthelm *et al.* (2000), gas effective relative permeability in the field was reduced by a factor of 2 to10 times by foam treatment in the gas-bearing zone. In the oil-bearing zone, injected foam was back-produced, and oil production resumed.

In matrix acidizing, one problem is that the acid flows into undamaged and high-permeability zones and leaves more-damaged and lower-permeability zones under-treated or even untreated. Foams have been used to divert acid into damaged zones (Smith *et al.*, 1969; Kennedy *et al.*, 1992; Bernardiner *et al.*, 1992; Gdanski, 1993; Thompson and Gdanski, 1993; Zerhboub *et al.*, 1994; Robert and Rossen, 1997; Thomas *et al.*, 1998). In studies of foam for acid diversion, it is customary to conduct experiments on lower- and higher-permeability undamaged rock (see references just cited) and assume that foam behaves in lower-permeability rock as it would in damaged rock. With foam, the high-permeability zone has higher resistance to flow and thus acid can be diverted into the low-permeability zone where it is needed the most.

The success of acid diversion hinges on trapping a large amount of gas in place during foam and acid injection (Kibodeaux *et al.*, 1994). Gas trapping during post-foam liquid injection is the key to the success of the process.

However, it is an issue that is not fully understood. An experimental study on post-foam liquid injection is described in Chapter 5.

1.2 FOAM IN POROUS MEDIA

1.2.1 Microscopic view of foam in porous media

Foam bubbles in porous media normally are as large, or larger than, the individual pores. If bubbles smaller than pores existed, the smaller bubbles would merge rapidly into larger ones, due to gas diffusion, until remaining bubbles were as large as pores (Rossen, 1996; Rossen and Wang, 1999). The liquid films separating gas phase and forming gas bubbles in porous media are called lamellae. Larger bubbles correspond to fewer lamellae per unit length in porous media, and vice versa.

In water-wet porous media, water occupies the smaller pores, and gas occupies the larger pores, with or without foam. During foam flow, however, only a fraction of gas flows (Gillis and Radke, 1990; Friedmann *et al.*, 1991). Most gas stays trapped even during foam "flow" (Figure 1.1). A minimum pressure gradient is required to mobilize foam lamellae. The minimum mobilization pressure gradient depends on bubble size, pore geometry and surface tension (Falls *et al.*, 1989; Rossen 1990a,b,c,d). At higher pressure gradient, a larger percentage of gas can be mobilized (Falls *et al.*, 1989; Cheng *et al.*, 2002). Many experimental studies (Bernard *et al.*, 1965; Friedmann and Jensen, 1986; Huh and Handy, 1989; Sanchez and Schechter, 1989; de Vries and Wit, 1990; Friedmann *et al.*, 1991) find that foam doesn't alter the water relative-permeability function, $k_{rw}(S_w)$. Water, as the wetting phase, occupies and flows in relatively small pores regardless of the existence or strength of foam. However, gas mobility is greatly altered by foam in complex ways. Gas mobility depends in particular on bubble size: the smaller are the bubbles, the lower is the gas mobility. Bubble size in turn is the product of ongoing processes of creation and destruction of lamellae.

As shown in Figure 1.1, flowing foam bubbles, each at least as large as a pore, form bubble trains through regions of trapped gas. The apparent viscosity of a bubble train in a straight capillary tube has been investigated in many studies (Bretherton, 1961; Hirasaki and Lawson, 1985; Ratulowski and Chang, 1989, Wong *et al*., 1995). However, a straight capillary doesn't capture the complex geometry of pores along a bubble train. Bubbles flowing in a periodically constricted tube is investigated in Rossen (1990 a,b,c,d) in the quasi-static limit. Based on these studies, a numerical approach coupling bubble flow viscosity and the effects of constrictions has been developed, and is introduced in Chapter 2.

1.2.2 Gas mobility with foam

Foam greatly reduces gas mobility. Foam can reduces gas mobility by a factor higher than 10,000 in the laboratory (Zhou and Rossen, 1995); foam reduces gas mobility by a much smaller factor in field applications (Ligthelm *et al*., 2000). Bubble size, flow rates, the presence of oil, reservoir temperature, surfactant formulation, rock type, reservoir heterogeneity, surfactant adsorption into rock, etc., all can affect foam behavior at reservoir conditions. Therefore, foam reduces gas mobility by different degrees, which is measured by a mobility reduction factor, or, equivalently, by an apparent viscosity. Foams with large reduction in gas mobility are referred to as strong foams, and foams with a small reduction in gas mobility are referred to as weak foams. There is no universal, clear-cut distinction between “strong” and “weak” foam in the literature, and, moreover, different authors use the terms in different ways. Nevertheless, the distinction between “strong” foam and “weak” or “coarse” foam is useful, even if a little ambiguous.

1.2.3 Foam regimes

Gauglitz *et al.* (2002) and Kam and Rossen (2002) investigate foam generation in porous media. They find foams exist in three regimes, depending on applied pressure gradient. The three regimes (Figure 1.2) are the strong-foam regime at high pressure gradient, the coarse-foam regime at low pressure gradient and at intermediate pressure gradient the transient-foam regime. The strong-foam regime comprises a high-quality strong-foam regime, and a low-quality strong foam regime, discussed further in the next section. The coarse-foam regime is characterized by low pressure gradient and relatively high gas mobility. The intermediate transient-foam regime appears to be inherently unstable. The remainder of this dissertation concerns the strong-foam regime.

1.2.4 Strong-foam rheology

Khatib *et al*. (1988) report that foam stability in porous media is limited by capillary pressure. In their study with bead-packs, they find an abrupt transition from strong foam to no foam (or weak foam) occurring in a very narrow range of capillary pressure, which they call the "limiting capillary pressure". That is, as foam quality increases, foam gradually coarsens and gas mobility rises, but capillary pressure and water saturation stay fixed. For P_c below the limiting capillary pressure, foam is strong and gas mobility low. For P_c above the limiting value, foam is much weaker and gas mobility much higher. The limiting capillary pressure is denoted P_c^*, and the limiting capillary pressure model is also referred to as the fixed-P_c^* model. The water saturation corresponding to P_c^* is denoted S_w^*.

Experimental findings of Osterloh & Jante (1992) indicate that steady-state strong-foam behavior falls in two flow regimes (Figure 1.3). In the high-quality regime, pressure gradient depends only upon liquid volumetric flux. High-quality foam is a foam with high gas volume fraction, and low-quality foam is a foam with low gas volume fraction. The high-quality regime corresponds to foam at the limiting capillary pressure, and water saturation doesn't change (or doesn't change much) in this regime. Capillary pressure controls the high-quality regime as follows. Lamella stability is especially sensitive to capillary pressure at P_c^*. If P_c rises above P_c^*, many lamellae break, gas mobility rises, gas saturation falls, and P_c falls back to P_c^*. If P_c falls below P_c^*, the reverse occurs: lamellae are more stable and fewer break; gas mobility falls, and gas saturation and P_c rise.

In the low-quality regime, pressure gradient depends only upon gas volumetric flux. Bubble sizes are thought to be fixed (Rossen and Wang, 1999;

Alvarez *et al.*, 2001) and pressure gradient is controlled by gas trapping and mobilization.

Other experiments conducted with various surfactants, porous media, and gases confirm the existence and generality of these two strong-foam regimes (Parlar *et al.*1995; Robert and Mack 1995; Rossen and Wang 1999; Alvarez *et al.*, 1999; Rong, 2002).

1.3 FOAM MODELS

1.3.1 The population-balance model

There is a variety of empirical and theoretical foam models in the literature (Marfoe and Kazemi, 1987; Falls *et al.*, 1988; Islam and Farouq Ali, 1990; Fisher *et al.*, 1990; Friedmann *et al.*, 1991; Kovscek and Radke, 1993; Chou, 1995; Robert and Mack, 1995; Zhou and Rossen, 1995; Kovscek *et al.*, 1995; Bertin *et al.*, 1998; Myers and Radke, 1999; Rossen *et al.*, 1999; Cheng *et al.*, 2000, 2002). Among these models, the population-balance model (Falls *et al.*, 1988; Friedmann *et al.*, 1991; Kovscek and Radke, 1994; Kovscek *et al.*, 1995, 1997; Bertin *et al.*, 1998; Myers and Radke, 1999) provides, in principle, a framework for complete description of foam behavior. Effects of gas mobility are attributed to two separate parts: effective gas permeability and effective gas viscosity. The effective gas relative permeability accounts for gas trapping, which blocks many gas-flow channels in the porous medium. The effective gas viscosity accounts for the resistance of lamellae to the movement of bubbles that do move.

The ability of foam to trap gas in place can be represented as an effective yield stress. Foam can be mobilized only when pressure gradient or shear stress is higher than a minimal value, called a yield stress. Separation of mobility into effective viscosity and permeability is ambiguous for a fluid with a yield stress. Rossen and Zhou (1994) demonstrate that

> The yield stress both governs the trapping of fluid in a portion of the medium and strongly affects the rheology of the fluid. Thus the relative permeability and viscosity are inextricably intertwined.

Besides modeling gas mobility, the population-balance model tracks the evolution of bubble size through a conservation equation for number of lamellae. In the equation, bubble density depends on the rate of influx, efflux, creation, destruction and trapping of lamellae. Including all these parameters, there are as many as 11 parameters in the foam portion of the population-balance model. The complexity of this model has led to the development of simpler alternatives.

1.3.2 The fractional-flow foam model

Zhou and Rossen (1994) first adapted fractional-flow theory to foam displacements. Hill and Rossen (1994), Zeilinger *et al.* (1995), Zhou and Rossen (1995), Kibodeaux and Rossen (1997), and Shan and Rossen (2002) extend the fractional-flow model for foam. Fractional-flow theory is simple, yet still captures the key features in a foam displacement. Rossen *et al.* (1999) shows that fractional-flow modeling does almost as good fitting coreflood data as the population-balance model.

Fraction-flow theory assumes incompressible phases; immediate attainment of local steady state; no chemical reaction, chemical dispersion, or capillary dispersion in the displacement; and Newtonian rheology. Fractional-flow theory is also restricted to one-dimensional displacements. Due to the complexity of foam flow and the simplifying assumptions in fractional-flow theory, the fractional-flow method is a qualitative approach rather than a quantitative means of foam-flow modeling. It is extremely valuable for revealing the key mechanisms in a complex process, such as a population-balance simulation, however (Rossen *et al.*, 1999; Shan and Rossen, 2002).

Using fractional-flow theory for a foam displacement requires first obtaining a fractional-flow curve. Then one can determine the displacement pattern from this fractional-flow curve by constructing a time-distance diagram. Kibodeaux and Rossen (1997) show how to construct a fractional-flow curve from coreflood data. This approach is refined and applied to SAG foam processes in Chapter 4.

1.4 ORGANIZATION OF THE DISSERTATION

This dissertation employs two very different approaches to understanding and designing successful foam field applications.

Chapter 2 describes a numerical approach coupling bubble-flow viscosity and the effects of constrictions to represent the rheology of flowing foam. These results would form but one component of a much larger effort toward fully mechanistic population-balance modeling of foam.

The next three chapters describe two experimental studies of two specific foam applications.

Chapter 3 introduces the experimental apparatus and general procedures used in the SAG-process and gas-trapping experiments described in later chapters.

Chapter 4 describes our experimental study of the SAG foam process for EOR.

Chapter 5 describes our experiments and results regarding post-foam liquid injection, which is a key process in foam acid-diversion.

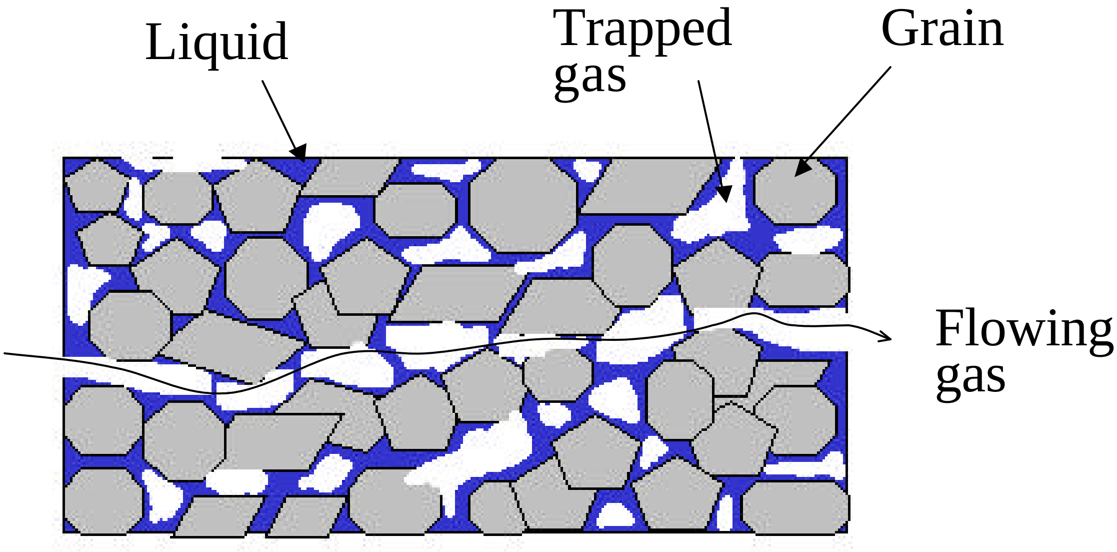

Figure 1.1 Schematic microscopic view of foam in porous media

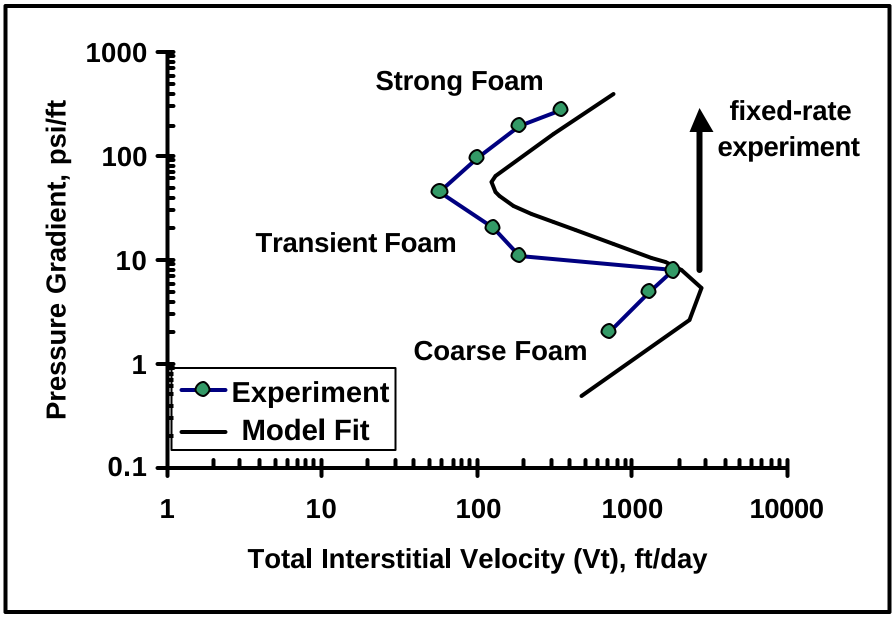

Figure 1.2 Foam-generation experiment in Berea core from Gauglitz *et al*. (2002) with model fit from Kam and Rossen (2002). At low pressure gradient (coarse-foam regime), total interstitial velocity is relatively high and gas mobility is high. At high pressure gradient (strong-foam regime), gas mobility is much lower. In between these is an unstable "transient" regime. In these experiments pressure drop across the core was held fixed and gas and liquid injection rates (at fixed quality) were controlled to maintain the fixed pressure gradient. In a more conventional experiment at fixed injection rates, coarse foam would abruptly change to strong foam at a total interstitial velocity of about 2000 ft/day.

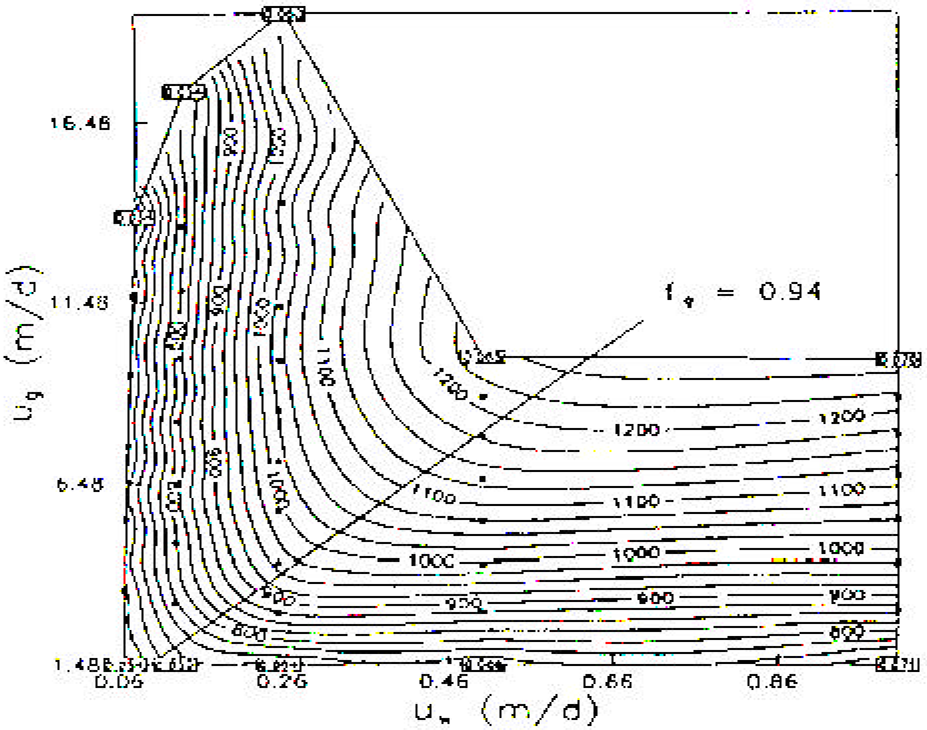

Figure 1.3 Pressure drop (psi) across a two-ft sandpack as a function of gas (u_g) and water (u_w) volumetric flexes, from Osterloh and Jante (1992). Upper-left region is the high-quality regime, and lower-right the low-quality regime. In this case, the transition between regimes occurs at a foam quality f_g of about 0.94 (94%). The transition foam quality varies depending on surfactant formulation, porous medium and other factors.

Chapter 2: Effective Viscosity of Foam in Periodically Constricted Tubes

2. 1 INTRODUCTION

2.1.1 Background

Foam is a promising tool in both the oil industry and environment remediation. Foam is used on a pilot basis to redirect gas flow in improved oil recovery (Schramm, 1994). Foam is used routinely in acid well-stimulation where foam re-directs acid flow to the desired interval (Gdanski, 1993). Foam is also considered a promising means to help clean up contaminated aquifers (Hirasaki, *et al*., 1997).

In foam flow through rock, most gas stays trapped. According to Gillis and Radke (1990), up to 70% to 99% of gas stays trapped in foam flow. In the experiments of Friedmann *et al.* (1991) in Berea sandstone, about 85% of resident gas remained trapped during foam flow.

Falls *et al.* (1989) conducted foam-flow experiments in bead packs, and found that foam flows along a few separate paths, with all other pores filled by trapped gas bubbles. In these paths, foam flows like a 'bubble train' through regions of trapped gas. Therefore moving bubbles are moving in a geometry not too unlike a periodically constricted tube as shown schematically in Figure 2.1. Generally, foam bubbles are larger than rock pore size (Gillis and Radke, 1990), so individual soap films, or lamellae, rather than many small bubbles, span individual pores.

Falls *et al*. (1989) split the apparent viscosity of gas in foam μ_{app} into two parts: the effects of constrictions, $\mu_{con,}$ and of viscous drag, μ_s :

$$\mu_{app}=\mu_{con}+\mu_s \quad . \tag{2.1}$$

This equation implies that pressure drop is given by

$$\Delta p=\Delta p_{con}+\Delta p_s \, . \tag{2.2}$$

The constriction effect is a yield stress that gives a constant contribution Δp_{con} independent of velocity. Falls *et al.* (1989) use results from Hirasaki and Lawson (1985) for bubbles moving in smooth capillaries to account for the viscous drag. They show good agreement between their model and experimental data for the apparent viscosity of foam in bead packs.

2.1.2 Effect of constrictions

To estimate Δp_{con} theoretically, Falls *et al.* (1989) assume that all lamellae are lodged in pore throats, where capillary resistance is greatest. In 3D, the pressure drop across a spherical lamella is $4\sigma/r$, where σ is surface tension and r is the radius of the lamella. Later, in fitting data, the values of Δp_{con} were adjusted to optimize the fit.

Rossen (1990a,b,c,d) considers the quasi-static movement of lamellae through schematic pores, illustrated in Figure 2.1. Δp_{con} for a bubble train is the number of lamellae times the population-average Δp per lamella. For incompressible bubbles, the population-average for the train equals the time-average Δp for one lamella crossing one pore, $(\Delta p)^{ave}$ (Rossen, 1990b). With constrictions at both entrance and exit, and some lamellae bulging forward and some backwards, one might guess that $(\Delta p)^{ave} = 0$. Rossen shows that $(\Delta p)^{ave} > 0$, if the pore has a relatively wide pore body, narrow pore throat, and a relatively sharp corner at the pore body. The reason is that the lamella spends more than half of its time in the first half of the pore, bulging forward, before jumping to the other side of the pore. Rossen also shows that even in radially symmetric pores, lamellae jump spontaneously to asymmetric shapes straddling the pore body. Examples are shown below. The resulting lamella shapes are complex in 3D, but a much simpler rigorous analysis in 2D also reproduces this behavior. This asymmetric jump increases $(\Delta p)^{ave}$ and the effective yield stress of foam.

2.1.3 Effect of drag

There have been several studies of viscous drag in bubble flow in cylindrical capillaries. Bretherton (1961) analyzes the motion of long bubbles in tubes. He assumes isolated bubbles flow in circular tubes at low velocity. The analysis is limited to very long bubbles with low capillary number, $Ca = \mu U/\sigma$, where μ is viscosity of the liquid phase, U is the velocity of moving bubble and σ is surface tension. Using an asymptotic approach, he concludes that the pressure drop across a bubble is $\Delta p \approx 3.58(3Ca)^{2/3} (\sigma/R)$, where R is the radius of the capillary tube.

Hirasaki and Lawson (1985) account also for surface-tension gradients along a bubble due to drag on surfactant molecules by liquid flow. Like Bretherton, they consider the case of isolated bubbles, with slugs of liquid in between, but then extrapolate their results to zero thickness of the liquid slug between bubbles to represent bubble trains. In this model, the apparent viscosity comes from three sources: drag in the liquid slug, radii of curvature of the leading and trailing surfaces of the bubble, and surface-tension gradients along the bubble. In the limit with no liquid slug between bubbles, and bubbles as wide as pores as in Figure 2.1, apparent viscosity μ_{app} scales as $U^{-1/3}$, and Δp scales as $U^{2/3}$ (see Appendix A for details). They fit data for bubbles in smooth cylindrical tubes to the model with a reasonably good fit even for bubbles that touch. The parameter values from the fit to the data indicate that the surface-tension gradient is an important contribution to the overall drag.

Ratulowski and Chang (1989) assume touching bubbles, with a lamella and Plateau borders in between, in circular tubes and without surface-tension gradients, at higher Ca than Bretherton (1961). They use an arc-length formulation of a composite lubrication equation for both low and high capillary numbers. Simple relations for pressure drop and film thickness, as functions of capillary number, are derived. The apparent angle that the extension of the lamella makes with capillary wall, which is not equal to 90^o, is determined in this analysis. They conclude that $(\Delta p_D) \equiv \Delta p/(\sigma/R)$, the dimensionless pressure drop across a lamella, is of order of $Ca^{2/3}$.

Wong *et al.* (1995) extend the theory of Bretherton (1961) for long bubbles separated by slugs of liquid to capillaries with cylindrical and polygonal cross-section. For a cylindrical capillary tube, they conclude that (Δp_D) scales as $Ca^{2/3}$. In non-circular tubes, due to domination of corner flow of liquid at very low velocity, the exponent is closer to 1.

2.1.4 Objectives

Solutions are available for the effects of pore constrictions in the quasi-static limit and for viscous drag on bubbles in tubes with uniform cross-section. There is as yet no solution for both effects simultaneously. This work models dynamic lamella motion in a periodically constricted tube accounting for both drag and capillary effects.

Our goals are limited. There is no solution for drag on individual Plateau borders (as opposed to isolated bubbles) that accounts for both hydrodynamics and surface viscosity, in even smooth capillaries. All solutions cited above are for steady-state flow. Rather than focus on the fluid mechanics of the Plateau border in dynamic movement through a constricted tube, we use the results above to investigate how coupling between capillary forces on the lamella and drag on the Plateau border governs the movement of lamellae through constricted tubes.

2.2 MODEL AND ASSUMPTIONS

2.2.1 Geometrical model

A wedge-shaped pore in 2D, shown in Figure 2.2, is the basis of our analysis. For purposes of calculation, pore depth in the third dimension is W. The pore wall is referred to here as the diverging pore wall on the left-hand side of the pore and the converging pore wall on the right-hand side. At the pore corner, a sine function (see Appendix B) provides a smooth transition between diverging and converging pore walls over a distance ($2\varepsilon L$), where ε is the dimensionless half-width of the rounded region. A smooth transition at the corner is appropriate even in angular pores, because water occupying the pore corners can effectively round off the pore body.

Specifically, Rossen (Rossen, 1988) shows that at finite capillary pressure a lamella begins to deviate from being perpendicular to the straight pore wall at a distance we call here (εL) of a little more than r_c from a sharp corner, where r_c is the radius of the Plateau border. (we use the same notation as Hirasaki and Lawson (1985) (see Appendix A) rather than Rossen (1988).) Capillary pressure P_c sets r_c:

$$P_c = \sigma / r_c , \tag{2.3}$$

and

$$P_c/P_c^e = R / (2\, r_c) = (R/L)\, (1/(2\, \varepsilon)) \tag{2.4}$$

for a round pore and

$$P_c/P_c^e = R / (r_c) = (R/L)\, (1/\varepsilon) \tag{2.5}$$

for a 2D wedge-shaped pore, where P_c^e is the capillary entry pressure of the pore. Using the formula for a round pore, for a typical case below with $(R/L) = 0.125$ and $\varepsilon = 0.05$, $P_c/P_c^e \approx 1.25$. (For $P_c/P_c^e \approx 1$ or less, a separate phenomenon, bubble separation at pore throats, can occur (Rossen, 1988). We do not address that phenomenon here.) Thus a large value of ε could represent either a gently rounded pore or an angular pore at relatively low capillary pressure.

A single lamella is taken as the focus of study because for an incompressible foam the motion of one lamella through one pore represents the behavior of the whole bubble train (Rossen, 1990b). Moreover, analysis of a compressible bubble train starts with the solutions derived for an incompressible bubble train (Rossen, 1990b).

Movement is from left to right. The advance of the lamella is regulated by pistons moving at constant velocity, V, both upstream and downstream of the pore (Figure 2.2). Note that the volumetric advance of the lamella during a time interval Δt is then $(2\ R\ W\ V\ \Delta t)$, where R is the radius of both the pore throat and the piston.

2.2.2 Assumptions

Gas is assumed to be incompressible and has negligible viscosity.

We assume that the lamella shape adjusts instantaneously to minimize its area subject to given bubble volume and the positions of its Plateau borders, while the Plateau borders respond more slowly to piston advance. With this assumption, lamella shape is always a circular arc.

Plateau borders are treated as points of contact between the lamella and the pore wall.

We assume that lamellae do not break during movement through the pore. Like other models (Falls *et al*, 1989; Kovscek *et al*., 1995), we separate the issues of foam coalescence and foam viscosity at a given bubble size.

Surface tension is assumed to be constant.

2.3 METHODOLOGY

2.3.1 Basic equations

Most of the studies of steady-state viscous drag in capillary tubes cited above conclude that

$$(\Delta p)_D = K' \; U^{2/3} , \tag{2.6}$$

where $(\Delta p)_D = \Delta p/(\sigma/R)$ is the dimensionless pressure drop, U is the velocity of the bubble, and K' is a constant that varies among the studies (see Appendix A). The study of Wong *et al*. (1995) considers the effect of water flow along pore and corners, and substitutes an exponent as large as 1 in Eq. 2.6 in some cases. We do not believe this difference would greatly affect what follows.

Consider a case with a lamella (in 2D) in a straight channel driven by a moving piston (Figure 2.3(a)). Take one of the Plateau borders as subject for a force balance. Surface tension exerts a force forward on the Plateau border, which is $[2 \; W \; \sigma \cos(\theta)]$, where θ is the angle the lamella makes with the pore wall; the factor of 2 accounts for the two surfaces of lamella. This term equals half of the total drag, $[(½)(\Delta p \; 2 \; R \; W)]$. A force balance on the Plateau border in the x direction gives

$$2 \; W \; \sigma \cos(\theta) = ½ \; \Delta p \; 2 \; R \; W$$

$$\cos(\theta) = \Delta p \; R/ (2 \; \sigma) \equiv (\Delta p)_D /2 = K' \; / \; 4 \; (V)^{2/3} \equiv (KV)^{2/3} \tag{2.7}$$

where $(\Delta p)_D = [(½) \, K' \; V^{2/3}]$ in 2D and K is a constant equal to $(K'/4)^{3/2}$. We define the dimensionless piston velocity as

$$V_D = K \; V. \tag{2.8}$$

A similar relation to Eq. 2.7 is derived in Ratulowski and Chang (1989).

Although this equation is derived from the steady-state motion in a channel, here we assume it applies instantaneously to Plateau borders in dynamic movement through constricted tubes (*cf*. Figure 2.2):

$$\cos(\theta_1) = (K\ V_1)^{2/3} \tag{2.9}$$

$$\cos(\theta_2) = (K\ V_2)^{2/3} \tag{2.10}$$

where θ_1, θ_2, V_1, and V_2 are the angles and velocities of the two Plateau boders along the pore walls. Note that the velocity of the Plateau border is zero if the apparent angle the lamella makes with the pore wall is $\pi/2$ (i.e., if the lamella is perpendicular to the pore wall). Individual Plateau borders can move backwards ($V_i < 0$) temporarily if $\theta_i > \pi/2$; examples are shown below.

The variables that determine lamella positions and shape are θ_1, θ_2, x_1, y_1, x_2, y_2, and r. Constraints on the systems are Eqs. 2.9 and 2.10, the volume constraint behind the circular lamella, and of course that the two Plateau borders must remain on the pore wall. Note also (Figure 2.2) that $dx_1/dt = V_1(\cos\beta)$ and $dx_2/dt = V_2(\cos\beta)$ for the Plateau borders on the pore walls.

2.3.2 The numerical method

2.3.2.1 Input parameters

One must specify initially the pore shape, value of K', piston advance velocity V, time step Δt and initial lamella position and shape to start a simulation.

There are three independent pore-geometrical parameters, (R/L), β and ε (Figure 2.2). At fixed dimensionless pore-throat radius $R_D \equiv R/L$, pore-body width is controlled by the inclination angle β; the bigger the angle, the fatter the pore is. Values of R/L = 0.125 and $\beta = 22.5^o$ are taken in most cases, which gives a pore 63% as wide as it is long. Another geometrical parameter is the half-width of the pore corner ε, which is found to be extremely important in altering lamella behavior and therefore $(\Delta p)^{ave}$. Values of ε used here vary from nearly 0 to 0.14, representing from a sharp corner to a very gentle corner. As noted above, ε may reflect either water occupying a sharp pore corner at finite capillary pressure or a gently rounded solid pore wall.

Parameter K' governs the drag on the Plateau borders. Appendix A shows that there is a range of values of K' implied in the literature. Here we report results in terms of a dimensionless velocity V_D (Eq. 2.8) that combines K and V, the velocity of the piston pushing the lamella (Figure 2.2).

2.3.2.2 Numerical method

A finite-difference method is used to calculate the sequence of lamella positions and shapes. Starting from a known position and shape (x_{11}, y_{11}, θ_{11}, x_{21}, y_{21}, θ_{21}, r_1), the algorithm below determines the resulting lamella position and shape (x_{12}, y_{12}, θ_{12}, x_{22}, y_{22}, θ_{22}, r_2) after one time step. Here the first subscript in the variables distinguishes Plateau borders (Figure 2.2) and the second subscript distinguishes starting (1) and updated, or resulting (2) value of the variables. Thus for instance r_1 is the initial value of r and r_2 is the resulting r. The resulting lamella position and shape is then taken as a new starting point, and so on for the duration of the calculation. Since at the start we don’t know initial lamella shape as it passes through the pore throat, we run the simulation into an identical second pore to determine how the lamella behaves near the pore throat.

For Plateau border 1 a forward-difference method is used, in the method Plateau border sliding-velocity V_1 is calculated from θ_{11} according to Eq. 2.9. Then the new position can be calculated as

$$x_{12}=x_{11}+V_1\,\Delta t\cos(\alpha), \tag{2.11}$$

where $\alpha\equiv\arctan(dy/dx)$ is the angle between the tangent to the pore wall and the horizontal direction; on the straight pore wall $\alpha=\beta$, whereas in the pore corner α changes smoothly from β to zero at the pore mid-point to $-\beta$ on the converging pore wall. y_{12} can be easily calculated from the equations defining pore shape. θ_{12} is undetermined at this point.

For Plateau border 2 a backward-difference method is used. An assumed value for θ_{22} determines V_2 using Eq. 2.10 and x_{22} using Eq. 2.12

$$x_{22}=x_{21}+V_2\,\Delta t\cos(\alpha)\ . \tag{2.12}$$

y_{22} can be easily determined from the shape of the pore wall. Now with the position of the two Plateau borders and θ_{22} fixed, θ_{12} and r_2 can be determined uniquely from the constraints that the lamella passes through the two Plateau borders and makes an angle θ_{22} with pore wall at Plateau border 2. The volume increment is then computed, which should equal the incremental volume swept by the piston in this time step. Otherwise, the initial guess θ_{22} is updated and the above calculation repeated. The final result satisfies all the geometrical constraints and the volume-conservation constraint.

In Eqs 2.11 and 2.12, V_1 and V_2 could be less than zero, meaning that the Plateau border moves backwards.

The mixed forward- and backward-difference method has an advantage over the purely forward-difference method in numerical stability. Numerical testing shows that there is no significant difference between these methods in most cases as long as time step is small enough. Also, in this scheme, it is always Plateau border 2 that reacts first to the bend in the pore wall at the pore body.

2.3.2.3 Time steps

The time step in the simulation must be small enough to minimize numerical artifacts. Especially near the pore corner, where the lamella jumps, the time step Δt must be small to resolve the jump in the presence of very high Plateau-border velocities V_1 and $V_{2,}$ as well as dramatic changes in lamella shape. In most cases we used 10^7 time steps to track lamella movement across one pore.

2.3.2.4 Computing final results

Lamella position and shape are calculated at each time step. With this, pressure drop across the lamella (in 2D) can be obtained from lamella radius r:

$$\Delta p = 2\sigma/r \quad . \qquad (2.13)$$

The dimensionless time-average pressure drop $(\Delta p_D)^{ave}$ is given by

$$(\Delta p_D)^{ave} \equiv \int_0^1 \Delta p_D \, \Delta t_D \quad , \qquad (2.14)$$

where t_D is the dimensionless time, i.e. time divided by the time required for the lamella to pass through one pore.

A PC animation showing lamella motion in pores is available for download at http://www.pe.utexas.edu/CPGE/FOAM/. The animation features all the cases shown below, with ability to pause, move backwards, and monitor x_{1D}, x_{2D} and Δp_D simultaneously with lamella shape.

2.4 SIMULATION RESULTS

2.4.1 Asymmetric jump

The sequence of lamella shapes shown in Figure 2.4 corresponds to $V_D = 2.9 \times 10^{-5}$, $\varepsilon=0.05$, $R/L = 0.125$, $\beta= 22.5^o$. The Figure shows only a small fraction of the 10^7 time steps in the simulation, of course. The lamella advances smoothly from (A) to (B), with angles θ_1 and θ_2 both very close to 90^o. The lamella shape stays symmetric about the x-axis during this period. Shortly after the lamella enters the curved corner at the pore body, the lamella jumps to an asymmetric shape, from (B) to (C). The dimensionless time corresponding to this jump is less than 10^{-6}, but still much larger than an individual time step in the simulation. During the jump, Plateau border 2 moves ahead faster and forces Plateau border 1 to move backwards to conserve bubble volume. The reason for the jump is discussed further below. From (C), the lamella then advances smoothly to (D). Next it jumps from (D) to (E) as Plateau border 1 enters the corner region again; the sharp change in angle with the pore wall forces Plateau border 1 forward, and Plateau border 2 retreats to maintain bubble volume.

The lamella moves smoothly from (E) to (F), nearly the mirror image of the corresponding part of the sequence from (A) to (B). Here, though, the lamella bulges backwards, with a negative pressure drop across the lamella. Physically, the lamella is pulled into the pore throat by surface tension. (Actually, the sequence from (E) to (F) differs slightly from that from (A) to (B), because drag on the lamella slightly distorts the angle of the lamella on the pore wall).

In Figure 2.4(b), points (A) to (F) correspond to the indicated shapes in Figure 2.4(a). Here $x_{1D} \equiv (x_1/L)$, and $x_{2D} \equiv (x_2/L)$. The split in the pathway in Figure 2.4(b) correspond to the asymmetric jump.

Figure 2.4(c) shows the dimensionless pressure drop across the lamella as a function of time. When the lamella bulges backwards, from (E) to (F), the pressure drop is negative, as the lamella is pulled forward in the converging part of the pore. The integral of the curve in Figure 2.4(c) gives $(\Delta p_D)^{ave}$ (Eq. 2.14); here the path from (E) to (F) partially cancels the work done from (A) to (B).

2.4.2 Asymmetric jump at higher piston velocity

As the dimensionless velocity increases to $V_D = 0.0058$ (Figure 2.5), the sequence of lamella shapes is roughly the same as in the previous case, with three differences. First, the lamella almost completes the jump to a symmetric shape after point (B) (see point O), but fails. Second, the lamella travels a little longer before the jumps from (B) to (C) and from (D) to (E). Third, with this higher velocity, drag makes Δp_D somewhat larger from (A) to (B), slightly positive from (C) to (D), and smaller from (E) to (F). All these differences are discussed further below.

2.4.3 Symmetric jump

At even higher velocity, V_D= 0.006, the Plateau borders complete a symmetric jump across the pore body, as shown in Figure 2.6(a) in the sequence A-B-E-F.

There is a noticeable, but small, difference between the two Plateau-border positions x_1 and x_2 during the jump, as discussed further below; therefore, this is not a perfectly 'symmetric' jump in that sense. However, as illustrated in Figure 2.6(b), the sequence is nearly symmetric ($x_1 \cong x_2$).

Figure 2.6(c) shows that the loss of the sequence from (C) to (D) here (*cf*. Figure 2.4(c)) reduces the capillary contribution to $(\Delta p_D)^{ave}$, because it replaces a sequence of nearly flat shapes with shapes that are concave and pulling the lamella forwards.

2.4.4 Transitional behavior

Figure 2.7(a) shows lamella sequences in a more gently rounded pore (ε = 0.14) at different velocities. At low velocity (V_D = 0.0003), the lamella makes an asymmetric jump, though it does not immediately take its shape of maximum asymmetry, and there is a gradual decrease in asymmetry before the jump back to a symmetric shape. Rossen (1990c) shows a similar result for quasi-static movement through gently rounded pores. As velocity increases, the lamella makes the asymmetric and return jumps later, and the degree of asymmetry gradually decreases (Figures. 7(a), 7(b)). At large velocity (V_D = 0.004), the sequence is essentially symmetric.

Unlike the abrupt change from an asymmetric jump to a symmetric jump observed with the sharper pore corner, the change in behavior shown in Figure 2.7 is gradual. We call this “transitional behavior.”

2.4.5 Average pressure difference

Figure 2.8 plots $(\Delta p_D)^{ave}$ v. dimensionless piston velocity V_D in pores with several values of ε. In all cases, R/L = 0.125 and $\beta = 22.5°$. For $\varepsilon \leq 0.08$ (Figure 2.8(a)), the curves have a discontinuity in $(\Delta p_D)^{ave}$ at some velocity. In Figure 2.8(a) with $\varepsilon = 0.05$, the case in Figure 2.4 corresponds to the limit of nearly zero V_D; Figure 2.5 to the point on Figure 2.8(a) just before the abrupt drop in $(\Delta p_D)^{ave}$; and the case in Figure 2.6 to the point just after the drop. Thus the abrupt drop in $(\Delta p_D)^{ave}$ is due to the change from asymmetric to symmetric lamella jumps.

The change from asymmetric to symmetric jumps appears to be abrupt; for instance, at $V_D = 0.0058$ we find an asymmetric jump, and at $V_D = 0.006$ a symmetric jump, with a remarkably different value of $(\Delta p_D)^{ave}$.

Just before the discontinuous drop in $(\Delta p_D)^{ave}$ for $\varepsilon = 0.05$ in Figure 2.8(a), however, there is a small decrease in $(\Delta p_D)^{ave}$ with increasing velocity. This is due to for a brief time the lamella takes reversed curvature with negative Δp_D (point ‘O’ on Figure 2.5) before it finally makes the asymmetric jump.

Over the range of ε from 0 to 0.08, the transition to lower $(\Delta p_D)^{ave}$ occurs at higher dimensionless velocity as ε increases. In the limit $\varepsilon \to 0$, i. e. a sharp corner (not shown on Figure 2.8), the velocity at which the abrupt drop occurs approaches zero, though results are affected by the size of any perturbations (see below) and the size of the time step used in the simulation.

Figure 2.8(b) plots $(\Delta p_D)^{ave}$ v. V_D for $\varepsilon \geq 0.09$. As ε increases the intercept at $V_D \rightarrow 0$ decreases, in agreement with the quasi-static analysis of Rossen (1990c). At about $\varepsilon = 0.09$ the discontinuous drop in $(\Delta p_D)^{ave}$ disappears, replaced by a continuous decrease over a range of V_D, in what we call "transitional behavior." The transitional region of decreasing $(\Delta p_D)^{ave}$ moves to smaller velocities as ε increases.

2.4.6 Viscous drag

Apart from the abrupt drop, $(\Delta p_D)^{ave}$ increases monotonically with increasing velocity in both symmetric and asymmetric regimes. This is due to increasing viscous drag. To separate the viscous drag from the total $(\Delta p_D)^{ave}$, one must separate the effects of the constriction, which can be estimated by extrapolating $(\Delta p_D)^{ave}$ values to zero V_D (denoted on Figure 2.9 as $(\Delta p_D)^{o}$). Subtracting this part from the total $(\Delta p_D)^{ave}$ gives the viscous contribution.

Figure 2.9 compares viscous-drag portion of the overall pressure drop for $\varepsilon = 0.05$ for a 2D wedged-shaped pore with that for a 2D straight conduit with width equal to the average width of the wedge-shaped pore. For this case, at least, at low velocity the assumption of Falls *et al.* (1989) is accurate; the total pressure drop is the sum of a part due to constrictions, which can be estimated from quasi-static movement, and a contribution from viscous drag, equal to that in a volumetrically equivalent straight conduit. Or, in other words, $(\Delta p_D)^{ave}$

consists of a constriction term and a viscous term that scales with (2/3) power of volumetric velocity. This is remarkable, because velocity of the lamella in the constricted pore is far from constant.

At higher velocities this assumption is very inaccurate, especially where $(\Delta p_D)^{ave}$ decreases with increasing velocity. Close examination of the case ε = 0.05 (Figure 2.8 (a)) shows that $(\Delta p_D)^{ave}$ is lower at a dimensionless velocity of $V_D = 0.006$ than that in quasi-static movement ($V_D \rightarrow 0$). Both Rossen (1990a,b,c,d) and Falls *et al.* (1989) assume that the value of $(\Delta p_D)^{ave}$ in quasi-static movement is the lower limit of $(\Delta p_D)^{ave}$; that assumption breaks down in this case.

2.4.7 Effect of pore-shape parameters

Figure 2.10(a) shows the effect of R/L (pore-throat width) on $(\Delta p_D)^{ave}$ for small values of ε. Pores with wider pore throats have smaller values of $(\Delta p_D)^{ave}$ and smaller transition velocities. With a large value of ε (Figure 2.10(b)), the value of R/L affects both the value of $(\Delta p_D)^{ave}$ and the velocities in the transition region. As $V_D \rightarrow 0$, $(\Delta p_D)^{ave} \rightarrow 0$ for large values of ε.

Figure 2.11(a) shows the effect of β (and, by implication, pore-body width) on $(\Delta p_D)^{ave}$ for a small value of ε. In agreement with Rossen (1990a) the pore with the wider pore body (larger β) has a larger value of $(\Delta p_D)^{ave}$ at $V_D \rightarrow 0$. With large ε (Figure 2.11(b)), the value of β affects both the magnitude of $(\Delta p_D)^{ave}$ (note difference of scale between Figures. 11(a) and 11(b)) and the velocities in the transition region). With larger ε, β must be relatively large or jumps disappear at even $V_D \rightarrow 0$ (Rossen, 1990a).

2.5 THEORY OF STABILITY OF SYMMETRIC SEQUENCE OF LAMELLA SHAPES

2.5.1 Stability in quasi-static movement

Rossen (1990c) considers quasi-static movement through 2D pores symmetric about the x-axis. In quasi-static movement θ_1 and θ_2 are always 90^o, and the lamella always seeks to minimize its area. In passage through the straight diverging and converging sections, symmetric lamella shapes ($x_1 = x_2$) are stable, in that any small derivation from symmetry increases lamella area. At a point within the rounded region at the pore body, however, the Jacobean of energy with respect to x_1 and x_2 has a zero eigenvalue, indicating the limit of stability. The corresponding eigenvector, (1, -1), indicates that one Plateau border moves forward and one back (Rossen, 1990c).

Unfortunately, for dynamically moving lamellae, $\theta \neq 90^o$, and this approach does not apply because the assumption of $\theta_i = 90^o$ breaks down. A theory for stability of the symmetric sequence $x_1 = x_2$ for lamellae moving at finite velocity is needed.

2.5.2 Stability criterion in dynamic movement

In numerical simulation, the coordinates of the Plateau borders (x_1, x_2) differ at all times by at least a numerical tolerance allowed in solving the differential equations (approximately 10^{-14} in our simulations). In nature, similar perturbations would result from a variety of causes. The question is, would naturally occurring perturbations away from symmetry grow or be suppressed as the lamella advances?

The angles θ_1 and θ_2 of the two Plateau borders govern the motion of the Plateau borders (Eqs 2.9 and 2.10). Consider the change in θ_1 and θ_2 under a perturbation (Figure 2.12). Before the perturbation, the lamella shape is symmetric, with $x_1 = x_2$ and $\theta_1 = \theta_2$. Suppose then that Plateau border 1 is perturbed ahead of Plateau border 2 with $\Delta x \equiv (x_1 - x_2)$, Appendix B shows that after the perturbation

$$\theta_{12}-\theta_{22} = 2P- N. \tag{2.15}$$

Here P is the angle of inclination of the lamella arc, as illustrated in Figure 2.12, and N is the change in the angle of the pore wall with the perturbed position of x_1. If (2P- N) is positive, then $\theta_{12} > \theta_{22}$, which means that the Plateau border 1 moves slower than the Plateau border 2 in next time step. This means that the lagging Plateau border 2 tends to catch up and the perturbation is suppressed. If (2P-N) < 0 then Plateau border 1 moves ahead faster than Plateau border 2, increasing the perturbation. Thus N acts as a destabilizing driving factor and P as a stabilizing factor.

Consider some specific cases. When both Plateau borders are on the straight converging or diverging pore walls, pore-wall direction does not change, N = 0, and therefore (2P- N) = 2P > 0, which means perturbations are always suppressed. Thus the symmetric sequence shape is intrinsically stable along the straight edges of the pore. Simulation results above confirm this conclusion.

In the rounded pore body, $N \neq 0$, i.e. the inclination of the pore wall changes with perturbation in position. Thus, depending on N and P, (2P-N) may be greater than, less than, or equal to zero. The mathematical expressions for N and P are (Appendix B):

$$N = \int (d\alpha/dx)\, dx \approx \Delta x \ (y'/(1+(y')^2)) \tag{2.16}$$

$$P = \arctan(\Delta x/(y_1-y_2)) \approx \Delta x/(y_1-y_2) \ . \tag{2.17}$$

Therefore,

$$\begin{aligned} 2P - N &\approx 2\,\Delta x/(y_1-y_2) - \Delta x \ (y'/(1+(y')^2)) \\ &\approx \Delta x\,((2/(y_1-y_2)) - y'/(1+(y')^2)) \ . \end{aligned} \tag{2.18}$$

Thus, the sign of (2P- N) depends solely on the pore geometry and not, for instance, on velocity. If (2P-N) > 0 along the entire pore body, then the symmetric lamella shape is stable regardless piston velocity, perturbation, or time-step size. One example of stable symmetric movement without a jump is the case with x/L = 0.125, $\beta = 22.5^o$, and $\varepsilon = 0.20$, in agreement with Rossen (1990a). However, if (2P-N) < 0 at some point, the lamella moves away from its symmetric shape; but we can not predict the lamella behavior after (x_1-x_2) becomes large.

2.5.3 Effect of piston velocity on stability

The criterion of intrinsic stability, Eq. 2.18, includes no effect of velocity. Yet Figures 8(a) and 8(b) clearly indicate that piston velocity affects the nature of the jump across the pore body. Higher velocity means smaller θ_1 and θ_2 at the point of instability (Eqs. 2.9 and 2.10). If both Plateau borders are moving forward faster as instability starts, they both move forward even as one begins to move ahead of the other. The higher the piston velocity, the better the lamella's chance of getting across pore body before the asymmetric perturbation gets large.

Figure 2.13 compares the growth of asymmetry near the pore body as a function of piston velocity. The perturbation initially grows in all cases. For $V_D \rightarrow 0$, the perturbation grows quickly to an asymmetric jump. With increasing velocity, the lamella travels further before the perturbation grows large enough to trigger the jump. For $V_D = 0.0035$, the perturbation $|x_{1D}-x_{2D}|$ grows to about 0.03, but by this point both plateau borders have passed the pore body and the perturbation decreases. Thus, this perturbation is suppressed and lamella makes a symmetric jump instead.

2.5.4 Effect of size of initial perturbation

The analysis above suggests that the size of perturbations initially present affects whether the lamella ultimately makes symmetric or asymmetric jump. Figure 2.14 shows that the magnitude of the initial numerical perturbation, which was controlled in most simulations by the tolerance in the numerical routine, changes the velocity at which the asymmetric jump disappears. In Figure 2.14 we added a random perturbation δ to x_1 much larger than this numerical tolerance in each time step. The greater the initial perturbation, the faster the perturbation grows, and the more likely the lamella makes an asymmetric jump.

This result further suggests that the transition from asymmetric to symmetric jumps can be affected by any factors that affect the size and growth of perturbations: numerical tolerance in solving the equations, time-step size, and numerical scheme used to solve the equations. In physical lamella movement, behavior would depend on deviation from perfect symmetry in the pore. In a perfectly symmetric pore, perturbations could arise from thermal fluctuations.

2.6 EXPERIMENTAL DEMONSTRATION

Rossen (1990c,d) presents several examples of asymmetric lamella jumps in slow movement through bi-conical glassware, and a theoretical explanation independent of any experimental imperfections (slight asymmetries in glassware, dirt on glass surfaces, etc.). Here we present a demonstration of the asymmetric jump disappearing at high velocity.

Experiments were conducted in a bi-conical glass pore (Figure 2.15) about 10 cm long, with pore-body diameter 4 cm ($\beta = 11.3^o$). The liquid was a 2.0 wt % solution of 'Joy' detergent (Procter and Gamble, Cincinnati, Ohio) in tap water and the gas was nitrogen. Gas flow behind the lamella was measured with a Brooks mass flow meter (Brooks Instruments). The bi-conical pore is of course 3D, not 2D, and we do not know the value of K in this experiment. It would be impractical to measure Δp directly with so large a value of lamella radius r. Nevertheless Figure 2.15 confirms the existence of an asymmetric jump at a gas flow rate of 10 cm^3/min. and a transition to more symmetric movement at a gas flow rate larger than 250 cm^3/min.

2.7 DISCUSSION

The transitions in behavior predicted by the 2D model occur at dimensionless velocities around 0.005 (Figure 2.8). Dimensionless velocity is the product of gas velocity and K, i.e. $(K'/4)^{2/3}$. Appendix A shows that estimates of K' inferred from the literature for flow in pores vary widely. The formula derived from Hirasaki and Lawson (1985) is directly based on theory, but the experiments to confirm the theory were conducted in tubes much larger than the pores on consolidated rock through which foam flows. The estimate based on the model fit of Kovscek *et al*. (1995) derives from coreflood data, but their parameter values used in Appendix A could have been affected by the fits to the many other parameters in their model.

Suppose foam flows at an overall gas volumetric flux (flow rate divided by cross-sectional area of the medium) of 1 m/day. If the core has porosity 20%, and 95% of the gas is trapped, then the average gas velocity through pores where gas flows is 1.16 mm/s. To obtain a dimensionless velocity V_D of 0.005, one thus requires

$$V_D = 0.005 = 0.00116\,(K'/4)^{2/3} \qquad (2.19)$$

which implies $K' \approx 36$. This is well within the range inferred from the equation of Hirasaki and Lawson for pores 200 μm in diameter (Appendix A), though well above the estimates based on the other models. Thus it appears that the transitions described here may well occur at realistic velocities in consolidated porous media encountered in foam applications.

Observing the abrupt drop in Δp with increasing foam flow rate shown in Figure 2.8 in realistic porous media would require that foam flow through a chain of identical pores. With a variety of pore shapes the transition would occur at different velocity in each pore. The net effect might be extremely shear-thinning behavior, as the drop in effective viscosity occurs in various pores over a range of flow rates. If Δp did drop abruptly, this might cause more foam to become trapped, partially reversing the effect.

Gas compressibility also plays a part in the effective viscosity of foam (Rossen, 1990b). When compressibility is significant, jumps occur from pore throats in addition to pore bodies. In quasi-static analysis, compressibility is important primarily when surrounding bubbles respond to pressure changes in flowing bubbles; pore geometry favors this in beadpacks rather than in the angular pores of rock (Rossen, 1990b).

Foam rheology in porous media depends on many factors not addressed here, including dynamic processes of bubble creation, destruction, and trapping and mobilization (Kovscek *et al.*, 1995). In at least some flow regimes, behavior is dominated by factors other than effective viscosity at fixed bubble size (Alvarez *et al.*, 2001). Foam apparent viscosity, at fixed bubble size, is just one component of a complete analysis of foam in porous media.

2.8 CONCLUSIONS

For the first time we present a dynamic model for the movement of bubbles through constricted tubes in 2D, accounting for the drag on lamellae along pore walls and the capillary forces that govern bubble shape in constricted tubes.

Simulation shows that in the limit of slow flow rate, lamellae jump to asymmetric shapes even in radially symmetric pores, in agreement with Rossen (1990a,b,c,d). The drag on the lamella increases the pressure gradient above the quasi-static limit by a factor scaling roughly as the 2/3 power of velocity, in agreement with Hirasaki and Lawson (1985).

At sufficiently high velocities, however, a symmetric jump replaces the asymmetric jump. In such cases unstable perturbations away from the symmetric shape have insufficient time to grow before the lamella settles into a symmetric shape on the other side of pore body.

A lamella moving at a faster rate may require a lower pressure gradient than one moving more slowly, due to the disappearance of the asymmetric jump.

In gently rounded pores, the asymmetric jump gradually changes to symmetric movement as velocity increases.

Observations of lamella movement in glass pores support the prediction that lamellae make asymmetric jumps at low velocity and the asymmetric jumps disappear as velocity becomes sufficiently high.

The phenomena predicted by theory are expected to occur at realistic flow rates in consolidated porous media. More research is needed to relate this pore-scale model to macroscopic foam behavior.

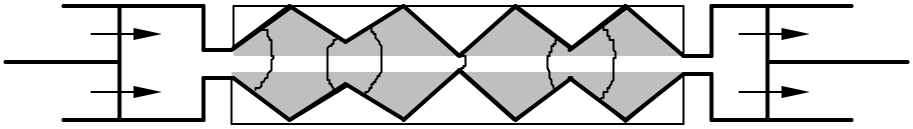

Figure 2.1 Schematic of bubble train in porous media.

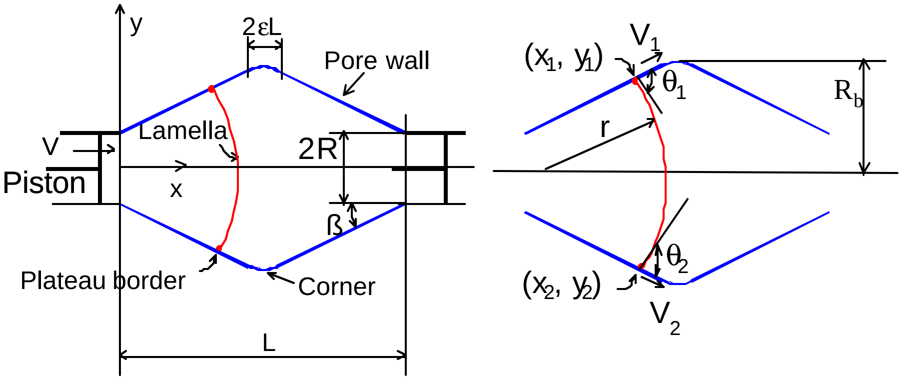

Figure 2.2 Geometrical pore model.

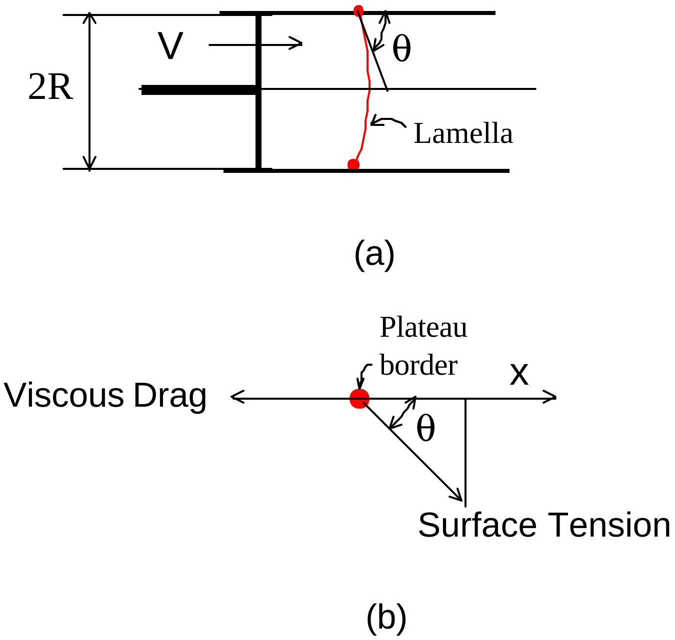

Figure 2.3 (a) Moving lamella in a straight channel. (b) Force balance on Plateau border.

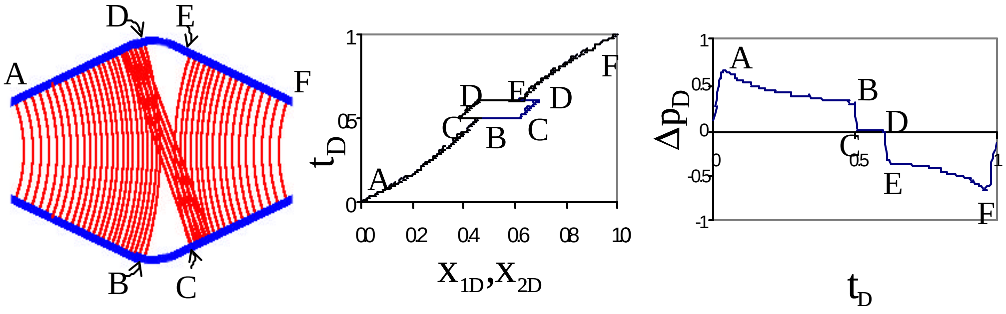

(a) (b) (c)

Figure 2.4 (a) Sequence of lamella shapes with asymmetric jump. (b) Positions of Plateau borders during sequence; split in path corresponds to asymmetric jump. (c) Pressure drop as function of dimensionless time during sequence. Parameter values: V_D = 2.9 E-5, ε = 0.05, R/L = 0.125, β =22.5°.

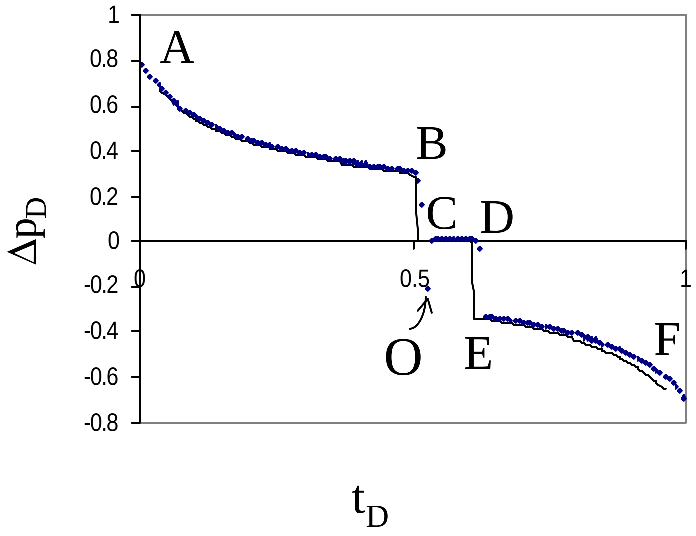

Figure 2.5 Dimensionless pressure drop as function of dimensionless time. Solid line is plot from Figure 2.4(c) , at lower velocity. Parameter values: V_D = 0.0058, ε = 0.05, R/L = 0.125, β =22.5°.

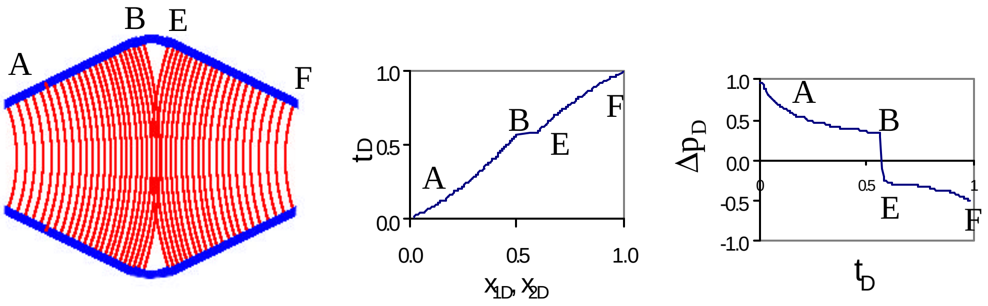

(a) (b) (c)

Figure 2.6 (a) Sequence of lamella shapes with symmetric jump. (b) Positions of Plateau borders during sequence: horizontal segment in path corresponds to symmetric jump. (c) Pressure drop as function of dimensionless time during sequence. Parameter values: V_D =0.006, ε =0.05, R/L = 0.125, β =22.5°.

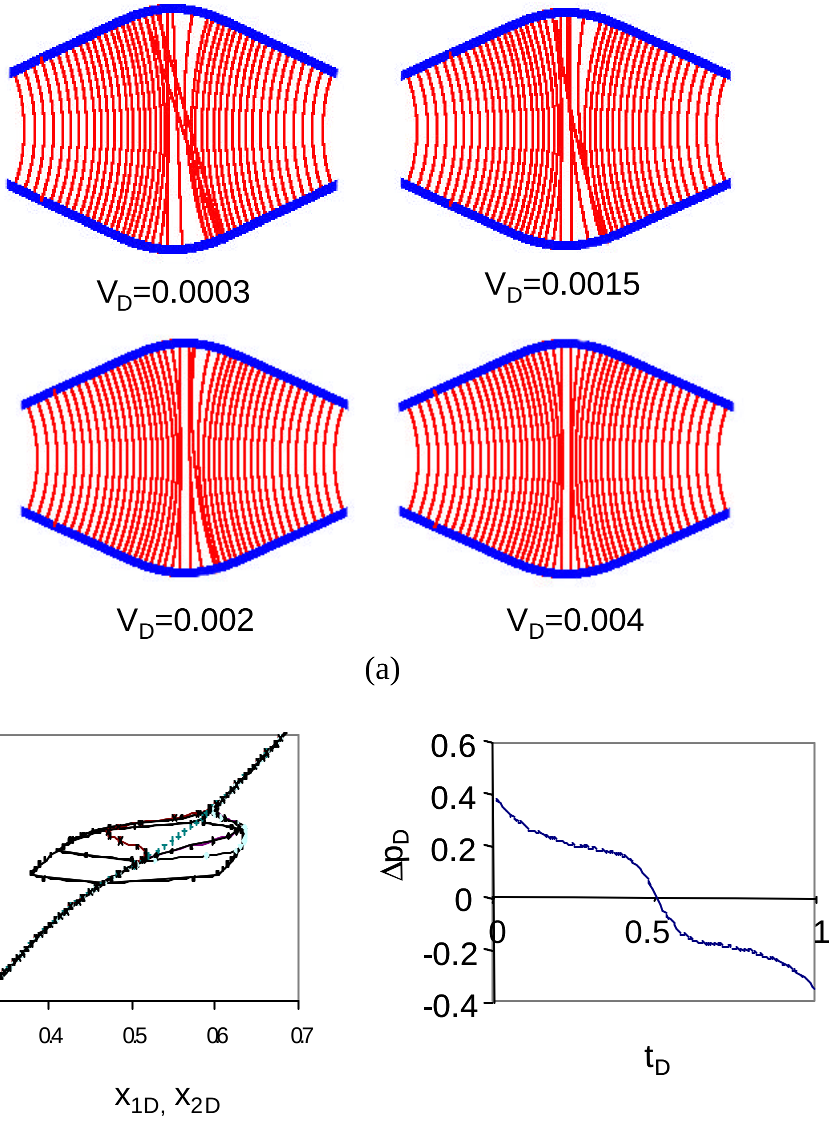

Figure 2.7 Transitional behavior with gently rounded pore corner. (a) Sequence of lamella shapes . (b) Positions of Plateau borders during sequence; splits in paths correspond to jumps. (c) Pressure drop as function of dimensionless time, for $V_D = 0.004$. Parameter values: $\varepsilon = 0.14$, $R/L = 0.125$, $\beta = 22.5^o$.

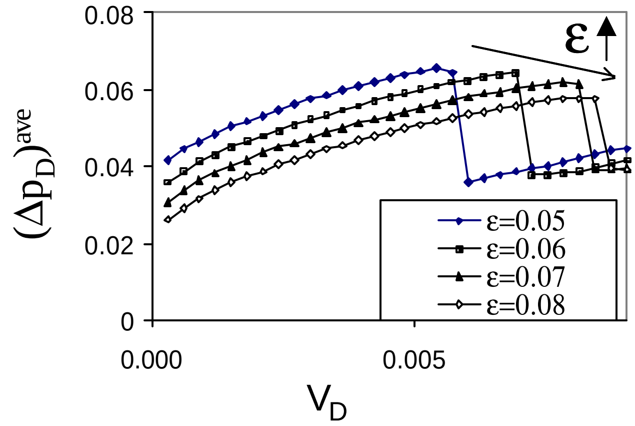

(a)

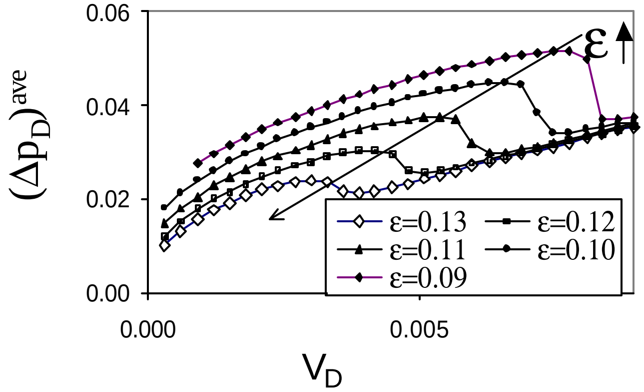

(b)

Figure 2.8 Dimensionless average pressure difference as a function of dimensionless velocity V_D. (a). Discontinuous transition in pores with sharp pore corners. (b). Continuous transition in pores with more rounded pore corners. Parameter values: R/L =0.125, β = 22.5°.

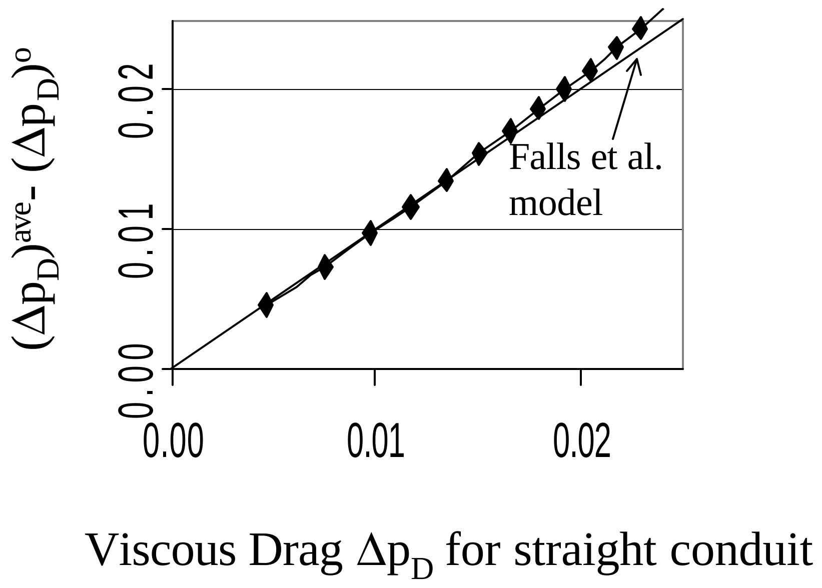

Figure 2.9 Comparison of viscous drag in wedge-shaped pore and straight conduit. Parameter values: $\varepsilon = 0.05$, $R/L = 0.125$, $\beta = 22.5^o$.

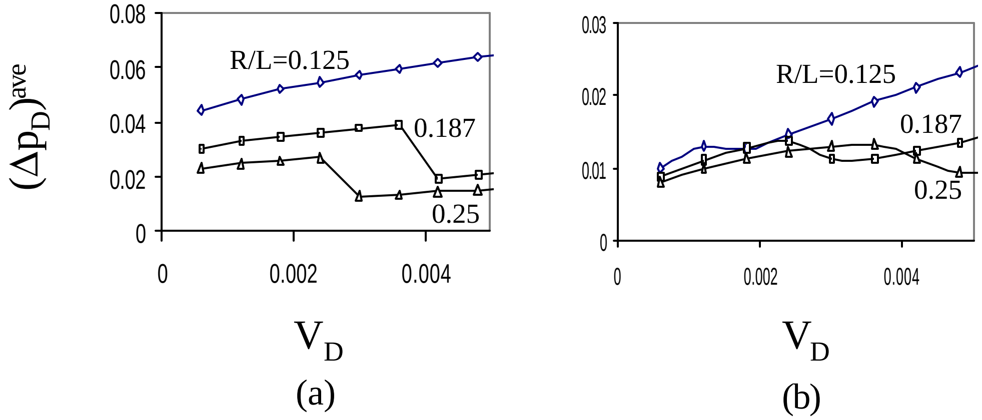

Figure 2.10 Dimensionless average pressure difference as a function of dimensionless velocity V_D. (a). Discontinuous transition in pores with sharp pore corners: $\varepsilon = 0.05$, $\beta = 22.5^o$. (b). Continuous transition in pores with more rounded pore corners: $\varepsilon = 0.14$, $\beta = 22.5^\circ$.

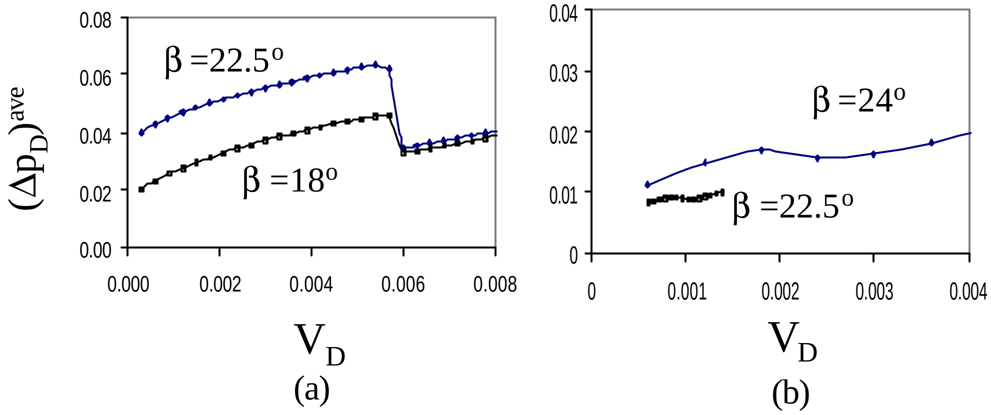

Figure 2.11 Dimensionless average pressure difference as a function of dimensionless velocity V_D. (a). Discontinuous transition in pores with sharp pore corners: ε = 0.05, R/L=0.125. (b). Continuous transition in pores with more rounded pore corners: ε = 0.14, R/L = 0.125.

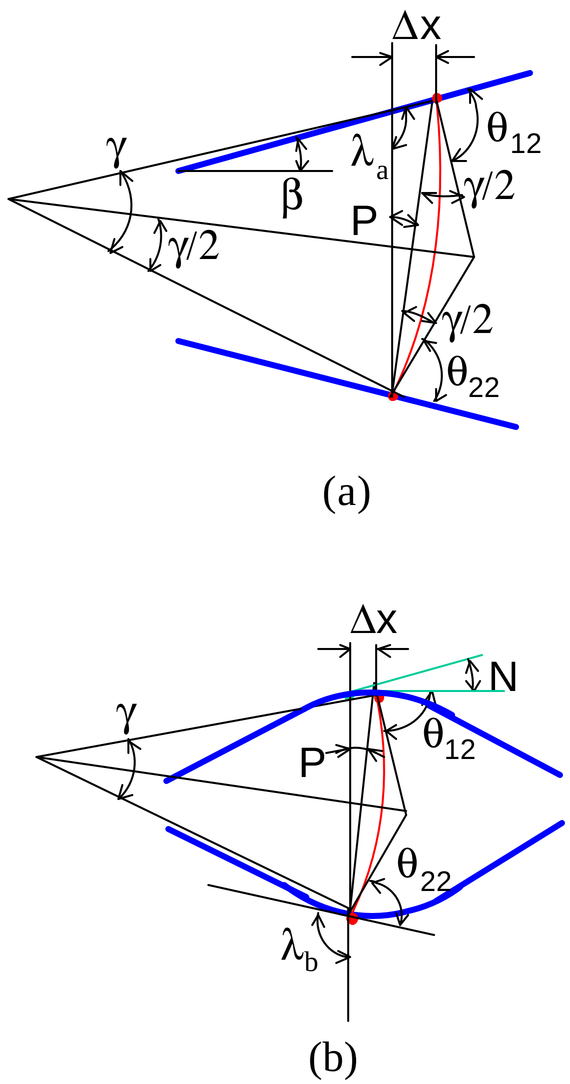

Figure 2.12 Illustration of analysis of stability of symmetric lamella shape at pore wall and pore corner.

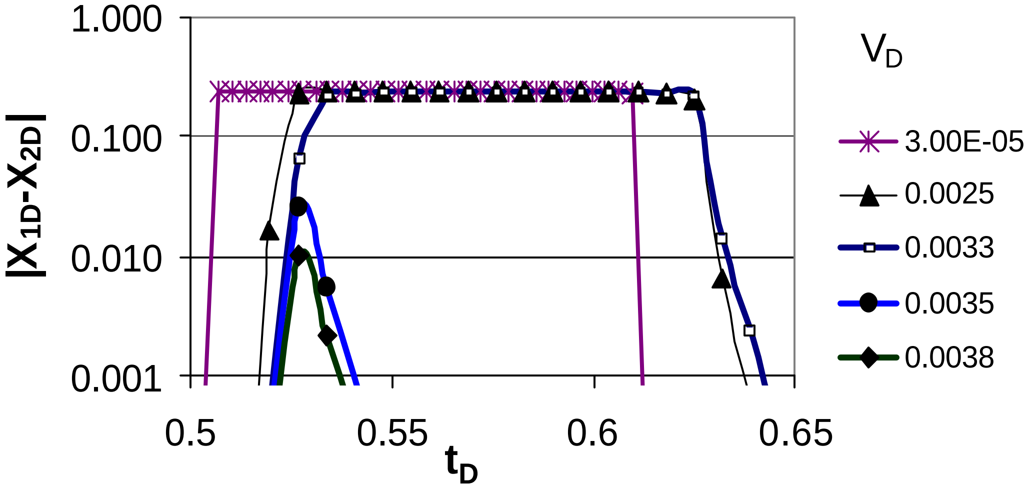

Figure 2.13 Growth of perturbation under different velocities. Parameter values: $\varepsilon = 0.05$, R/L=0.125, $\beta = 22.5^{o}$.

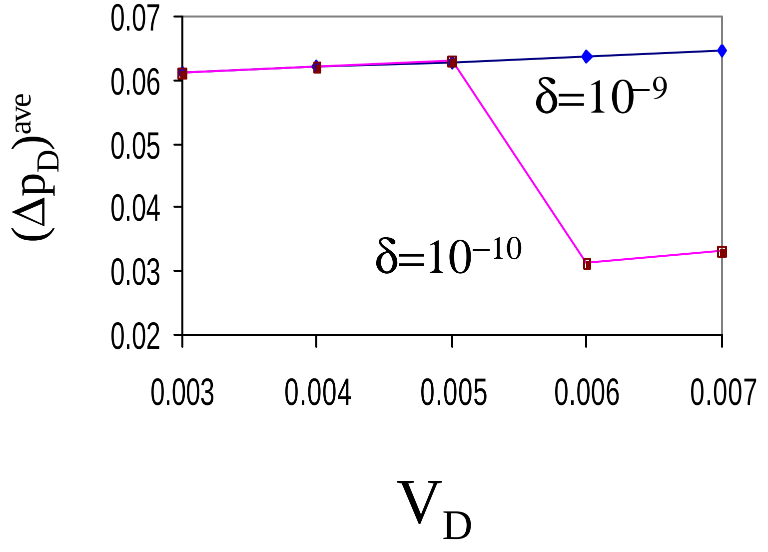

Figure 2.14 Average dimensionless pressure drop as function of dimensionless piston velocity V_D for two values of perturbation δ. Sudden drop in $(\Delta p_D)^{ave}$ corresponds to disappearance of asymmetric jump. Parameter values: $\varepsilon = 0.05$, $R/L = 0.125$, $\beta = 22.5^{\circ}$.

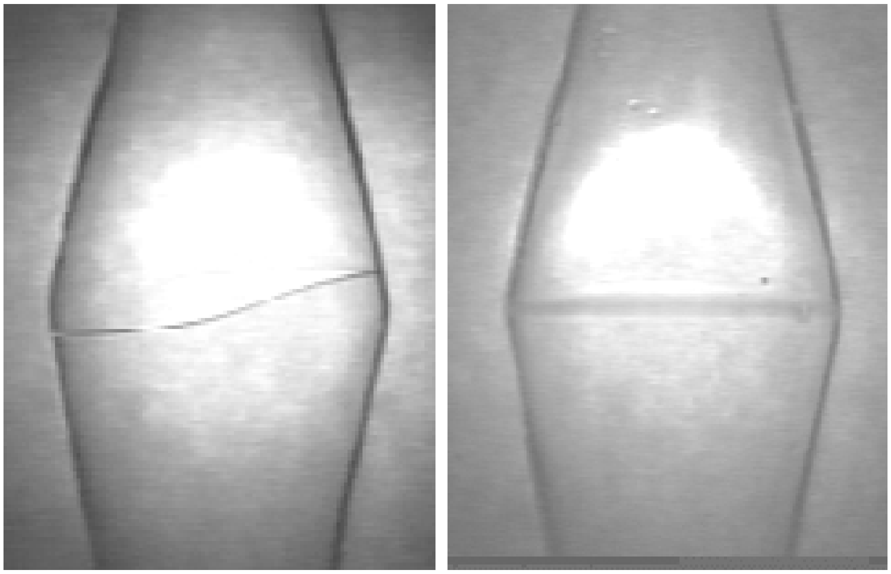

(a) (b)

Figure 2.15 Experimental verification of asymmetric lamella movement at low velocity and symmetric movement at high velocity in glass pore 10 cm long and 4 cm wide.

Chapter 3: Experimental Materials and Method

3.1 APPARATUS

Our experiments on SAG-foam processes and post-foam liquid injection utilized a general-purpose coreflood apparatus, shown in Figure 3.1. This apparatus is equipped with liquid pumps, nitrogen supply, gas mass-flow controller, electronic balance, back-pressure regulators, data-acquisition system, flow lines, etc.

A liquid pump, either an ISCO syringe pump (LC-5000, ISCO Inc, NE) or a reciprocating pump (Milton Roy Constametric 3000, Riviera Beach, FL) delivers liquid to the apparatus at a preset, constant volumetric flow rate. The range of liquid injection rate applied in this study with the ISCO pump is from 0.75 cc/hr to 30 cc/hr. The ISCO syringe pump has a finite reservoir (750 cc) in the syringe to store liquid. Upon depletion of this reservoir, the pump must be stopped and refilled. For cases where a significant injection rate needs to be held constant for long time, the reciprocating pump is used. The range of injection rate applied in this study with the reciprocation pump is from 0.5 cc/min. to 10 cc/min. Since the reciprocating pump takes liquid from an external container, there is no limit to how long it can run. The reciprocating pump is not as accurate as the syringe pump, especially at low flow rate. Both kinds of pumps have a control panel to preset desired flow rate, but they don't have outputs to the computer. Therefore liquid injection rate needs to be recorded manually.

Gas flow is regulated with a gas mass-flow controller (5850 TR, BROOKS Instruments, NY) (referred to as “controller” in the text that follows). This controller delivers gas from the nitrogen supply at a preset nominal volumetric injection rate, in units of standard cc per minute at 70^{o} F and 1 atmosphere pressure. It also measures the actual volumetric injection rate in those units in case flow rate differs from the set value and sends this value to the data-acquisition system. The actual volumetric flow rate varies with pressure, due to gas compressibility; the higher the pressure, the lower is the actual volumetric flow rate at same preset flow rate.

The controller works best with a fixed pressure difference of 50 psi across it. It may deliver at a slower rate, or not at all, if the pressure differential is too small. During a co-injection of liquid and gas, caution needs to be taken to avoid building pressure downstream of the controller higher than that upstream. That is possible if the apparatus is plugged or the flow encounters extremely high resistance; in such a case, continuing liquid injection can force liquid flow back into the controller and may damage it.

Gas and liquid meet before they flow into the core. In some experiments, a foam generator was used upstream of the core. A foam generator is a porous medium, usually with a smaller radius than the core, so that fluid flows at higher velocity through it. Higher velocity is a favorable condition for foam generation (Rossen and Gauglitz, 1990).

3.2 FLUIDS

The surfactant solution was prepared with distilled water. Surfactants used were Bio-terge AS-40 (STEPAN Company, Northfield, IL) and Shell NEODOL 91-8 surfactant (Shell Chemical Company, Houston, TX) at various concentrations. Both brine and surfactant solutions contain 1.0 wt % NaCl (i.e., 1 gram $NaCl_2$ in 99 gram water) and 0.02 wt% $CaCl_2$ to control clay swelling and to prevent possible fines migration. In preparation of surfactant solutions, all chemicals were stirred in water for at least 60 minutes. There were no signs of surfactant precipitation in any cases.

Industrial-grade nitrogen, stored in cylinders, was used in experiments as the gas. A pressure regulator is attached to the nitrogen cylinder to release nitrogen to the test system at any desired pressure that is lower than the cylinder pressure; a full cylinder has a pressure up to 3,000 psi.

No oil was present in the cores in any of the experiments.

3.3 CORE AND CORE PREPARATION

Unfired Berea sandstone cores, with permeability of around 300 md and porosity of around 0.21, were used. Cores were 1 foot long and 2 inches in diameter. Cores were cut parallel to the bedding plane.

A core is assembled with a section of PVC pipe (schedule 80, 2 ½ inch ID, 12 1/2 inches long), two PVC end-caps, two distributing caps and four fittings. The rock core is sealed inside PVC pipe with epoxy and connected with the flow system through drilled ports as shown in Figure 3.2(a).

The following is the procedure of core preparation: Machine two NPT-thread ports into the PVC pipe at 4-inch intervals along the pipe to allow measurements of pressure in three sections along the core. Machine NPT-thread ports on each end-cap. Using a quick-solidifying epoxy, fill the flow channel inside three of the four fittings, to prevent epoxy from flowing out in later steps. Screw these three fittings tight enough into the two ports on the PVC pipe and on the bottom end-cap using Teflon tape (Figure 3.2).

Two distributing plates, made of Plexiglas, are used to distribute fluid evenly at the core injection face and outlet face. Machine flow channels on the side of these plates that contact the rock to distribute fluid (Figure 3.2(b)). Attach the plates to each end of the core using adhesive tape.

Put the rock core inside the PVC pipe (without the end-caps attached yet). With the distributing plates attached, the core has the same length as the PVC pipe. A plastic quick-solidifying epoxy (i.e., one that is deformable before it solidifies) can be used to position the core at the center of the PVC pipe (Figure 3.2(c)). Then cement the two PVC end-caps on to the PVC pipe, using conventional cleaner and glue sold for connecting PVC pipe. Prepare 600 cc of “Armstrong” Epoxy Resin (Resin Technology Group, Easton, MA) in a large paper cup for each core assembly, stirring until it is well mixed. Use a supporting frame to hold the core assembly upright. With the top end-cap still open (no fitting installed yet), use a funnel to *slowly* pour the prepared epoxy into the core through the top opening, making sure to fill the core holder completely. Wait for at least two days for the epoxy to completely harden.

Reopen the port on the top end-cap and screw in the last fitting. Then use a small drill bit to drill through all the ports, until the bit just hits the rock. Clean all ports with laboratory air supply (at 100 psi). Test connectivity of all ports with the air supply, by connecting one port to the air supply and opening each of the rest ports one at a time. The core assembly now is ready for installing into the apparatus.

3.4 DATA ACQUISITION

Pressure differences along the core are measured using pressure transducers (Validyne, Validyne Engineering Sales Company, Northridge, CA). The range of the transducer diaphragms is 0-80 psi in these experiments, and according to the manufacturer transducers are expected to measure pressure difference as small as 1 psi accurately. All transducers are calibrated before and after experiments.

Pressure drop was measured separately in three sections along the core. During a foam injection, gas and liquid mix and foam is generated (or altered from an initial texture if a foam generator is placed upstream of the core) in the first few centimeters of the core (Ettinger and Radke, 1992). Pressure in the first section then could be unrepresentative of steady-state flow. In the third section, the capillary end-effect increases water saturation at the end of the core. Because foam mobility is so sensitive to water saturation, pressure drop in section two is therefore considered the most reliable source of pressure data. However, if section 1 matches the section 2 pressure drop, both pressure drops can be taken as indicative that entrance effects are minor and that both sections accurately reflect steady-state flow. Likewise, if section 3 matches the section-2 pressure drop, it indicates that the capillary end-effect is unimportant in this case and that both section 2 and 3 reflect steady-state flow.

Strictly, if both gas and liquid are present, measured pressure drop is gas-phase pressure drop, since gas is the non-wetting phase and occupies larger pores and also the space inside a fitting.

Analog signals from the pressure transducers and gas mass-flow controller feed into a data-acquisition card (PC-LPM-16/PnP, National instrument, Austin, TX). A LabView (National instrument, Austin, TX) program takes signals from the data-acquisition card and displays and saves these measurements.

3.5 WEIGHING THE CORE

Water saturation is measured by weighing the core. Saturation is calculated from the electronic balance reading and known core pore volume. For example, starting with a tared balance reading of zero with the core fully saturated with liquid, if later the electronic balance reading averaged –97 g in steady-state foam flow, the negative number would represent that the core was lighter than at the fully-liquid-saturated condition. Then, with a core pore volume of 145 cc, for example, water saturation would be

$$(145-97)/145 = 0.33 .$$

An electronic balance (LC-4000, Satorius, Satorius Corp., NY) with a special digital RS232 output, continuously monitors the weight of the core for determination of core-average liquid saturation. A LabView program modification based on the “advanced data logger,” which is available in the “solution gallery” of the standard LabView program, was used for data acquisition. The digital signal of weight and all other analog signals can be periodically logged into computer. In these experiments, readings were taken every 2 minutes. The balance can take readings as often as twice per second, allowing it to record rapid saturation changes. This balance has a capacity of 5 kg and sensitivity of 0.01 gram. For a core with a pore volume of 145 cc, a change of 0.01 g corresponds to a fractional change in saturation of 0.01/(145) = 0.00007, or 0.007 %. The balance itself is not a limiting factor for precisely measuring average water saturation.

Measurement accuracy *is* limited by other factors. The objective is measuring the liquid saturation in the core. However, the weight of fluid in part of the flow lines, distributing plates, and fittings (volume other than rock pore volume, referred to as dead volume) is also measured along with the core. We estimate dead volume included in core weight at under 2 cc, based on the volumes of plates and diameters and lengths of flow lines. It is reasonable to assume that fluid flows through the dead volume with liquid fraction equal to the imposed fractional flow f_w. Fortunately, changes in f_w are relatively small through most of our data, but an uncertainty of core weight of order 1g (0.7% in S_w) could be attributed to uncertainty in the weight of the dead volume, with much smaller uncertainty when changes in f_w are small. If foam quality doesn’t change much, dead volume is not expected to be a problem.

Pressure-induced load may also act on the balance, appearing as a weight change. A large pressure acting on even the small cross-sectional area of a transducer line could in principle induce a measurable load on the balance. Pressure changes on flow lines and transducers lines could also stiffen the flexible lines, changing their mechanical properties. We use stainless steel rigid horizontal lines up to within 1 inch of the core; flexible lines made of nylon then connect to the core (Figure 3.3). The dotted line in Figure 3.3 defines a system for a force balance on the apparatus. Theoretically, pressure-induced loads induced by the transducer lines should be zero, because horizontal lines don't involve any vertical force, unless pressure alters the mechanical properties of the flexible lines. We ran several tests by applying pressures with gas and checking the change in reading of the balance; the induced weight was less than 1 gram/100 psi of absolute pressure.

As a direct check on the possible mechanical support offered by the flow and transducers lines, a piece of metal of known weight (18.0 g) was put on top of the core holder. The reading of the balance reflected the known weight at 18.0 g both with a static pressure of 150 psi acting on the core and flow and transducer lines, and without pressure acting in the system. This result suggests that the flexible lines don't support or affect the measured weight of the core holder.

The electronic balance reading can drift over long periods of time. Tests show drift is smaller than 0.2 g over 24 hours in a random-basis, and the reading doesn't drift away over a week. Twenty-four hours is a time sufficient for most post-foam liquid injection experiments (Chapter 5) to be completed. For SAG experiments (Chapter 4), a whole experiment takes as long as one week, but saturation changes occur in much short time period.

Overall, we estimate precision of the measurement at about 1-2 grams, giving effects of dead volume, pressure-induced load and drift accounted for. Fortunately, the total weight changes in the experiments are an order of magnitude larger than 2 grams during the transition period in post-foam liquid-injection experiments and foam quality doesn't change much over a short time in SAG-process experiments.

Using an electronic balance sets limits for choices in these experiments. Total weight on the available balance was limited to 5 kg; thus only a light core holder could be used. Light PVC is readily available but it has a low strength: 2.5-inch ID PVC pipe has pressure rating of about 500 psi, and flexible nylon flow-lines have about the same pressure rating. Therefore, back-pressure was set at only 150 psi, the pressure build-up across the core was then limited to a few hundred psi. Previous foam experiments have built up pressure drops of 600-800 psi over a 1-ft core (Kibodeaux *et al*. 1994; Zeilinger *et al*. 1995); therefore, we chose to use relatively low surfactant concentration, low flow rates, and high foam quality.

3.6 BACK-PRESSURE REGULATOR

A back-pressure regulator (BPR) maintains a constant pressure upstream of the BPR equal to a set pressure (dome pressure), by blocking flow until upstream pressure reaches the dome pressure. There are two back-pressure regulators used in this apparatus. One is a “Mity Mite” (Grove Valve & Regulators, Oakland, CA) BPR installed downstream of the gas mass-flow controller. To ensure a 50 psi differential pressure across the controller, the dome pressure of the BPR is set at 50 psi lower than the nitrogen supply, so that the pressure across the controller is always kept at 50 psi. In most experiments, the nitrogen supply pressure was set to 500 psi, and the dome pressure of this BPR was set to 450 psi.

The other BPR (BPR-50, Temco Inc., Tulsa, OK) is installed at the outlet of the apparatus to hold the core at an elevated pressure to reduce the effects of gas expansion. For example, if a pressure drop across the core were 3 atm., without back-pressure, inlet pressure would be at 4 atm and outlet pressure 1 atm.; gas would expand by a factor of four from inlet to outlet. Gas velocity at steady state would also increase by a factor of four, from inlet to outlet, making interpretation of the data difficult. With a back-pressure of 10 atm., the inlet pressure would be 13 atm for the same pressure drop of 3 atm., and gas expands by a factor of only 1.3 from inlet to outlet. The higher the back-pressure is, the lower the effects of gas expansion for the same pressure drop across core. There is no way to eliminate gas expansion completely.

A separate nitrogen cylinder was used for the dome pressure of the BPR at the outlet of the apparatus. To compensate for a persistent, very slow leak somewhere in the line, the cylinder was continuously connected to the dome to ensure a constant dome pressure over each experiment. A transducer continuously measured pressure difference between the dome and inlet of this

BPR to indicate if the BPR malfunctioned during an experiment. In experiments reported here, no BPR malfunction occurred.

Occasionally in other experiments not reported here the BPR malfunctioned, i. e. it dropped 20-50 psi in a short time before slowly rebuilding pressure. This led to the following adjustments. It appeared that abrupt changes in injection rates coincide with some malfunctions, and two-phase flow through the BPR can also cause problems with a BPR. To minimize problems, we tried to avoid sudden injection-rate changes during an experiment and restrict flow through the BPR to gas only. For the latter purpose a Jerguson cell (Jerguson Gage company, Upper Saddle River, NJ) was used as a foam breaker just upstream of the BPR (Figure 3.1). A Jerguson cell has two openings, one on the top and one at the bottom. It also has a transparent wall on one side. Silicon oil filled about one third of the cell. Foam flowed into the cell through a line from the top of the cell nearly to the bottom. Foam bubbles break as they contact the silicon oil; liquid sinks to the bottom, and gas rises to the top, where it flows out through a second line to the BPR. A third flow line connects the bottom of the cell to a needle valve, which can be opened to drain liquid. Care must be taken to drain the liquid slowly.

3.7 ALTERNATIVE EXPERIMENTAL TECHNIQUES

Weighing the core was the method used to measure liquid saturation in these experiments. The method was convenient and accurate, but it set limits for the core weight, and consequently for the material of core holder and pressure build-up, which limits the scope of the study. Here we briefly discuss some alternative techniques.

PEEK (PolyEtherEtherKetone) is a synthetic material that is much stronger than PVC, yet a light material. Using PEEK material for the core holder would allow higher pressures in the apparatus. We used PVC primarily because PVC is readily available and inexpensive.

It is possible to use much heavier core holder, like a steel Hastler-type core holder, and still use this electronic balance to measure *weight change*. Instead of having the whole core assembly sit on top of the balance, the weight of core assembly could be balanced with a dead weight through a mechanical device like a pivot. Thus, the electronic balance readings would reflect weight change, which is expected to be small, rather than the entire weight of the core assembly.

Computerized X-ray Tomography (CT) has been used in laboratory coreflood studies for porosity and saturation measurements (Donald *et al.*, 1993; Bartko *et al.*, 1995; Akin *et al.*,1996; Bertin *et al.*, 1998; Chen, *et al.*, 2000; Apaydin and Kovscek, 2001). These studies are briefly reviewed here.

Donald *et al.* (1993) used CT to determine water saturation in cores. Their visualization of 3D fluid distributions inside porous media shows that the assumption of uniform fluid saturation was violated during parts of the experiments. Without having used CT, this uneven distribution of water would have been overlooked.

Bartko *et al.* (1995) used CT scan to visualize acid treatments in core samples. Density distribution along the core and over core cross-sections was measured at different times in the simulated acidizing process. Quantitative measurement of porosity changes was obtained.

Akin *et al*. (1996) conducted a theoretical error analysis of water saturation measurement using CT. They reported an uncertainty of slightly less than 6%.

Bertin *et al*. (1998) used CT scans to measure porosity and aqueous-phase saturation fields. Total time needed for one cross-sectional scan was about 47 seconds. Many cross-sections are needed for a full 3D scan.

Chen *et al*. (2000) monitored surfactant imbibition in an oil-saturated core using CT. Spatial fluid movement and saturation distributions were acquired and compared with mass-balance data. CT results for ultimate pore-volume oil recovery were within 6.5% of those obtained using the mass balance.

Apaydin and Kovscek (2001) concluded, “in practice, repeated measurement of porosity and static water saturation on this particular CT scanner, including the positioning system, displays errors of 1-2%”.

Magnetic resonance imaging (MRI) is another technology that has been utilized in laboratory coreflood tests to determine water saturation and core porosity.

Wegener and Harpole (1996) used magnetic resonance imaging (MRI) to screen core plugs for internal, hidden heterogeneities prior to flow testing.

Wassmuth *et al*. (2001) demonstrates the application of magnetic resonance imaging to steady and unsteady-state foam flow in porous media. They estimated the accuracy of the water saturation measured by the MRI instrument is within 5% of the actual value.

CT and MRI provide some advantages for laboratory saturation measurement. In particular, spatial variation of saturation can be resolved. However, a measurement accuracy of 5-6% doesn't satisfy objectives of measuring subtle saturation changes like those in these experiments. The weighing method can also resolve changes in saturation more rapidly than can be resolved by CT or MRI. An uncertainty of even 1-2% with CT or MRI is comparable to that of the weighing approach according to our estimate.

3.8 DETAILED EXPERIMENTAL PROCEDURES

3.8.1 Porosity measurement

Porosity was measured for each new core following these procedures:

- Connect vacuum pump to the outlet of the core; close or cap all other ports on the core and valves. Turn on vacuum pump for at least 4 hours.
- Fill a graduated cylinder with brine. The amount of liquid in the cylinder should be much greater than the estimated pore volume of the core. Place the outlet line of the core in the brine, with the outlet valve still closed.
- Stop the vacuum pump. Open the valve to connect the core with the graduated cylinder, allowing brine to be drawn into the core.

Wait until the level of brine in the cylinder is stable. Measure the volume drawn out of the cylinder.

- Subtract from this volume the volume within end-caps and flow lines, to obtain the volume of brine actually filling the core pore space. This is the core pore volume.
- Porosity is calculated from the bulk volume of the core and the volume of the pore space.

3.8.2 Permeability measurement:

For each new core, permeability is measured with brine after the porosity measurement. Measurement of permeability k is based on Darcy's law:

$u_w = (k/\mu)\ (\Delta p/L)$,

$k = (u_w \mu)/(\Delta p/L)$

where u_w is liquid superficial velocity (i.e., volumetric flux); brine viscosity μ is taken as 1.0 cp (0.001 Pa s); Δp is pressure difference; and L is core length. In the measurements, u_w was set at a fixed value, and pressure drop was measured accordingly. Measured permeabilities ranged from 295 md to 320 md for the Berea sandstone cores used.

3.8.3 Initial condition

The procedure for establishing an initial condition in the core is as follows.

Install the core assembly in the apparatus. Connect inlet and outlet flow lines and pressure taps. Zero the pressure transducers if necessary. Set dome pressure on the downstream BPR to 150 psi (gradually, to avoid damage of the diaphragm inside the BPR; a needle valve in the gas line to the BPR dome helps for this purpose).

Prior to injecting gas, zero the balance. At this time, the core is saturated with liquid and the “zero weight” serves as a reference point for saturation calculations. For experiments in which the core doesn’t start with a fully-saturated condition, normally the core was flushed with surfactant solution with alternating back-pressure between 150 psi and zero 3 times to displace as much gas as possible. In retrospect, it would have been better to use brine in this step.

3.8.4 Foam flow

All the experiments described in this work start with a steady-state foam flow. The procedure to reach a steady-state foam flow is as follows. Inject gas and surfactant at desired injection rates. The apparatus always starts at low pressure because the vapor in the foam separator (Jerguson cell) is initially at zero back-pressure (Figure 3.1). Therefore the actual gas flow rate is high initially. Fluid then accumulates and gas is compressed within the core, flow lines and the Jerguson cell until pressure in the system also reaches the back-pressure setting, at which point the outlet BPR opens and maintains constant outlet pressure.

During this process, liquid and gas flow rate may need to be increased to favor foam generation. After generation of foam (inferred from pressure response), gradually reduce the injection rates to the desired injection rates for steady-state foam flow. Then wait for a sufficient time for foam to reach steady state in the core.

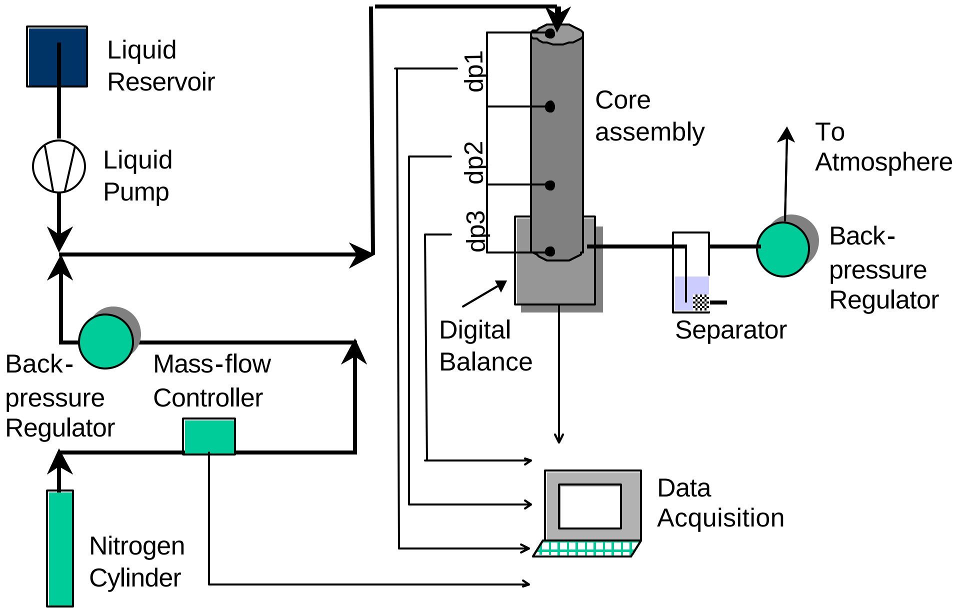

Figure 3.1 Schematic of the coreflood apparatus

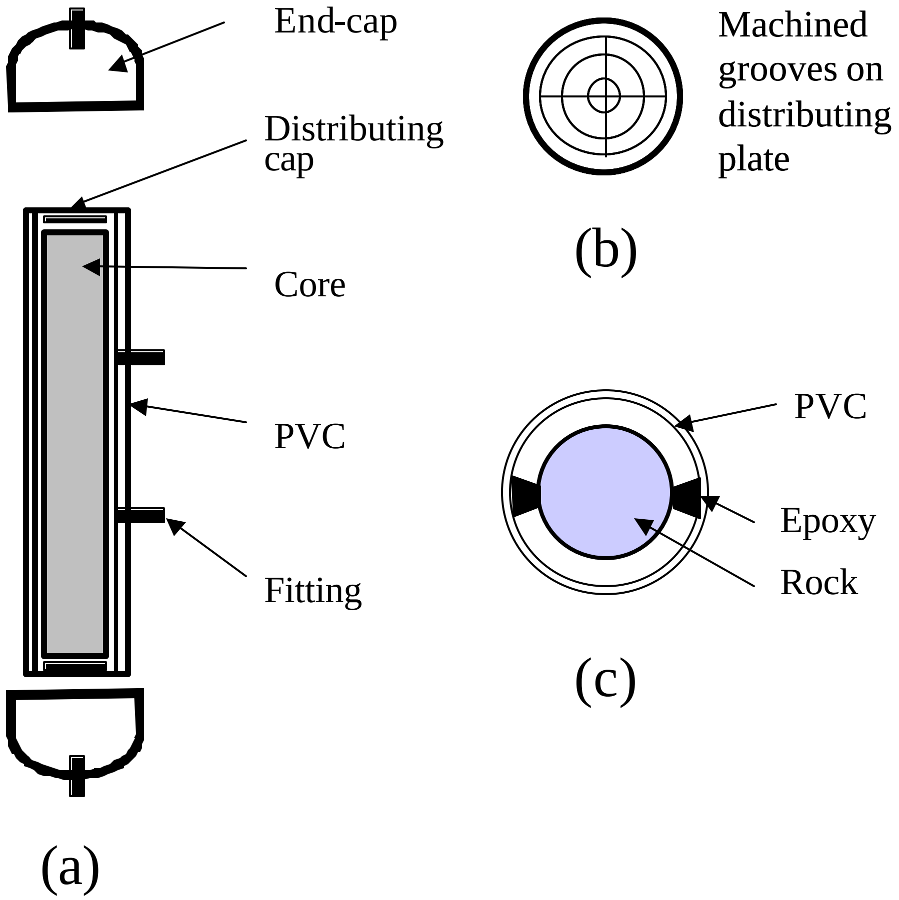

Figure 3.2 (a) Detailed schematic of core assembly. (b) Machined distributing plate. (c) Schematic of end of core, showing that the initial epoxy hardens and centers the core in the PVC pipe; the remaining annulus between the core and the PVC pipe is to be filled with additional epoxy.

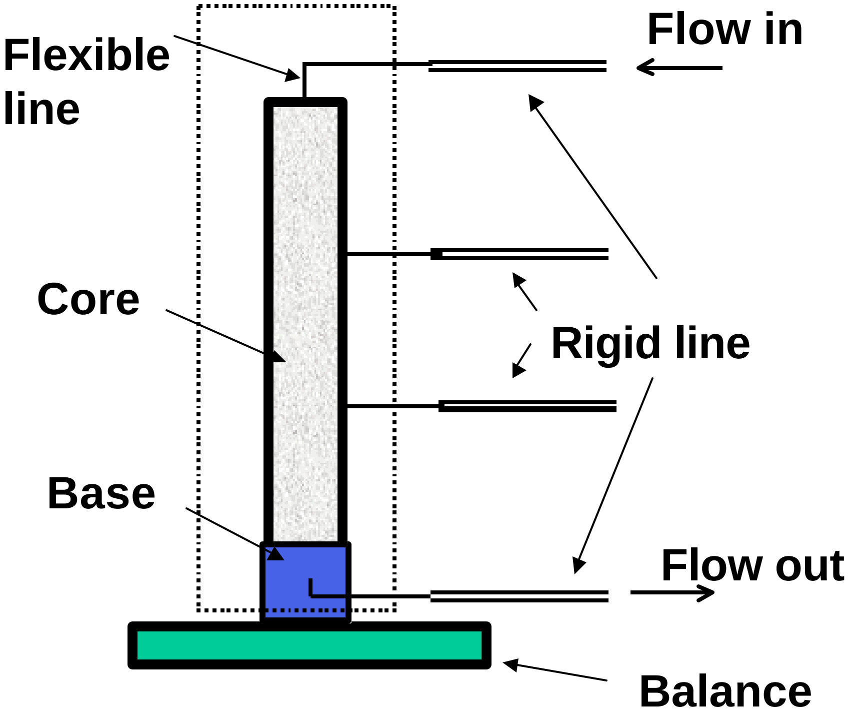

Figure 3.3 Detailed schematic of core-weighing apparatus. Dotted line indicates system on which force balance (detailed in text) is based. Rigid tubing is indicated by double lines on figure, flexible tubing by single-width lines on figure.

Chapter 4: Experimental Investigation of Surfactant-Alternating-Gas Injection Processes

4.1 INTRODUCTION

4.1.1 Surfactant-alternating-gas processes

Foams for gas diversion can be placed in the reservoir by continuous co-injection of surfactant solution and gas or by injecting alternating slugs of surfactant solution and gas (surfactant-alternating-gas, or SAG, injection).

Different foam-injection strategies have been used in field trials due to stratigraphic differences, foam behavior and operational concerns. Shan and Rossen (2002) list 11 foam field trials with CO_2, N_2, air or hydrocarbon-gas foams (Holm, 1969; Chad *et al.*, 1988; Liu and Besserer, 1988; Jonas *et al.*, 1988; Kuehne *et al.*, 1990; Chou *et al.*, 1992; Krause *et al.*, 1992; Hoefner *et al.*, 1994; Aarra *et al.*, 1995; Martin *et al.*, 1995; Svorstol *et al.*, 1996; Blaker *et al.*, 1999). Among these field trials, there are six cases of co-injection of gas and liquid, seven of SAG injection at fixed injection rates, and two of SAG injection at fixed pressure (several projects include trials of more than one injection strategy). Blaker *et al.* (2002), and Skauge *et al.* (2002) also report a more recent, successful SAG injection field trial in the Snorre field. The main operational conclusion from the field trials is that SAG injection is preferable to co-injection. Skauge *et al.* estimate that the SAG treatment in the Snorre field has contributed approximately $44 million dollars worth of oil at a hypothetical cost of the treatment (i.e., if repeated routinely) of approximately $1 million in this project.

SAG injection has several advantages over co-injection. It minimizes contact between water and gas in surface facilities and piping, which can be important if the gas, for instance CO_2, forms an acid upon contact with water (Mattews, 1989; Heller, 1994). Alternating injection of small slugs of gas and liquid can promote foam generation in the near-well region (Rossen and Gauglitz, 1990). SAG injection also improves injectivity; as water is displaced from the near-well region during gas injection, foam weakens there, gas mobility rises and injectivity increases. Injectivity is especially important in low-permeability formations, where injection rate can be limited by fracture pressure due to low foam injectivity (Holm, 1969; Jonas *et al.*, 1988; Kuehne *et al.*, 1990).

If foam has disappeared from the entire formation rather than merely weakened in the near-well region, however, the process fails. This could occur if foam generation fails late in the process. There are number of reasons for this concern. First, some research finds that foam generation requires high pressure gradients normally attainable only in the near-well region (Rossen and Gauglitz, 1990; Friedmann *et al.*, 1991; Gauglitz *et al.*, 2002), although other research disagrees (Chou, 1991). The minimum pressure gradient for foam generation depends on gas-liquid interfacial tension (Rossen and Gauglitz, 1990), which is much lower for CO_2 foams than for the N_2 foams used in many laboratory studies of foam generation (Rossen, 1996, Gauglitz *et al.*, 2002). Therefore, this effect may not be as important for CO_2 foams used in SAG processes. Moreover, a fixed-pressure SAG process focuses most of the well-to-well pressure drop on the displacement front where foam forms (Shan and Rossen, 2002), so large pressure gradients are feasible far from the injection well. In this study we assume that foam generation is not a limiting factor.

Another reason for concern is that high-mobility gas near the well may finger through or override lower-mobility foam away from the well during gas injection. In a homogeneous formation, gravity override represents a worst case of fingering, with gravity and density differences, in addition to viscous instability, driving finger formation at the top of the reservoir. Simulation studies (Shi and Rossen, 1998; Shan and Rossen, 2002) suggest that at fixed *injection rates*, high mobility near the injection well promotes gravity override in a SAG process. More recent simulation results (Shan and Rossen, 2002) suggest that SAG processes at fixed injection *pressure* better control gravity override in homogeneous reservoirs than either continuous foam injection or a fixed-injection-rate SAG process. Gas and liquid should be injected at maximum possible injection pressure to minimize segregation and reduce surfactant slumping.

The success of SAG processes depends on many issues: injection rates, injection pressure, foam generation *in-situ*, injectivity, foam propagation, size of slugs, etc. Foam behavior and possible collapse during gas injection is one of the major concerns. Fractional-flow methods illustrate these concerns, as discussed in the next section.

4.1.2 Modeling SAG processes using fractional-flow methods

In modeling SAG processes with fractional-flow methods, one finds that the fractional-flow curve at extremely low water fractional flow f_w controls the displacement, because a Buckley-Leverett shock bypasses the rest of the fractional-flow curve. The next section discusses this point further. However, data at low f_w are scarce. For instance, Persoff *et al.* (1991) report steady-state foam mobility and water saturation for $f_w = 0.004$, but Shi and Rossen (1998) show that even these data do not suffice to predict the nature of a SAG displacement. This example is examined in detail in the next section.

Kibodeaux and Rossen (1997) studied the fractional-flow curve for one foam formulation in Berea sandstone. They show that foam is strong even at low f_w, until water fractional-flow f_w reaches a distinct point where foam abruptly weakens by a factor of more than 100. In addition, f_w is not a single-valued function of S_w. Combined with fractional-flow methods, their experimental results predict a successful field-scale SAG process under the conditions studied. Unfortunately, problems with the experiments made the measured water saturations uncertain. See Kibodeaux and Rossen (1997) for discussion.

Foam behavior under extremely dry conditions is investigated in this chapter. In these experiments, Berea sandstone core is used without oil. The surfactants used are Bio-terge AS-40 and Shell NEODOL 91-8. Water saturation was measured using an electronic balance to weight the core. A fractional-flow curve is presented for each surfactant formulation at one concentration. The fractional-flow curve obtained with Shell NEODOL 91-8 surfactant repeats

Kibodeaux and Rossen's (1997) finding of a multi-valued fractional-flow function. Foams are persistent, but weaken significantly at extremely dry conditions. Fractional-flow curves are obtained from laboratory experiments, and then fractional-flow methods are used to upscale laboratory coreflood data to a hypothetical 1D reservoir-scale displacement. Using fractional-flow methods, displacement patterns are predicted from experimental data, suggesting successful SAG foam processes under the conditions of the experiments.

4.2 APPLYING FRACTIONAL-FLOW METHODS TO SAG PROCESSES

4.2.1 Fractional-flow methods

Compared to simulation, fractional-flow methods (Buckley and Leverett 1941; Helfferich and Klein, 1970; Lake 1989; Zhou and Rossen, 1995) are easy to use, and capable of unraveling the essentials of displacements. With fractional-flow methods, one constructs a "time-distance" diagram for the displacement process from the fractional-flow curve. The displacement pattern can be read from this time-distance diagram. Water saturation at any specific position at any time is indicated on the diagram.

Fractional-flow methods make various simplifying assumptions, including immediate attainment of local steady state, an absence of viscous fingering, incompressible phases, one dimensional displacement, Newtonian fluids (i.e. independence of mobilities on total superficial velocity), and absence of chemical dispersion and gradients of capillary pressure.

Even in cases where the assumptions in fractional-flow theory do not apply quantitatively, fractional-flow methods help in unraveling the mechanisms of success or failure of foam processes (Rossen *et al.*, 1999). Fractional-flow methods can accommodate oil along with gas, water and surfactant (Zeilinger, 1996), but for simplicity here we consider SAG foam displacements in the absence of oil.

The fractional flow of water, f_w, is defined as

$$f_w=u_w/(u_w+u_g) \tag{4.1}$$

where Darcy's law gives

$$u_w= k_{rw}k(\Delta p/L)/\mu_w \tag{4.2}$$

$$u_g= k_{rg}k(\Delta p/L)/\mu_g \tag{4.3}$$

and u_w and u_g are water and gas superficial velocities (i.e., volumetric fluxes); k is permeability; k_{rw} and k_{rg} are water relative permeability and gas relative permeability; $\Delta p/L$ is pressure gradient; and μ_w and μ_g are the viscosities of water and gas. From Darcy's law, $k_{rw}k/\mu_w = u_w/(\Delta p/L)$ is the mobility of water. Mobility of gas is defined similarly. Removing permeability k from the expression for mobility, one gets the relative mobilities, λ_{rw} and λ_{rg}. Total relative mobility λ_{rt} is then the sum of the relative mobilities of water and gas.

Substituting Eqs. 4.2 and 4.3 into Eq. 4.1, one finds

$$f_w=[1+(\mu_w k_{rg}(S_w))/(\mu_g\, k_{rw}(S_w))]^{-1}. \tag{4.4}$$

The fractional flow of water f_w is thus a function of water saturation S_w and the viscosities of the two phases, as long as the relative permeabilities are functions of S_w alone.

For conventional gas-water flow (Lake, 1989) this condition is satisfied. Some studies (Zhou and Rossen, 1995; Rossen *et al.*, 1999) suggest that to a reasonable approximation, even with foam, relative mobilities are unique functions of S_w.

Applying mass conservation to the displacement (Lake 1989), one gets

$$d(f_w(S_w))/d(S_w)=X_d/t_d, \tag{4.5}$$

where X_d and t_d are dimensionless distance and dimensionless time respectively. Dimensionless distance X_d is the ratio of the pore volume between the injection face and a given location to the total pore volume; dimensionless time t_d is given in pore volumes injected. Eq. 4.5 says that the dimensionless velocity of a saturation wave (right-hand side) with saturation S_w travels at a velocity equal to the slope of the tangent to the fractional-flow curve at the same saturation (left-hand side). In other words, each given water saturation moves downstream on a “characteristic” line at a constant velocity determined by the fractional-flow function. Thus, with the fractional-flow curve, one can predict how saturation waves propagate, and the displacement behavior.

The solution given by Eq. 4.5 is called a “spreading wave” because the change in saturation starts at the inlet and spreads out through the core or reservoir over time. If Eq. 4.5 gives a solution that is non-monotonic in velocity, however, then some values of S_w are jumped over in the solution. These saturations are replaced by a Buckley-Leverett shock front, a discontinuity in saturation (Lake, 1989). The velocity of the Buckley-Leverett shock is given by

$$\Delta f_w/\Delta S_w = X_d/t_d \tag{4.6}$$

where $(\Delta f_w/\Delta S_w)$ is the ratio of the changes in f_w and S_w in the jump. Graphically, the jump is determined usually by a point of tangency to the fractional-flow curve.

Figure 4.1 illustrates an application of fractional-flow methods using the case of waterflooding. The two phases involved are water and oil. Point “I” represents the initial state of the reservoir, at the irreducible water saturation, 0.2, and point “J” represents the injection condition, i.e. 100 % water fractional flow. A Buckley-Leverett shock from “I” to “S” is constructed on the fractional-flow curve to eliminate the non-monotonicity of $d(f_w)/d(S_w)$ between “I” and “J”. Only saturations between point “S” and “J”, plus initial condition “I”, are present in the displacement (Figure 4.2). Saturations between “S” and “J” propagate at constant velocities on characteristics, which can be represented in the time-distance diagram as straight lines from the origin.

In the time-distance diagram (Figure 4.2), the shock has the same slope as the shock line on the fractional-flow curve (Figure 4.1). In Figure 4.2 this shock separates the region with the initial saturation of $S_w = 0.2$ and the spreading-wave region, which starts with $S_w = 0.6$ immediately behind shock and gradually increases S_w to 0.8 at $X_d = 0$. Each dotted line from the origin represents a specific saturation moving at a dimensionless velocity giving by Eq. 4.5.

4.2.2 Applying fractional-flow methods to SAG processes

The fractional-flow curve for foam is shifted far up and to the left from that for conventional gas-water flow, because foam greatly reduces the mobility of gas. Near the limiting capillary pressure and limiting water saturation S_w^* (Chapter 1), foam weakens abruptly over a narrow range of S_w, and the fractional-flow curve is nearly vertical, as in Figure 4.3(a). This figure also shows what happens when gas is injected into a slug of surfactant solution in a SAG foam process. Here the initial condition "I" is at $S_w = 1$ following injection of liquid, and the injection condition is $f_w = 0$. Nearly the entire fractional-flow curve lies within the shock, which forms between the point "I" and the point of tangency to the fractional-flow curve at extremely low f_w. The success of the process depends on how much the foam has weakened at the condition defined by this point of tangency. Thus the nature and success of the displacement depends on the nature of the fractional-flow curve at extremely low f_w.

Figure 4.3(b) shows and expanded view of the fractional-flow curves for gas-water two-phase displacements with and without foam based on data of Persoff *et al*. (1991). With an expanded f_w scale, Figure 4.3(b) shows two plausible fractional-flow curves extended beyond the lowest-f_w datum of Persoff *et al*. (1991) (point "S"). The "progressive collapse" model of Zhou and Rossen (1995) assumes foam weakens gradually for $S_w < S_w^*$. The "fixed-P_c^*" model extends the vertical fractional-flow curve beyond the available data to reach complete foam collapse, i.e. to meet the $f_w(S_w)$ curve without foam at S_w^*. Without foam, in a water-wet medium, the fractional-flow curve lies so low at these water saturations that it almost overlaps the horizontal axis of the diagram.

Injection of gas into a medium saturated with surfactant solution is represented on the fractional-flow diagram as illustrated in Figure 4.4 for the "progressive collapse" model of Zhou and Rossen (1995). The initial condition "I" (not show in this figure, with expanded scale) lies at $S_w = 1.0$. The injection condition "J" (also not show in the figure, with expanded scale) is at $f_w = 0$, with S_w at its irreducible value. The displacement front is represented by a shock front from point "I" to a point of tangency on the fractional-flow curve as shown in Figure 4.4.

Figure 4.5 shows the "time-distance" diagram for the "progressive collapse" model. The shock line on this figure has the same slope as the shock line on the fractional-flow curve (note the difference in scale). The region to the upper left of the shock line represents the initial condition with a total relative mobility of 558 $(\text{Pa s})^{-1}$. Behind the shock line is another constant-state region bounded by the shock line and the tangent to the fractional-flow curve at S_w^*, with a constant total relative mobility of 278 $(\text{Pa s})^{-1}$. The shock line represents a saturation discontinuity between the two constant-state regions. Following the tangent line is a spreading-wave region. Within this region, any dotted line from the origin represents a different saturation value propagating at a different velocity. Numbers in the ovals represent total relative mobility of the foam at that saturation.

From Figure 4.5, one see that a foam bank with low mobility (278 $(\text{Pa s})^{-1}$) exists and expands with time. A SAG process with foam behavior that obeys this "progressive collapse" model therefore would be successful (Shan and Rossen, 2002).

Figure 4.6 shows the same initial and injection condition for the "fixed-P_c^*" model. Following the shock front, there is again a constant-state region bounded by the shock and the tangent to the fractional-flow curve at S_w^*. This constant-state region has a uniform saturation, at S_w^*. However, mobility within this region is 38,300 (Pa s)$^{-1}$, due to complete foam collapse at the point of tangency. To the lower-right of this region is a spreading-wave region of extremely low velocity (not seen). There is no low-mobility zone at all in the displacement. Thus, this model predicts a failure of the SAG processes. Shan and Rossen (2002) show that numerical simulation of such a process ironically might predict success, due to numerical artifacts.

Both models represent plausible extrapolation of the data of Persoff *et al.* (1991) (i.e., foam behavior at very dry conditions), but very different displacements. Thus, the success of SAG processes depends on the $f_w(S_w)$ curve at very low f_w values. However, measurement in this range is difficult, for a number of reasons. First, as foam weakens, it may be slow to reach steady-state. The near-zero slope of the fractional-flow curve means near-zero saturation-wave velocities in the core, i.e. slow approach to a new steady-state. Second, expected changes in saturation are small, but with large implications for a SAG displacement. Therefore, experimental measurement of water saturation must be accurate and precise.

4.3 EXPERIMENTAL DESIGN

There are a number of coreflood studies in which gas is injected into cores pre-saturated with surfactant solution (Bernard *et al.*, 1980; Yang and

Reed, 1989; Chou, 1991; Prieditis and Paulett, 1992). Some of the results show that foam can be persist for many pore volumes of gas injection. An obvious way to conduct SAG experiments in the laboratory is simply to inject slugs of surfactant and gas alternately into the core. However, it is dangerous to scale laboratory coreflood results directly to field scale, for several reasons.

First, the width of the displacement shock front in a laboratory core flood could be significant. Relative to core length, the shock front can be wide due to slow foam generation and chemical and capillary dispersion. In particular, foam generation to reach steady-state can take several pore volumes on the core scale (Rossen, 1996), completely distorting behavior projected to the field scale. On the other hand, the width of this shock front on the field scale is likely to be negligible.

Second, within the first few centimeters or inches of the injection face, foam is generated (or altered if a foam generator is used upstream of the core) (Ettinger and Radke, 1992). This length can be a significant portion of the core. However, a few inches are negligible on the field scale.

Third, water transport in a laboratory coreflood is different from that in the field. In the laboratory, the capillary end-effect is unavoidable, and it delays or stops water transport out of the core. Since foam mobility is very sensitive to water saturation, this delay in water transport would tend to make foam appear to last longer than it should. Additionally, at very high gas volumetric flux late in an experiment, evaporation of water into injected gas could be significant.

This would tend to make foam dry out and break prematurely. Thus, direct scale up of laboratory results to field scale is inappropriate.

We use a different approach here: obtain steady-state data in the laboratory, and then use fractional-flow methods to predict displacement behavior on the field scale. Laboratory artifacts that accelerate or restrict water transport from the core are less important because we measure water saturation directly. For ultimate field application, a reservoir simulator would be fitted to these data. That step is outside the scope of this study.

To obtain the fractional-flow curve, fixed volumetric fluxes of liquid and gas are imposed in a series of steps, and the resulting S_w at steady state is measured at each step with an electronic balance. As noted above, the fractional-flow curve at extremely low f_w determines the SAG displacement pattern. Therefore, injection rates in the experiments are restricted to high gas fractions, i.e. low f_w. This restriction also helps to keep pressure drop within the allowed range for the apparatus.

In order to determine S_w from core weight, it is important to set the initial condition for each experiment as close to $S_w = 1$ as possible. The first time a core is used, it is fully saturated with brine, which is then replaced by surfactant solution. To reuse a core that has been used in previous foam experiments, gas was removed by injecting many pore volumes of surfactant solution at back-pressure alternating three times between 0 and 150 psi. In retrospect, it would have been more efficient to use brine in this step.

Experiments were conducted at room temperature and with 150 psi back-pressure.

Experiment I was conducted using Bio-terge AS-40 surfactant at a concentration of 0.1 wt%. In Experiment I, core “A” was used, which had a porosity of 0.21 and permeability of 0.29 Darcy. To obtain steady-state flow at six values of f_w, as shown in Table 4.1, fixed superficial velocities of liquid and gas were imposed. Liquid superficial velocity ranged from 0.303 ft/d to 0.0303 ft/d. Gas superficial velocity ranged from 5.45 ft/d to 112 ft/d at the local average pressure in section 2 of the core.

Experiment II was conducted using Shell NEODOL 91-8 surfactant at concentration of 0.075 wt%. Core “B” was used, which had a porosity of 0.23 and permeability of 0.3 Darcy. Flow conditions are shown in Table 4.2. Water fractional flow ranged from 0.218 to 0.0041. Liquid superficial velocity ranged from 31.20 to 5.20 ft/d and then was kept at 5.20 ft/d for another 4 steps with gas superficial velocity increasing up to 1,260 ft/d at the local average pressure of section 2.

4.4 EXPERIMENTAL RESULTS AND DISCUSSION

4.4.1 Experiment I

Experiment I tested six steady-state conditions from $f_w = 0.0527$ to 0.00027 as shown in Table 4.1. The steady-state pressure drop in the three sections and average water saturation are shown in Figures 4.7 - 4.12. In each case both the sectional pressure drops and saturation stabilized following a period of change induced by the change of injection rates.

As shown in Figures 4.7 - 4.12, the pressure drops in the three sections, dp1, dp2, and dp3, don't change much between several of the steady-states, especially pressure drop in sections 1 and 2. Pressure drop in section 2 is slightly larger than in section 1, but smaller than in section 3. The capillary end-effect may be responsible for the higher pressure drop in section 3; an inlet effect may be responsible for the slightly lower pressure in section 1. Pressure drop in section 2 is the most stable one, and, in principle, this measurement is least subject to the inlet and outlet effects. Pressure drop in section 2 is used in subsequent calculations. The higher pressure drop in section 3 may reflect only a slightly higher water saturation, given the extreme sensitivity of foam to S_w. There appears to be some drift in the measured water saturation for the two lowest-f_w data ($f_w = 0.00075$ and 0.00027; Figures 4.11 and 4.12). There is no apparent drift in pressure drops during this time. As noted in Chapter 3, there can be some drift in scale reading over long times. In each case there was a reasonably steady period of core weight before apparent drift set in. Therefore we took the value during this steady period as the core weight (*cf*. Table 4.1).

Fortunately, these two data are not crucial to the scale-up of the results using fractional-flow theory, described below.

It takes longer (hundreds of injected in Figures 11 and 12) to verify steady-state as S_w decreases. In part this is expected from the shape of fractional-flow curve (shown below). As S_w decreases, the slope $d(f_w)/d(S_w)$ decreases, which means slower propagation of saturation changes through the core.

Table 4.1 shows preset quantities, measured quantities and derived quantities at each steady-state condition. u_w and u_g are preset quantities (except for the effect of pressure on u_g), while dp2, dp3 and S_w are measured quantities. dp3 is listed because gas superficial velocities u_g were calculated based on pressure at middle of the core in section 2, which depends on dp3. On the other hand, dp1 is not involved in the calculation of the derived quantities. Liquid fractional flow f_w, liquid relative permeability k_{rw}, gas effective relative permeability with foam k_{rg}^f, apparent viscosity of foam μ_{app}, gas mobility-reduction factor R, and relative total mobility λ_{rt} are derived quantities. Derived quantities are defined and calculated as follows.

Liquid fractional flow was calculated directly from volumetric fluxes:

$$f_w = u_w/(u_w+u_g). \tag{4.7}$$

The foam fractional-flow function derived from the data is shown in Figure 4.13. More discussion on the fractional-flow curve and fractional-flow method is in the next section.

Liquid relative permeability was calculated from Darcy's law applied to the liquid phase:

$$k_{rw} = (u_w\mu_w)/(k\ \Delta p/L)\ , \tag{4.8}$$

where $\Delta p/L$ is the pressure gradient calculated from dp2 and the corresponding length of section 2, which is 10.16 cm (1/3 ft).

The $k_{rw}(S_w)$ curve derived from these data is plotted in Figure 4.14. A power-law function,

$$k_{rw} = 170\ S_w^{10.02} \tag{4.9}$$

fits the data reasonably well in this saturation range. Eq. 4.9 doesn't include an irreducible water saturation or fit behavior at large S_w. It is only intended to represent the data in the range of measured water saturations.

Foams greatly reduce gas mobility. There are at least three simplified ways to represent this. One can attribute the mobility reduction entirely to a reduction in gas effective relative permeability, k_{rg}^f,

$$k_{rg}^f = (u_g\mu_g)/(k\ \Delta p/L) \tag{4.10}$$

where μ_g is gas viscosity in the absence of foam, about 0.02 cp ($2\text{x}10^{-5}$ Pa s) (Perry and Chilton, 1973). In this low range of water saturation, with no foam, gas relative permeability should be roughly between 0.5 and 1.0 (Persoff *et al.*, 1991). With foam, gas effective relative permeability ranges from 0.001 to 0.03 over the range of the data (Figure 4.15(a)).

Another way to represent gas mobility reduction is as an increase in gas effective viscosity. If one assumes gas relative permeability takes its foam-free value $k_{rg}^o \approx 1$ and calculates gas apparent viscosity, μ_{app}, one finds

$$\mu_{app} = (\Delta p/L)\ (k/\ u_g)\ . \qquad (4.11)$$

Figure 4.15(b) shows apparent gas viscosity plotted against water saturation. Apparent viscosity decreases sharply at high S_w, and then declines more slowly with decreasing water saturation. The lowest value is still close to 0.6 cp at S_w = 0.279 and f_w = 0.00027, however, 30 times the viscosity of gas without foam, indicating foam persistence at low S_w.

A gas mobility-reduction factor R has been used in some foam simulation models (Rossen *et al.*, 1999; Cheng *et al.*, 2000, 2002); it is yet another parameter to characterize foam strength. It can be calculated as the ratio of mobilities of gas with and without foam at the same liquid saturation:

$$R = \lambda_{rg}{}^{o}(S_w)/\lambda_{rg}{}^{f}(S_w) = k\ k_{rg}{}^{o}(S_w)\ (\Delta p/L)\ /(u_g\ \mu_g\ ) \qquad (4.12)$$

where $\lambda_{rg}{}^{o}(S_w)$ is the relative mobility of gas without foam; $\lambda_{rg}{}^{f}\ (S_w)$ is the relative mobility of gas with foam, defined as

$$\lambda_{rg}{}^{o} = k_{rg}{}^{o}/\mu_g$$

$$\lambda_{rg}{}^{f} = u_g/(k\Delta p/L)\ . \qquad (4.13)$$

$k_{rg}{}^{o}$ and μ_g are gas relative permeability and viscosity, both without foam. R represents the degree of gas mobility reduction by foam at the same water saturation. It differs from the “resistance factor” sometimes used in foam studies, which is a comparison of total mobility made at the same value of f_w. In this experiment (Table 4.1), R changes from 2370 to 101 as S_w declines from 0.345 to 0.279, indicating weaker foam as f_w decreases.

Total relative mobility is the sum of gas relative mobility and liquid relative mobility,

$$\lambda_{rt} = (u_g+u_w)/(k\Delta p/L) . \tag{4.14}$$

Total relative mobility is the ratio of total superficial velocity to permeability times pressure gradient. Total relative mobility changes from 74 to 1650 $(Pa\ s)^{-1}$, as S_w declines from 0.345 to 0.279 (Table 4.1).

The fractional-flow curve, the main objective of these experiments, is shown in Figure 4.13(a); each of the points on the graph corresponds to a steady-state condition described above. The shape of the fractional-flow curve suggests a gradual collapse of foam as S_w decreases, not an abrupt, complete collapse at a single value of S_w^*.

In Figure 4.13(b), the foam fractional-flow curve is plotted with the foam-free fractional-flow curve in a log scale. The foam-free fractional-flow function $f_w(S_w)$ is calculated based on $k_{rw}(S_w)$ (Figure 4.14) and k_{rg}^o, which is assumed to be 1.0. The value of f_w differs between the two curves by from 1 ½ to 3 ½ orders of magnitude. Even had a smaller k_{rg}^o been used in $f_w^o(S_w)$, the difference would still be significant. In conclusion, the foam fractional-flow curve is still well above the foam-free curve at low f_w. Although we have not extended the steady state to $f_w = 0$, the data are sufficient to extrapolate a hypothetical SAG displacement to the field scale.

4.4.2 Applying fractional-flow methods to data

With fractional-flow data, one can predict the displacement pattern for gas injection into surfactant-saturated zone in a SAG process. An exponential fit to foam data (Figure 4.13) gives

$$f_w = 4.0x10^9\ S_w^{24}; \tag{4.15}$$

then the slope on the fractional-flow curve, $d(f_w)/d(S_w)$, can be computed at any S_w value. The initial condition of the displacement, at point “I”, is $S_w = 1.0$, $f_w = 1.0$. The injection condition is at “J”, at $f_w = 0$, with S_w at its irreducible saturation. This saturation is unknown, except that it is less than 0.279.

Construction of the shock from point “I” to the point of tangency on the fractional-flow curve at point “S” is shown in Figure 4.16. The slope of the shock line, equal to the slope of the tangent line at point “S”, is about 1.5. As shown in Figure 4.17, saturation changes from the initial condition $S_w = 1.0$, with total relative mobility of 1000 $(Pa\ s)^{-1}$, discontinuously to $S_w = 0.340$ ($S_w = 0.340$ is not an experimental datum, it is the water saturation at the point of tangency calculated from Eq. 4.15). Behind this shock, water saturation decreases gradually, with characteristic velocities equal to the slope of fractional-flow curve at that saturation. For example, at $S_w = 0.322$, the slope is 0.46, with total relative mobility of 326 $(Pa\ s)^{-1}$; at $S_w = 0.293$, the slope is 0.017, with total relative mobility of 1060 $(Pa\ s)^{-1}$.

Compared to the prediction of the “progressive collapse” model illustrated in Figure 4.5, the prediction of SAG displacement from data of Experiment I doesn’t have a constant-state region leading the foam bank. In Figure 4.5 the constant-state region is a result of the abrupt change in slope $(d(f_w)/d(S_w))$ of the fractional-flow curve. However, a low-mobility foam bank is present throughout the displacement in Figure 4.17, indicating a successful SAG process.

At $S_w = 0.279$, the slope is 0.017, which means it takes nearly 60 PV injection for this saturation to reach the end of core. Although such low saturations may never propagate far into a reservoir, they do apply near the well-bore, where they have a large impact on injectivity (Shi and Rossen, 1998; Shan and Rossen, 2002).

4.4.3 Experiment II

Experiment II was conducted with core "B", which had been used prior to this experiment. The difference between a reused core and a new core is that a new core is vacuum-saturated with brine, thus providing a more reliable reference for water saturation. With a reused core, a little gas might still remain in the core after flushing the core with surfactant and cycling in back-pressure three times.

Eight sets of steady-state data at flow conditions specified in Table 4.2 are shown in Figure 4.18–4.26. For each flow condition, pressure drop in the three core sections and average saturation are plotted against pore volume injected. From these plots, it can be seen that steady states have been reached for most of the steps. The first step (Figure 4.18) and the last step (Figure 4.26) appears not yet a steady state, with average water saturation still change even after more than 100 PV for the latter case. Fortunately, these two data are not crucial to the analysis that follows. We continue to use the pressure-drop data from section 2 in our calculations, as the data in principle least affected by entrance and end-effect. In this experiment, however, the pressure drop in section 2 was sometimes lower than that in section 1.

The water relative-permeability data $k_{rw}(S_w)$ are plotted in Figure 4.27. The data fit a power-law function,

$$k_{rw} = 20.5\, S_w^{7.59} \qquad (4.16)$$

reasonably well. Eqs. 4.8 (Figure 4.14) and 4.16 (Figure 4.27) from Experiment I and II are within about a factor of two of each other in the range of S_w in which they overlap. The discrepancy may be partially due to differences between the cores.

Figure 4.28(a) shows the fractional-flow data. In Figure 4.28(b), the fractional-flow curve is compared to the foam-free fractional-flow curve on a log scale, using the $k_{rw}(S_w)$ function derived from data and assuming $k_{rg}^o = 1$ and $\mu_g = 0.02$ cp. The values of f_w from the two curves differ by at least two orders of magnitude. Even if a smaller value of k_{rg}^o were used, the difference would still be significant. Even after foam weakens, the foam fractional-flow curve still lies well above the foam-free curve.

The "fixed-P_c^*" model assumes that strong foam exists at a unique capillary pressure P_c^* and an unique water saturation S_w^* (Rossen and Zhou, 1995), as described in Chapter I. In this experiment, as in Experiment I, foam doesn't collapse at a single S_w^*; rather it weakens gradually over a range of saturations.

The foam data in Figure 4.28(a) do not lie on a single curve. In fact, saturation *increases* as f_w decreases from 0.0369 to 0.0189. In this transition, R drops from 2150 to 865, λ_{rt} increases from 80 to 196 (Pa s)$^{-1}$, and k_{rw} increases (Table 4.2), consistent with the rise in S_w.

A repeat experiment was conducted in attempt to test and reproduce this behavior using the same core and same surfactant; only three values of f_w were checked (Table 4.2). Again, the same behavior was observed, as shown in Figure 4.29. The shift in average water saturation during the repeat is probably caused in part by failure to expel all the gas from the core at the start of this experiment, re-using core “B”. Gas in the core at the start of the experiment would mean a smaller decline in core weight during foam injection and higher apparent S_w. The shift in S_w between curves is nearly consistent at 0.019 ± 0.003. In any case, the shape of the fractional-flow curve, and particularly the rise in S_w at f_w = 0.037, is confirmed by the repeat experiment.

The saturation rise in this experiment was only 0.004, from 0.312 to 0.316, and the corresponding weight change was only about 0.6 gram. One may suspect that 0.6 gram could be artifact of the experiment. One possible cause of such an artifact is the dead volume in the apparatus. The change in water fractional flow is from 0.0369 to 0.0189; the difference of f_w is 0.018. Thus, any measurement error from dead volume should be less than 0.018 x 2 cc ˜ 0.036 grams, since 2 cc is the estimated dead volume in flow lines, distributing grooves, and fittings as discussed in Chapter 3. Thus the possible error from the dead volume is much smaller than 0.6 g. Moreover, the decrease in f_w should make the dead volume weigh less, not more, as f_w decreases.

Second, this change occurred within less than 1 PV injected (less than one hour, see Figure 4.29), so any drift of balance reading should be very small

(Chapter 3). Therefore, we conclude that the saturation change is real, the result of foam breakage and subsequent imbibition into the core.

Similar behavior was reported by Kibodeaux and Rossen (1997), and also by Wassmuth *et al*. (2001). In Kibodeaux and Rossen's (1997) experiments (Figure 4.30), the increase in water saturation was almost 0.02 (from 0.34 to 0.36) as f_w decreased from 0.02 to 0.004. Foam was much weaker after the transition in their case. Total relative mobility rose from 88.0 to 1620 (Pa s)$^{-1}$. The transition occurred at about the same value of f_w in our experiment as in Kibodeaux and Rossen, however.

Kibodeaux and Rossen (1997) suggest a hypothesis to explain their data. There are more than one foam steady-state possible at the same value of S_w, with a separate fractional-flow curve for each state. At some point upon reducing f_w, the strong-foam state is no longer stable and foam jumps to a weaker steady-state, as illustrated in Figure 4.31. Kam and Rossen (2002) present a mathematical model for this behavior, where at sufficiently low f_w a strong foam reverts to a coarse foam. In the context of the model, the multiple steady states reflect a nonlinear dependence of foam generation on pressure gradient (Rossen and Gauglitz, 1990; Gauglitz *et al*., 2002; Kam and Rossen, 2002). Our data do not fit this model quantitatively; in the model the "coarse foam" reduces gas mobility only a little, and there is little further weakening of foam upon further decreases in f_w. There is at least qualitative fit to the trend to the model and to the data of Kibodeaux and Rossen (1997), however.

After the transition in the fractional-flow curve, water saturation again decreases as f_w decreases (Figure 4.28(a)). For this particular experiment, we stopped at $f_w = 0.0041$, with R equal to 283. This range is sufficient to determine the shock front in a SAG process.

4.4.4 Applying fractional-flow method to data

Figure 4.32 shows shock construction on the fractional-flow curve obtained in Experiment II. A hypothetical field-scale 1D displacement can be predicted from the data. A shock line from initial condition "I" bypasses the upper portion of the fractional-flow curve. Therefore, data with f_w greater than the transition to weaker foam is irrelevant to a field-scale displacement. We have only four data points on the lower portion of the $f_w(S_w)$ curve. Due to limited data, only a rough prediction is attempted here, in the manner of Kibodeaux and Rossen (1997). Figure 4.32 shows a shock tangent to the lower portion of the fractional-flow curve at about $S_w \approx 0.314$ with total mobility equal to 404 $(\text{Pa s})^{-1}$ (Figure 4.33). In the spreading-wave region, water saturation decreases gradually, and mobility rises, as one moves toward the injection point. But mobility behind the shock is still lower than that of the water bank ahead of it.

4.5 DISCUSSION

4.5.1 Effect of injection rates on a fractional-flow curve

As mentioned in the previous section, fractional-flow theory makes several simplifying assumptions, including the assumption of Newtonian fluid properties, i.e., no dependence of fluid properties on total volumetric flux.

Foams are non-Newtonian in many cases (Alvarez *et al.*, 2001) in that behavior and mobilities at fixed f_w depend on total volumetric flux. Fractional-flow methods are still rigorously valid for scale-up of foam processes in the following restricted sense. In a 1D rectilinear flow, if gas is incompressible and volumetric injection rate constant, then total volumetric flux is uniform throughout the medium at all times in the displacement. Therefore, if the fractional-flow curve is measured at this same total volumetric flux, that curve governs the entire displacement. Therefore, one can scale-up laboratory data at least to a hypothetical field-scale rectilinear displacement with no loss of rigor, as long as the fractional-flow curve is measured at a single total volumetric injection rate, and gas-compressibility effects are negligible on the field scale.

Tables 4.1 and 4.2 show that our fractional-flow curves include data from a variety of total volumetric fluxes, with total volumetric flux increasing as f_w decreases. Thus the extrapolation to field scale using fractional-flow methods is not rigorous. If behavior were shear-thinning, as is often observed (Khatib *et al.*, 1988; Osterloh and Jante, 1992; Alvarez *et al.*, 2001; Mamun *et al.*, 2002), then the low-f_w data would have higher gas mobility at the higher volumetric fluxes of this experiment than if they had been taken at the same volumetric flux as the first datum at $f_w = 0.0527$. In other words, if one corrects for increasing volumetric flux in our experiment, one should adjust the gas mobilities *downwards* at low f_w. This would tend to increase f_w, or reduce S_w at the same value of f_w, for these data, as illustrated in Figure 4.34. A primary goal of this experiment is to determine whether foam collapses completely behind the shock front in a SAG process or not. Figure 4.34 makes clear that if there is a point of tangency at some value of f_w from the fractional-flow curve derived from data, the point of tangency would still occurs at a similar, or higher, value of f_w if the data had been taken at the same volumetric flux. Our fractional-flow data are sufficient to confirm that foam does not collapse behind the shock front in a SAG process.

It could be argued that the break in the fractional-flow curve shown in Figure 4.28 between f_w = 0.0369 and 0.0189 could be the result of shear-thinning rather than a distinct change in foam state. Stated differently, the sort of adjustment shown in Figure 4.34 could in principle make the break in the fractional-flow curve in Figure 4.28 disappear. Explaining the change in mobility between f_w = 0.0369 and 0.0189 in Table 4.2 purely as the results of shear-thinning rheology, however, would require a power-law exponent of (-0.32), outside the range of realistic values. Moreover, the change in total relative mobility between f_w = 0.0369 and 0.0189 in Table 4.2 is distinctly different from that seen elsewhere in the data. We believe the data reflect a change in foam state and a break in the foam fractional-flow curve between f_w = 0.0369 and 0.0189, as has been reported in other experimental (Kibodeaux and Rossen, 1997; Wassmuth *et al*., 2001) and theoretical studies (Kam and Rossen, 2002).

4.5.2 Construction of shock for multi-valued fractional-flow curve

Recently Rossen (Rossen, W. R., unpublished) has reconsidered the construction of the shock front with a multi-valued $f_w(S_w)$ function, illustrated with data from Experiment II, as shown in Figures 4.35. He concludes that in such a case the shock jumps over the portion of the curve where S_w increases and then decreases, as f_w decreases. The reason is that the traveling wave inside the shock must be monotonic in P_c (*cf*. Lake, 1989, for discussion of the traveling wave within the shock). As a result, the fractional-flow function jumps from the lowest value of S_w (0.312) on the strong foam portion of the $f_w(S_w)$ curve to the same value of S_w on the lower branch, as illustrated in Figure 3.35. In this case there is a shock to $S_w = 0.312$, with a total relative mobility of 422 (Pa s)$^{-1}$ (Table 4.2). Mobility is still lower behind the shock than in the water bank ahead, thus successful mobility control is still feasible with such a shock construction.

4.6 SUGGESTION FOR FUTURE WORK

Two simple improvements should be made in any future applications of this experimental technique. First, the core should be vacuum-saturated with brine at the start of each experiment. Given the difference between Experiment II and its repeat (Table 4.2 and Figure 4.29), it is not absolutely clear that water saturation was at 100% at the start of experiments in which the core was re-used. One should note, however, that a constant offset (error) in S_w would affect the scale-up of our data only in the slope of the shock, and that effect would be small; since the shock is drawn from $S_w = 1$, $f_w = 1$, a few percent difference in S_w in the range of $S_w = 0.3$ would make only a small difference to the slope. Other aspects of the fractional-flow solution for the displacement, including mobilities and characteristic velocities in the spreading wave, would be unaffected by altering all the S_w data by a fixed amount.

Second, all data should be taken at a single value of total superficial velocity. Then the scale-up to a hypothetical field-scale rectilinear displacement is rigorous, with certain simplifying assumptions. It would be even better to obtain several fractional-flow curves, each at a single total superficial velocity. In our experiments, we were restricted in the range of liquid injection rates possible with the pumps available. This made it impossible to conduct experiments over the full range of f_w values at one fixed total superficial velocity. Still, it would have been better to use a fixed superficial velocity for as wide a range of f_w as possible, rather than varying superficial velocity throughout the data as in Experiment I.

More work is needed for application of these results to the field. Issues include, but are not limited to, presence of oil, reservoir temperature, rock mineralogy, adsorption of surfactant, wettability, *in situ* foam generation and propagation, gravity override, operational and economic considerations.

The presence of crude oil can weaken or destroy foam (Rossen, 1996). Wettability is another factor that alters foam behavior, especially in the presence of oil. Foam displacements in the presence of oil can be modeled using fractional-flow theory (Zeilinger, 1996), but the procedure is much more complex with the additional components. Additionally, adsorption of surfactant has an impact on economics of SAG projects; adsorption also can be represented with fractional-flow theory (Zhou and Rossen, 1995).

Even where its assumptions do not hold in the field, fractional-flow theory provides insights into more-complex foam modeling (Rossen *et al.*, 1999). In the end, one has to balance the effects of simplifying assumptions in fractional-flow theory against the complexity and numerical artifacts (Shan and Rossen, 2002) in simulation of SAG processes. Fractional-flow methods do not stand alone, but complement complex simulation models for foam (Rossen *et al.*, 1999).

4.7 CONCLUSIONS

In the cases studied, foam don't break completely at a single value of S_w. Foams are sufficiently stable and persistent at extremely dry conditions for a successful SAG process, although foam is weakened significantly at low f_w. Using fractional-flow theory, displacement patterns predicted from experimental data suggest successful SAG foam processes, at the field scale under the experimental conditions. A fractional-flow curve obtained with Shell NEODOL 91-8 surfactant repeats Kibodeaux and Rossen's (1997) finding of a non-single-valued fractional-flow function.

Table 4.1 Measured and derived quantities for Experiment I

u_w (ft/d)	u_g (ft/d)	f_w	S_w	dp2 (psi)	dp3 (psi)	k_{rw}	k_{rg}^f	μ_{app} (cp)	R	λ_{rt} (Pa s)$^{-1}$
0.303	5.45	0.0527	0.345	13.7	20	0.00391	0.0014	14.24	2370	74.1
0.303	10.9	0.0269	0.345	15	18.9	0.00357	0.0026	7.78	1290	132
0.162	21.9	0.00730	0.322	12	19.5	0.00238	0.0065	3.09	516	326
0.162	54.1	0.00298	0.319	16	20	0.00178	0.0119	1.67	279	599
0.081	107	0.00075	0.293	18	20	0.00079	0.0211	0.95	157	1060
0.030	112	0.00027	0.279	12	16	0.00045	0.0330	0.61	101	1650

Bio-terge surfactant at 0.1 wt%; Core “A”

Table 4.2 Measured and derived quantities for Experiment II

u_w (ft/d)	u_g (ft/d)	f_w	S_w	dp2 (psi)	dp3 (psi)	k_{rw}	k_{rg}^f	μ_{app} (cp)	R	λ_{rt} $(\text{Pa s})^{-1}$
31.200	112	0.218	0.371	28.8	41.0	0.00715	0.0005	124	6240	33.8
20.800	125	0.142	0.357	18.1	24.4	0.00760	0.0010	69.9	3500	55.2
10.400	132	0.0725	0.339	11.7	18.7	0.00586	0.0016	42.8	2140	83.7
5.200	135	0.0369	0.312	12.0	16.7	0.00286	0.0016	42.9	2150	80.4
5.200	269	0.0189	0.316	9.6	13.5	0.00357	0.0039	17.3	865	196
5.200	526	0.0098	0.314	9.0	14.7	0.00381	0.0080	8.31	415	404
5.200	763	0.0068	0.312	12.5	18.1	0.00274	0.0084	7.95	397	422
5.200	1260	0.0041	0.310	14.7	18.7	0.00233	0.0117	5.67	283	589

Repeated steps

10.40	127	0.0729	0.361	9.5	18.7	0.00724	0.00184	36.1	1810	99.3
5.200	129	0.0372	0.328	8.4	16.3	0.00408	0.00211	31.5	1580	109
5.200	261	0.0188	0.331	7.5	15.0	0.00457	0.00478	13.9	697	243

Shell NEODOL 91-8 surfactant at 0.075 wt%; Core “B”

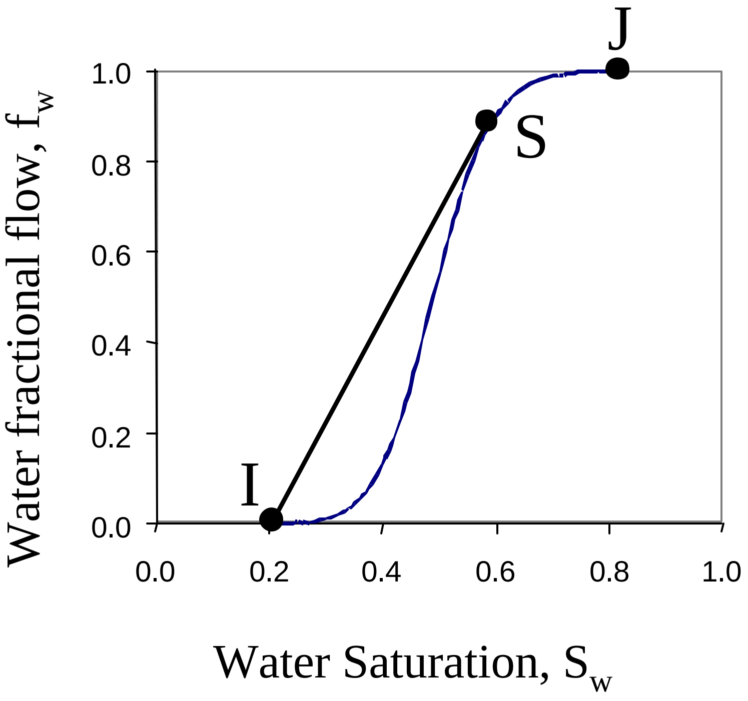

Figure 4.1 Fractional-flow curve for a waterflooding case at initial condition (I) of 80% oil, i.e. initially at irreducible water saturation.

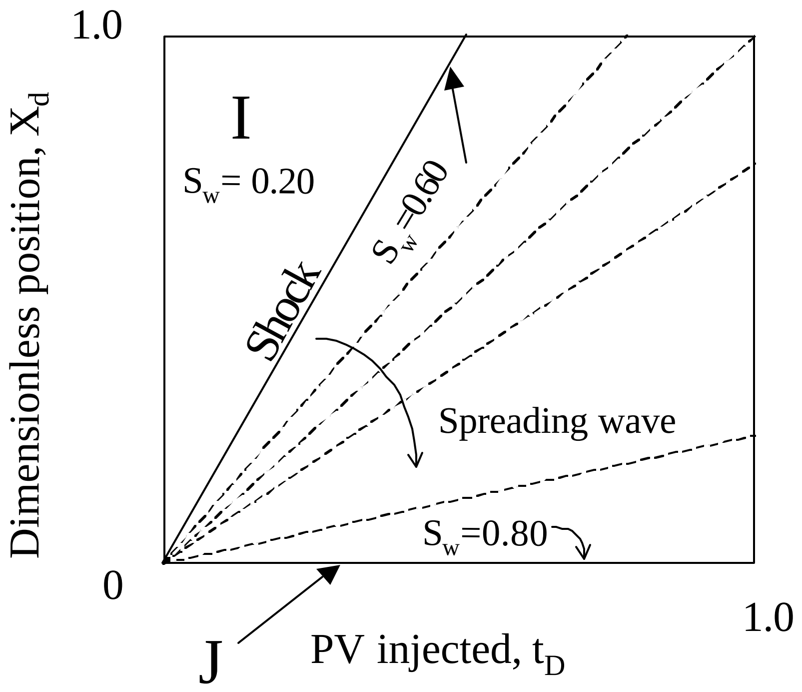

Figure 4.2 Time-distance diagram for the waterflooding case in Figure 4.1, with initial condition “I” ahead of, and spreading wave behind, shock. Solid line shows shock, and dotted lines characteristics within spreading wave.

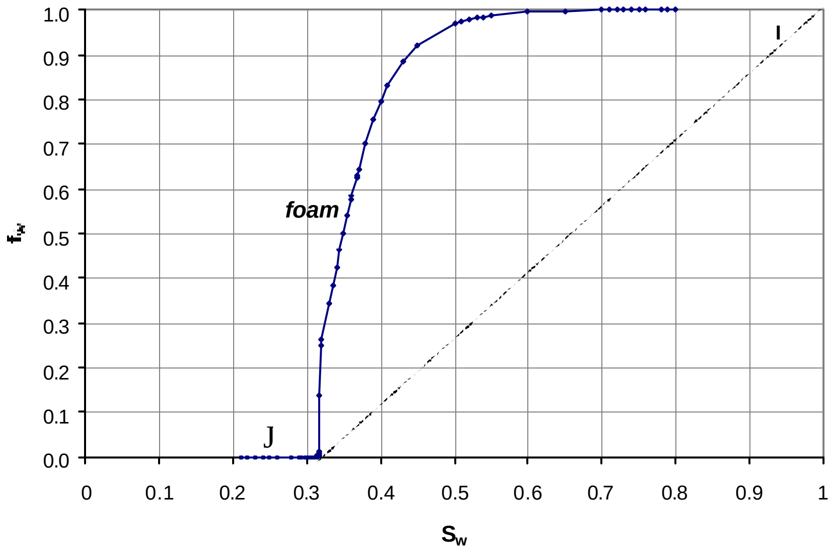

Figure 4.3(a) Schematic fractional-flow curve for foam showing shock front that forms during injection of gas (point "J", $f_w = 0$) into bank of surfactant solution (initial condition "I", $S_w = 1$) in a SAG process. Nature of foam behind shock depends on shape of fractional-flow curve at extremely low f_w, where shock front finds point of tangency to fractional-flow curve. (The model on which this figure is based is similar to, but differs in detail from, that used elsewhere in this chapter.) (From Shan, 1999.)

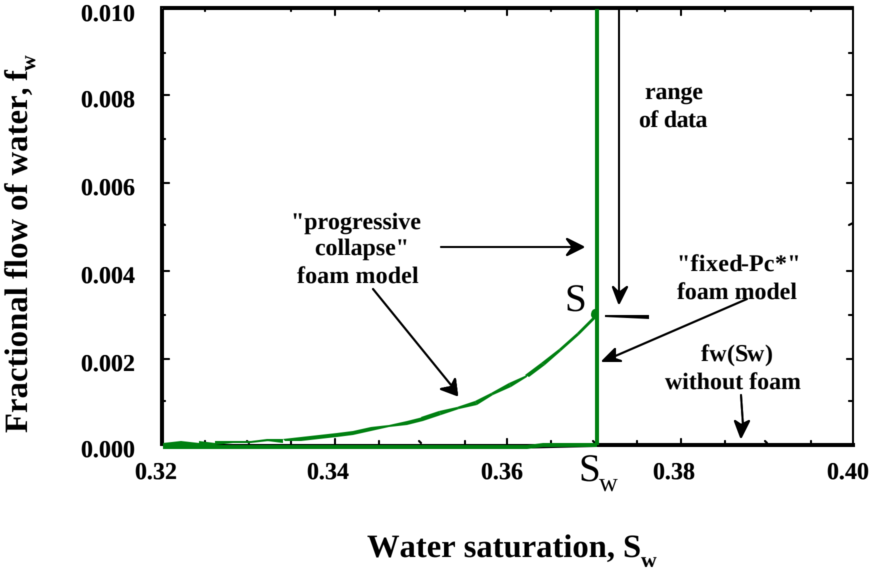

Figure 4.3(b) Expanded view of fractional-flow curves for “fixed-P_c^*”and “progressive collapse” foam models. After Zhou and ossen(1995).

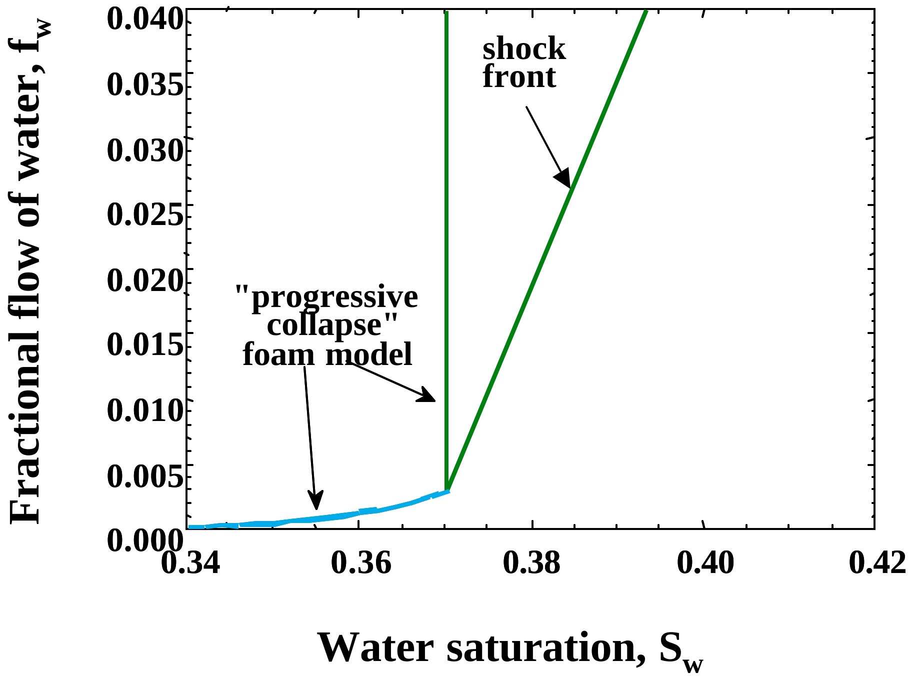

Figure 4.4 Application of fractional-flow method to the “progressive collapse” foam model; shock construction. After Zhou and Rossen (1995).

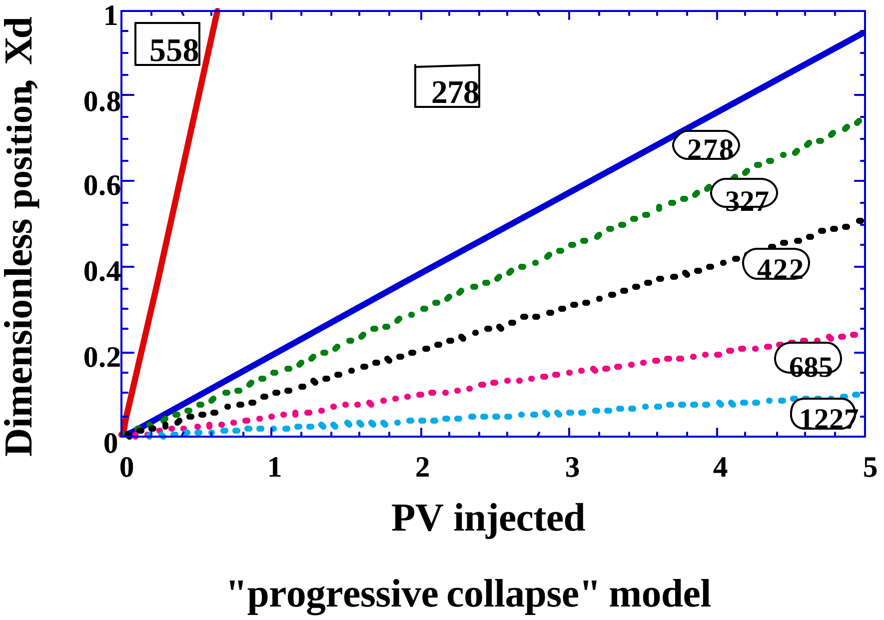

Figure 4.5 Application of fractional-flow method to the "progressive collapse" foam model; time-distance diagram. From Zhou and Rossen (1995). Total relative mobilities are given in (Pa s)$^{-1}$.

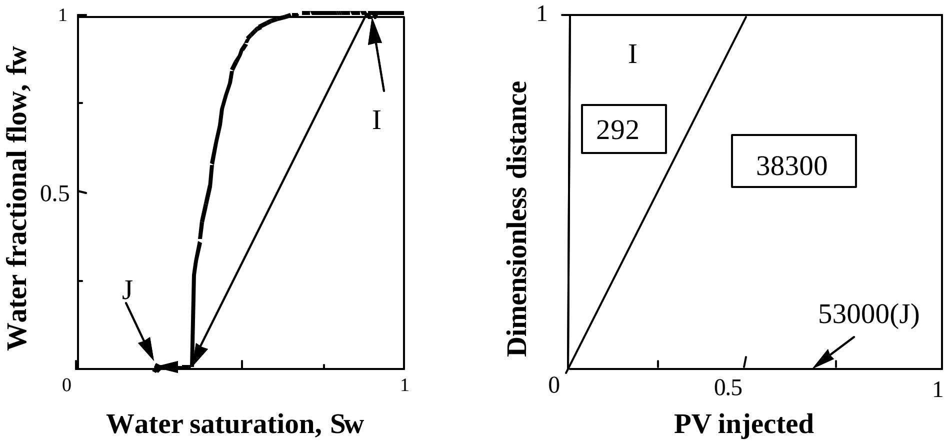

Figure 4.6 Application of fractional-flow method to the "fixed-P_c^*" model. From Zhou and Rossen (1995). Total relative mobilities are given in (Pa s)$^{-1}$.

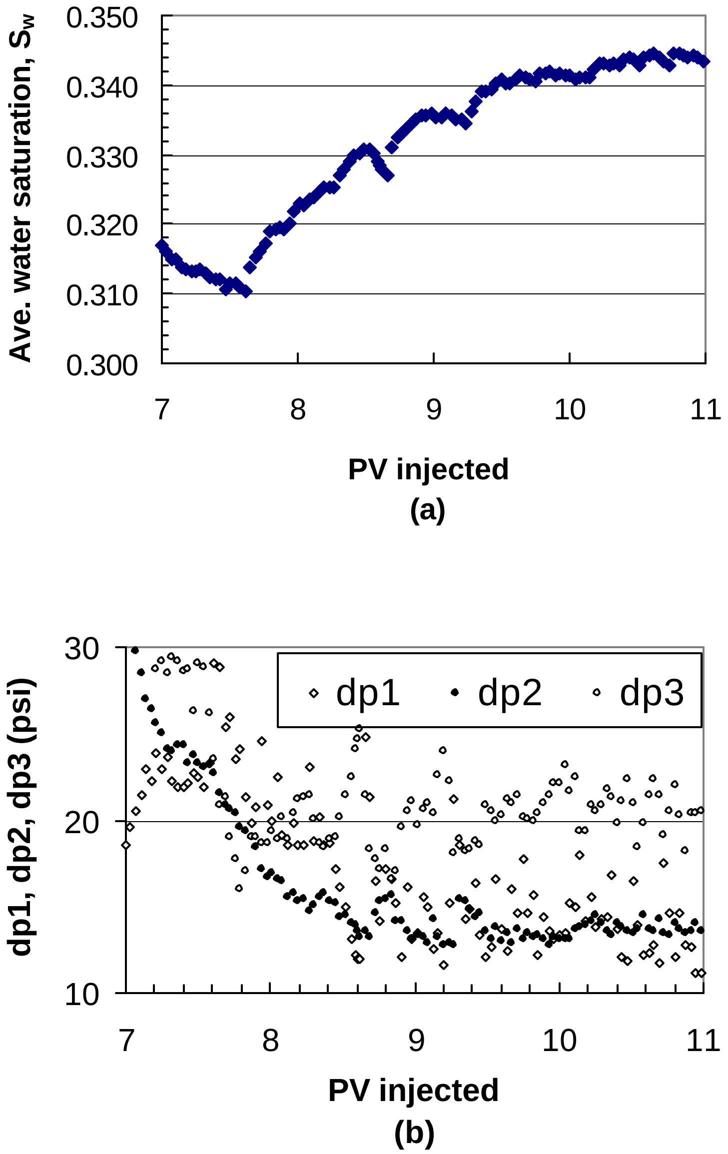

Figure 4.7 Results of Experiment I, with 0.1 wt% Bio-terge AS-40 surfactant injection at f_w = 0.0527 starts at 7.6 PV injected. (a) Average water saturation vs. pore volume injected. (b) Pressure drops in three sections of core vs. pore volume injected.

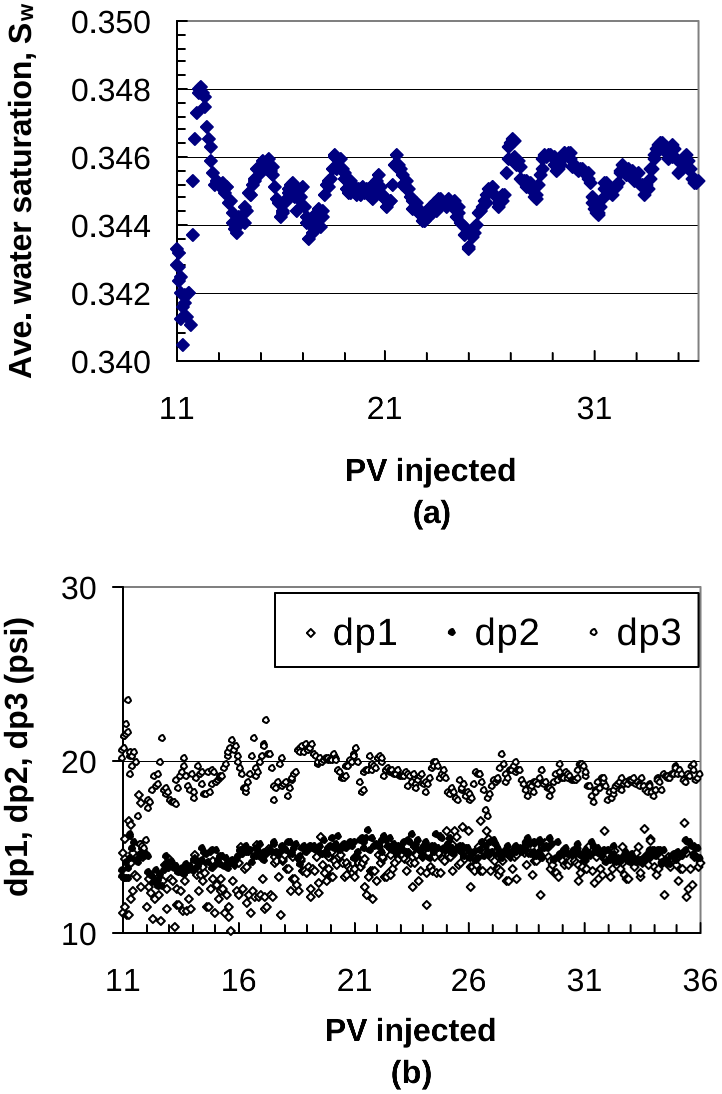

Figure 4.8 Results of Experiment I, with 0.1 wt% Bio-terge AS-40 surfactant injection at f_w = 0.0269 starts at 11 PV injected. (a) Average water saturation vs. pore volume injected. (b) Pressure drops in three sections of core vs. pore volume injected.

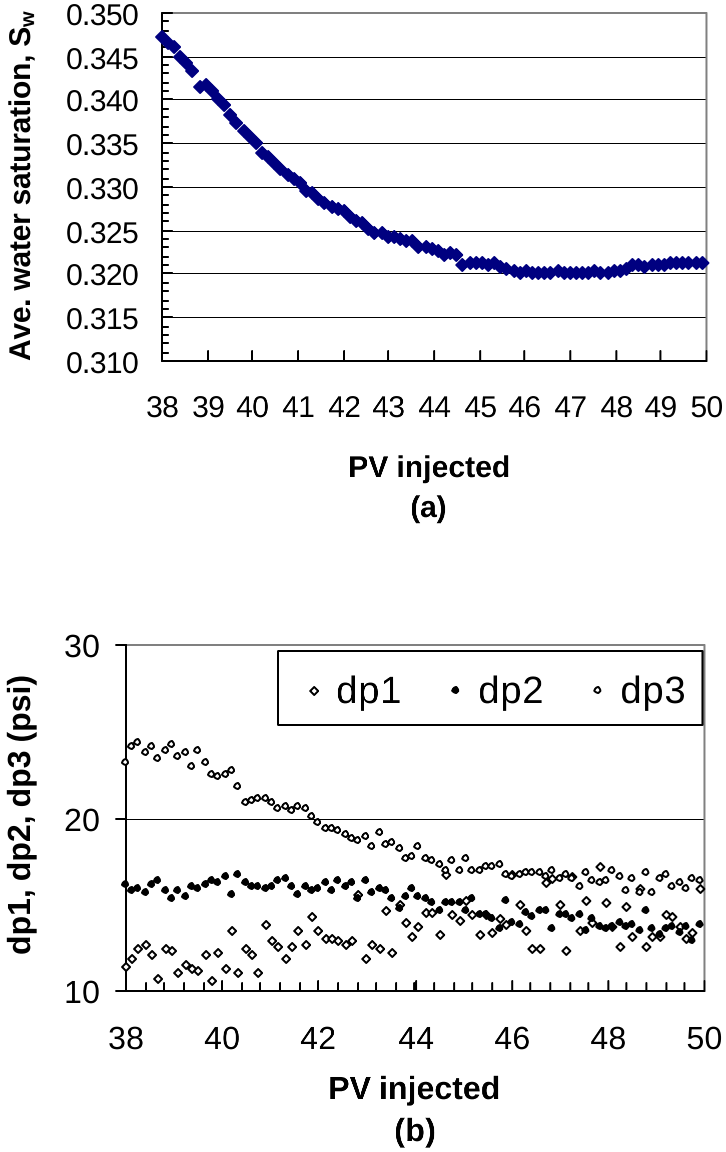

Figure 4.9 Results of Experiment I, with 0.1 wt% Bio-terge AS-40 surfactant injection at f_w = 0.00730 starts at 36 PV injected. (a) Average water saturation vs. pore volume injected. (b) Pressure drops in three sections of core vs. pore volume injected.

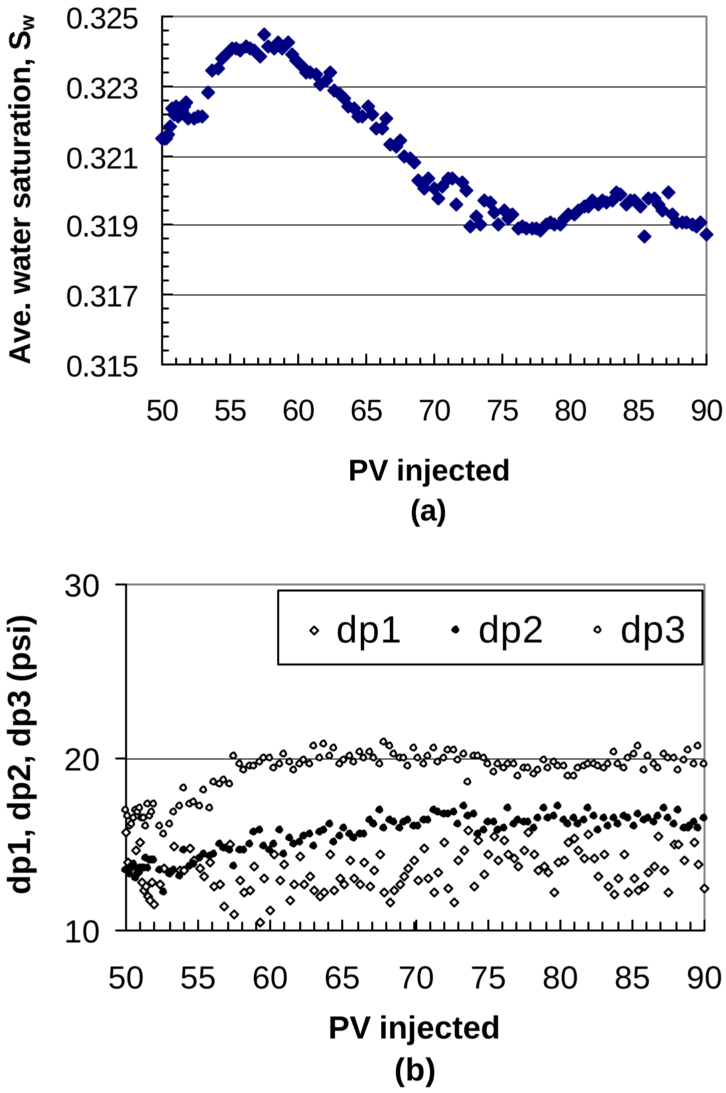

Figure 4.10 Results of Experiment I, with 0.1 wt% Bio-terge AS-40 surfactant injection at f_w = 0.00298 starts at 50 PV injected. (a) Average water saturation vs. pore volume injected. (b) Pressure drops in three sections of core vs. pore volume injected.

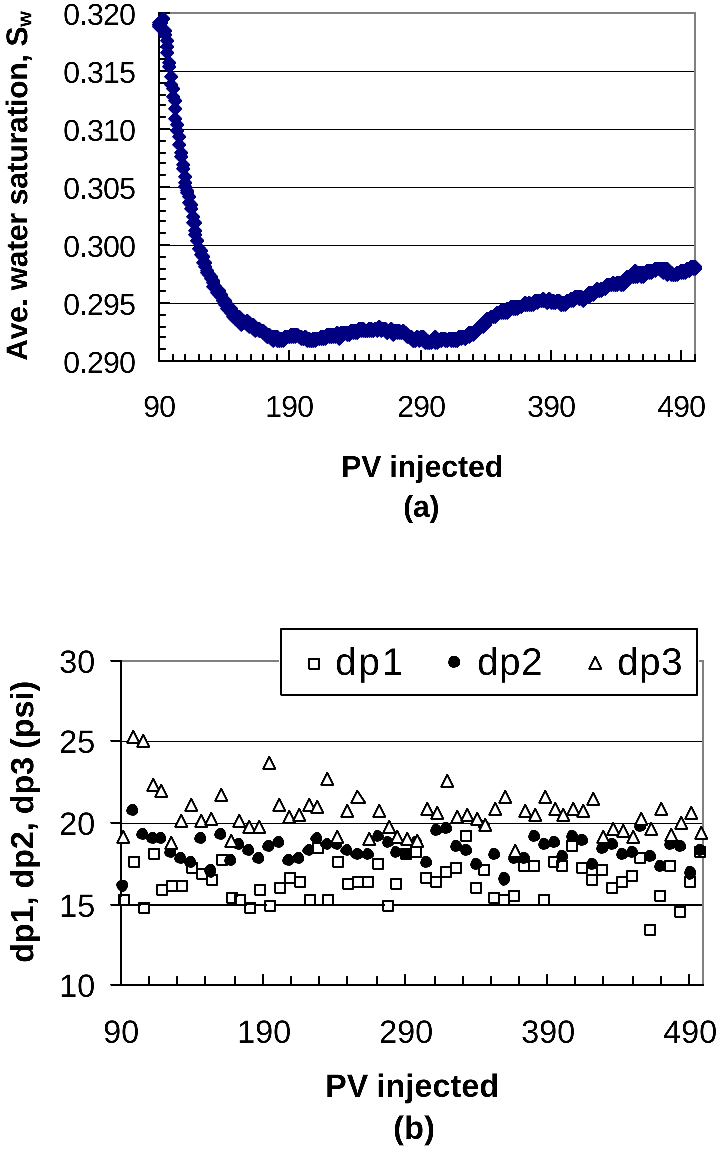

Figure 4.11 Results of Experiment I, with 0.1 wt% Bio-terge AS-40 surfactant injection at $f_w = 0.00075$ starts at 90 PV injected. (a) Average water saturation vs. pore volume injected. (b) Pressure drops in three sections of core vs. pore volume injected.

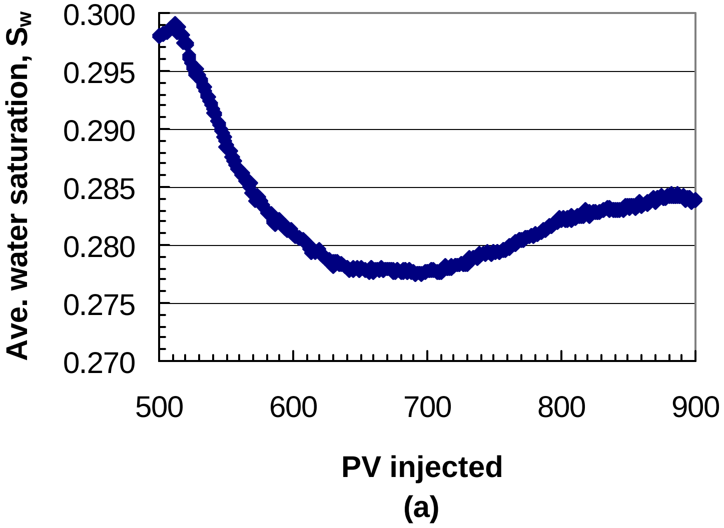

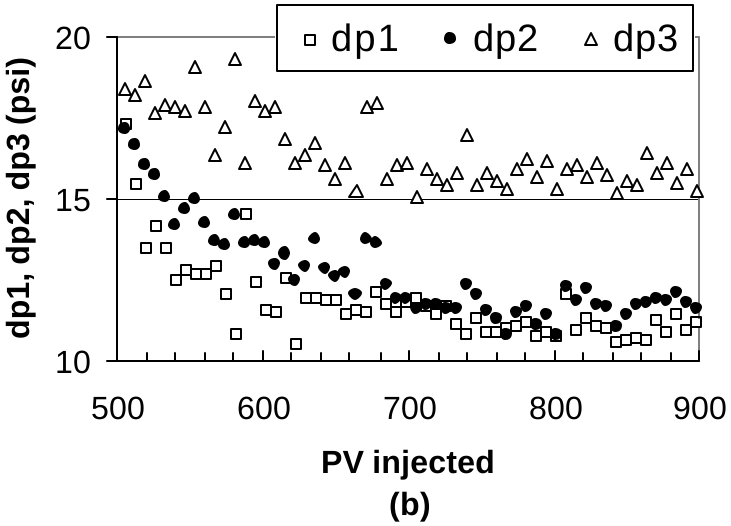

Figure 4.12 Results of Experiment I, with 0.1 wt% Bio-terge AS-40 surfactant injection at $f_w = 0.00027$ starts at 500 PV injected. (a) Average water saturation vs. pore volume injected. (b) Pressure drops in three sections of core vs. pore volume injected.

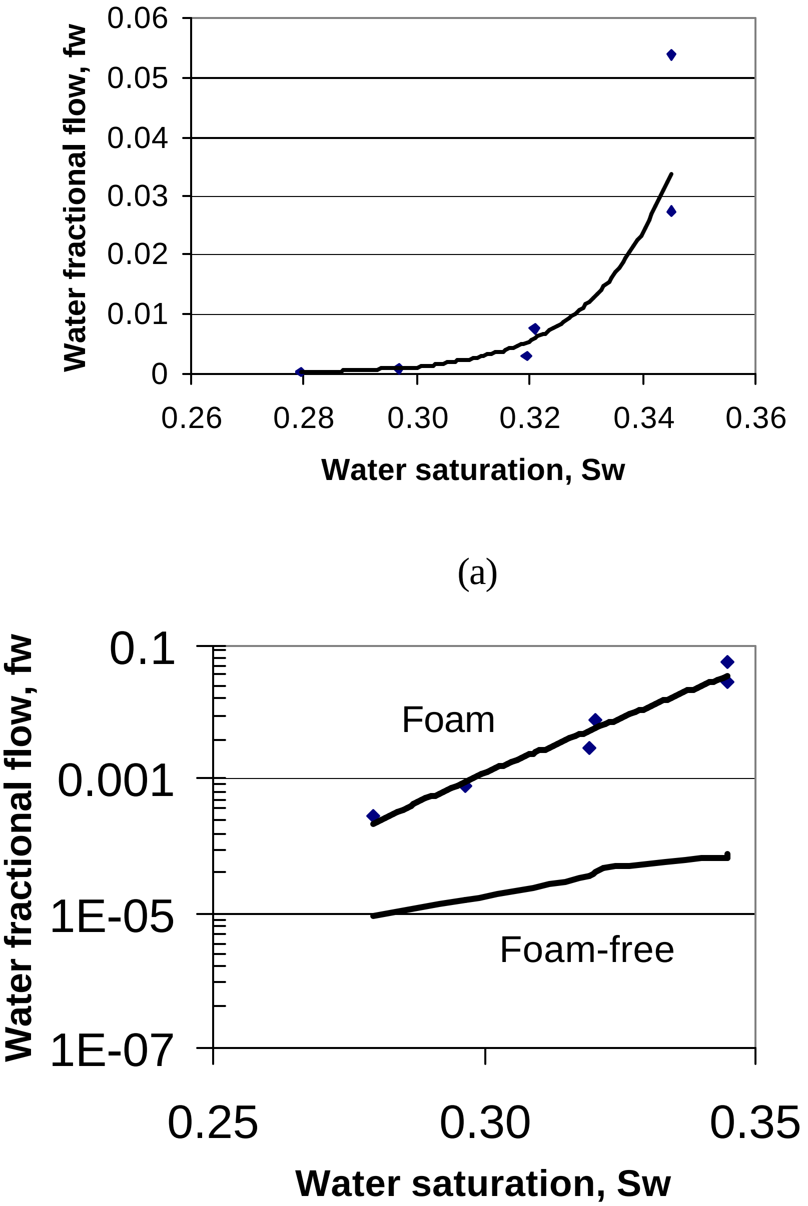

(a)

(b)

Figure 4.13 (a) Fractional-flow curve from Experiment I, 0.1 wt% Bio-terge AS-40 surfactant. (b) Comparison of foam fractional-flow curve and foam-free curve. The nearly linear trend on the log plot (b) suggests the power-law trend though the data plotted in (a) and given in Eq. 4.15.

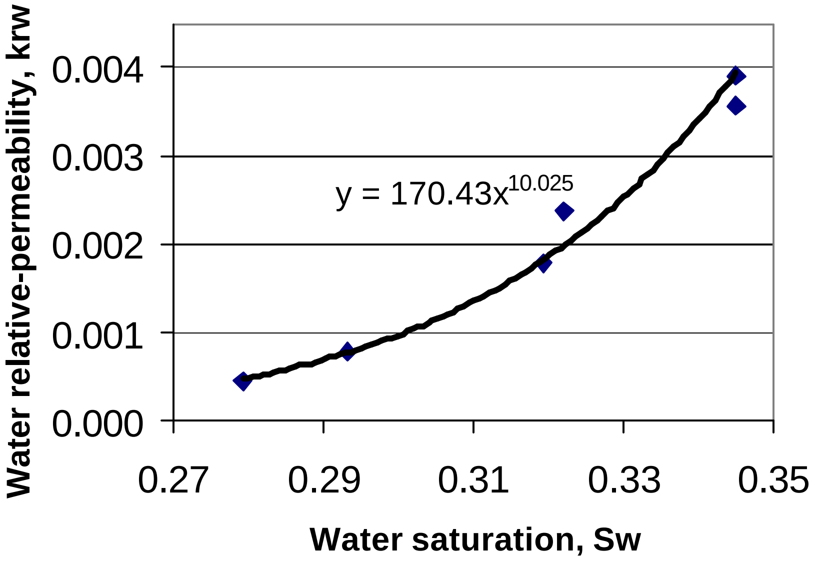

Figure 4.14 Water relative-permeability data and the fitted curve from Experiment I, with 0.1 wt% Bio-terge AS-40 surfactant.

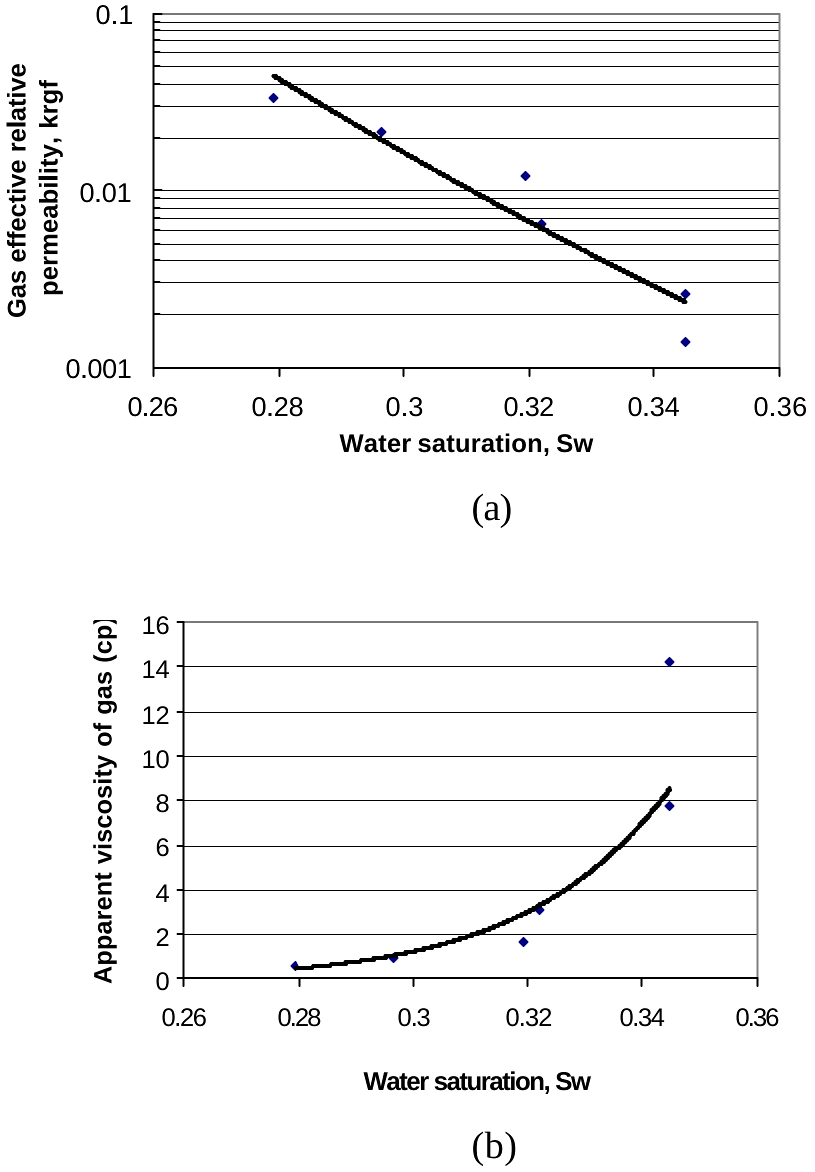

Figure 4.15 Results of Experiment I with 0.1 wt% Bio-terge AS-40 surfactant. (a) Gas effective relative permeability. (b) Apparent viscosity of gas as a function of water saturation.

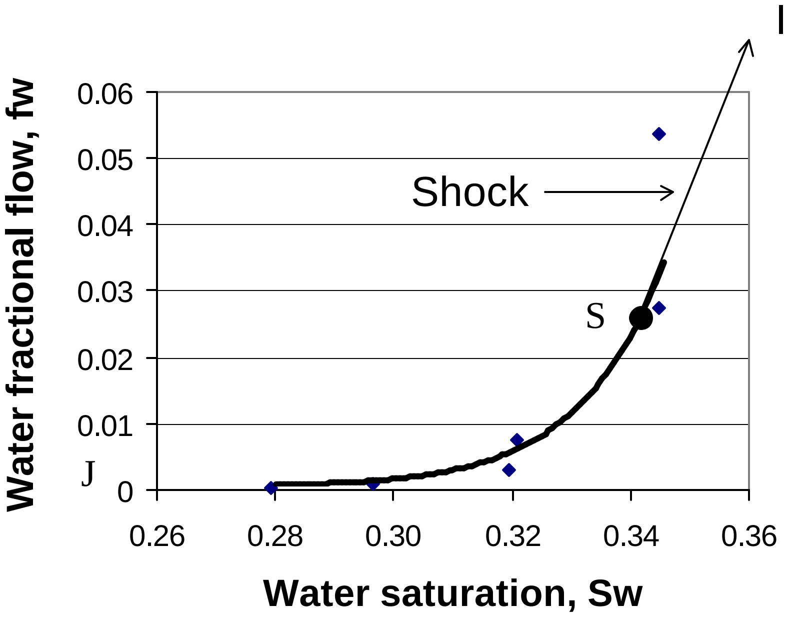

Figure 4.16 Fractional-flow method applied to results from Experiment I, with 0.1 wt% Bio-terge AS-40 surfactant.

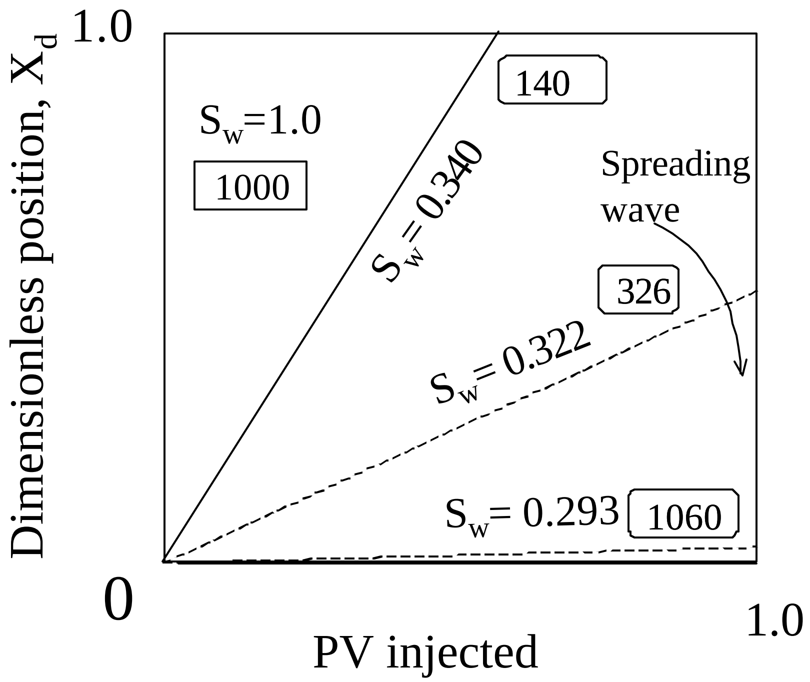

Figure 4.17 Time-distance diagram based on Experiment I, with 0.1 wt% Bioterge AS-40 surfactant. Numbers in boxes are total relative mobility in the unit of (Pa s)$^{-1}$.

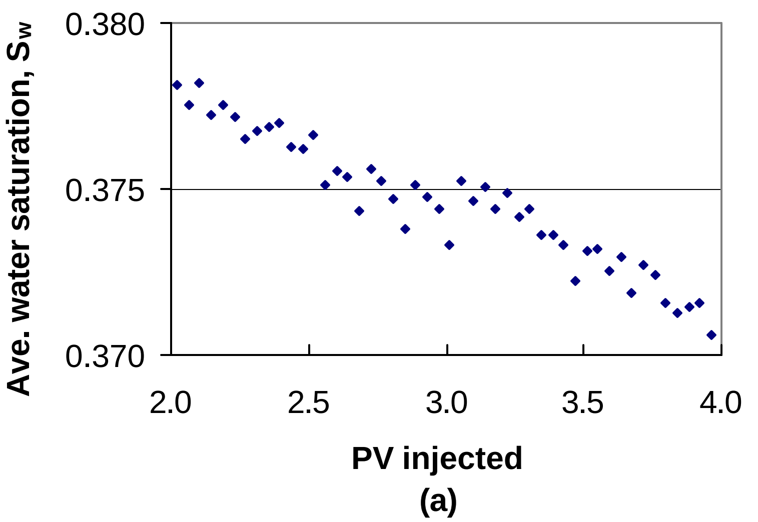

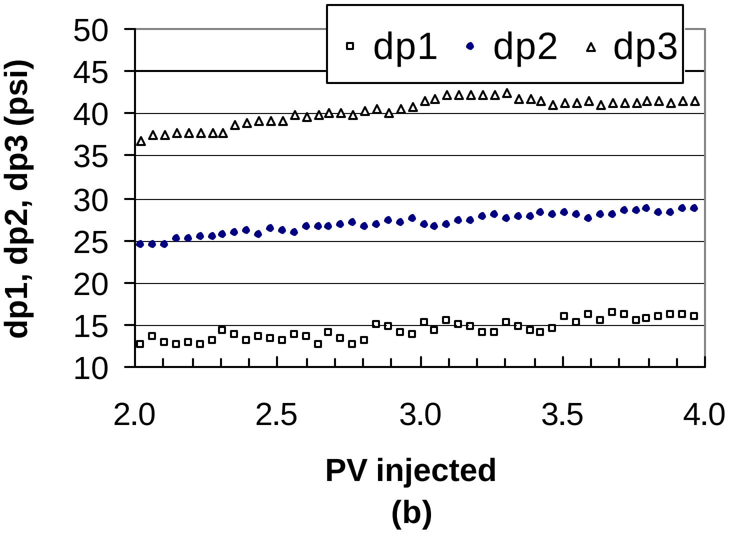

Figure 4.18 Results of Experiment II, with 0.075 wt% Shell NEODOL 91-8 surfactant solution injection at $f_w = 0.218$ starts at 2 PV injected. (a) Average water saturation vs. pore volume injected. (b) Pressure drop in three sections of the core vs. pore volume injected.

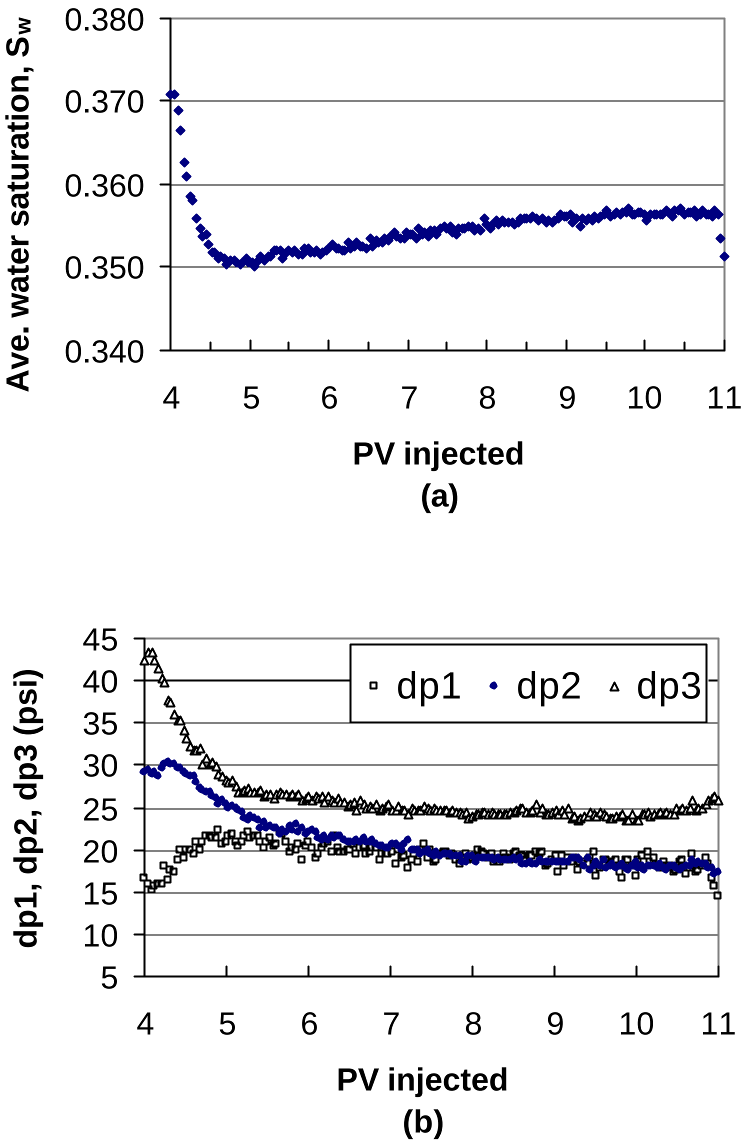

Figure 4.19 Results of Experiment II, with 0.075 wt% Shell NEODOL 91-8 surfactant solution injection at $f_w = 0.142$ starts at 4 PV injected. (a) Average water saturation vs. pore volume injected. (b) Pressure drop in three sections of the core vs. pore volume injected.

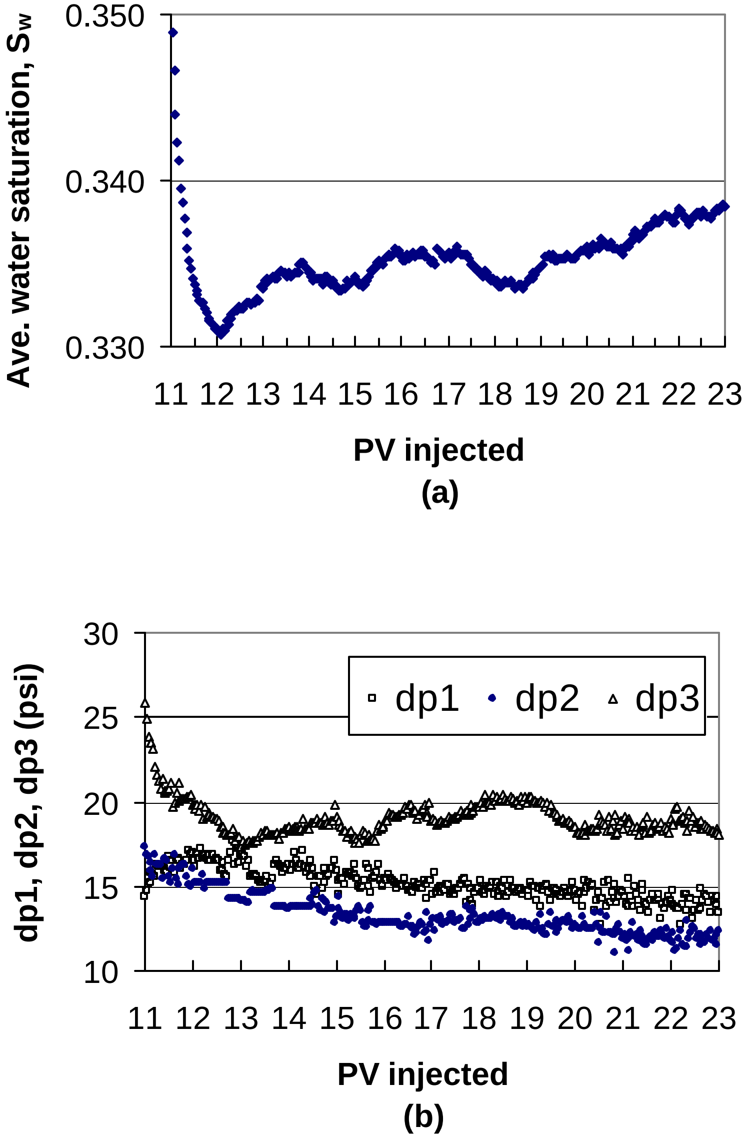

Figure 4.20 Results of Experiment II, with 0.075 wt% Shell NEODOL 91-8 surfactant solution injection at $f_w = 0.0725$ starts at 11 PV injected. (a) Average water saturation vs. pore volume injected. (b) Pressure drop in three sections of the core vs. pore volume injected.

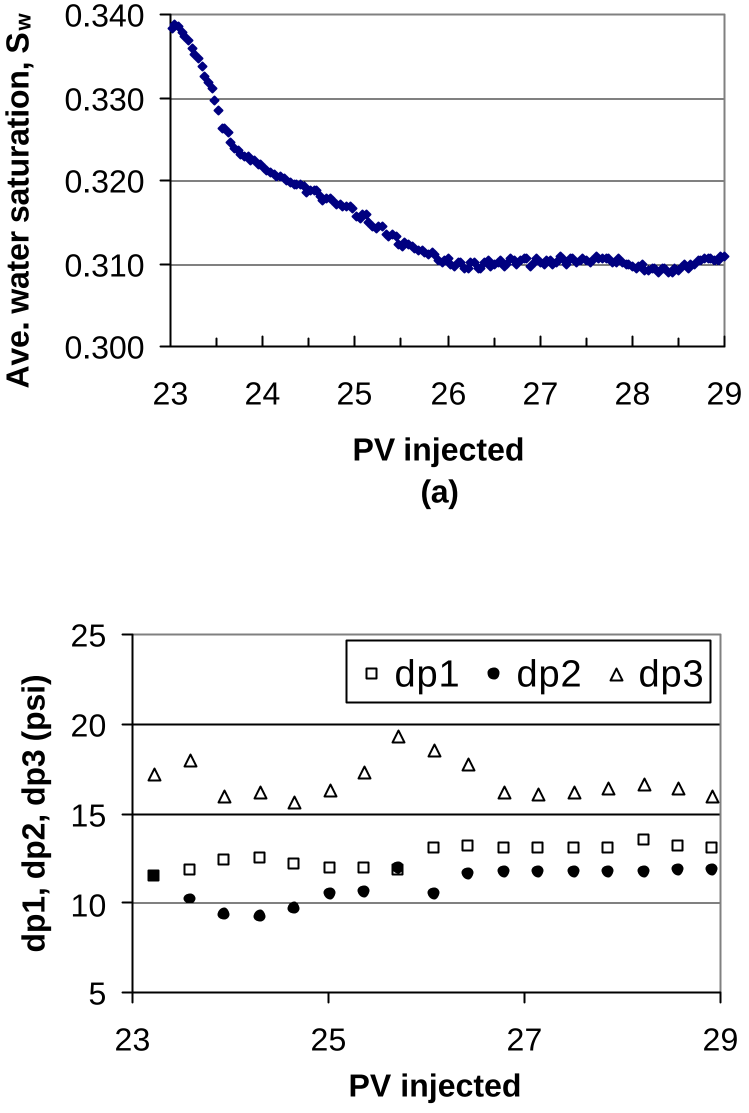

(a)

(b)

Figure 4.21 Results of Experiment II, with 0.075 wt% Shell NEODOL 91-8 surfactant solution injection at $f_w = 0.0369$ starts at 23 PV injected. (a) Average water saturation vs. pore volume injected. (b) Pressure drop in three sections of the core vs. pore volume injected.

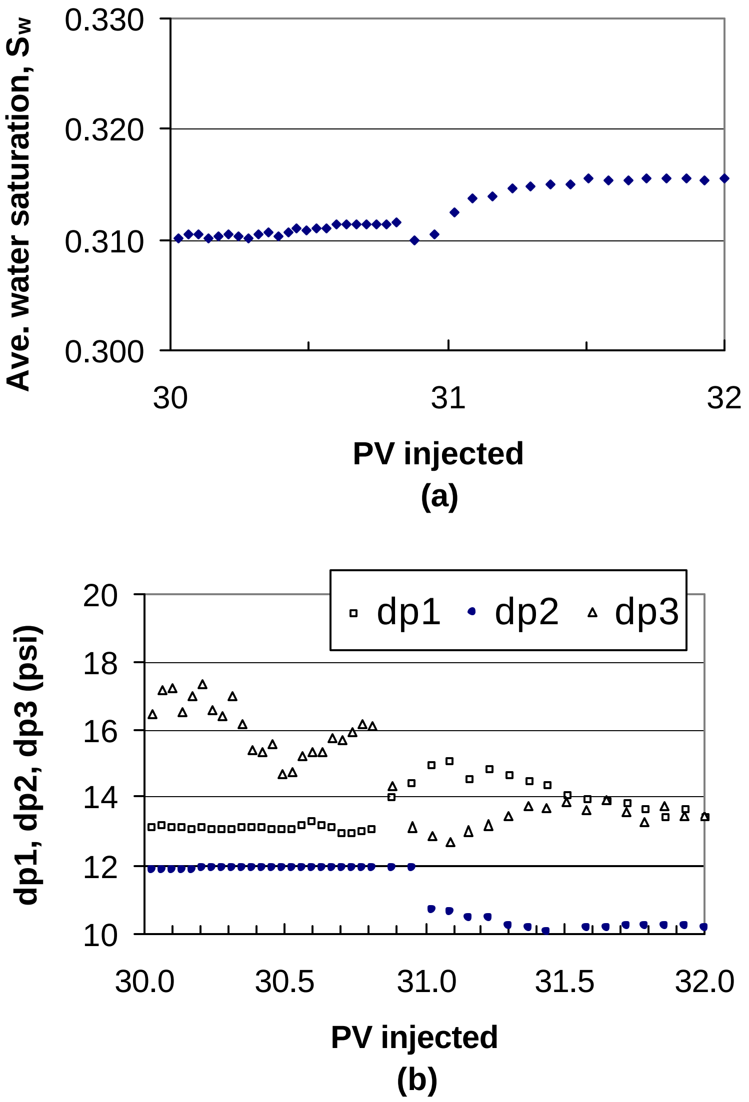

Figure 4.22 Results of Experiment II, with 0.075 wt% Shell NEODOL 91-8 surfactant solution injection from $f_w = 0.0369$ to 0.0189. (a) Average water saturation vs. pore volume injected. (b) Pressure drop in three sections of the core vs. pore volume injected.

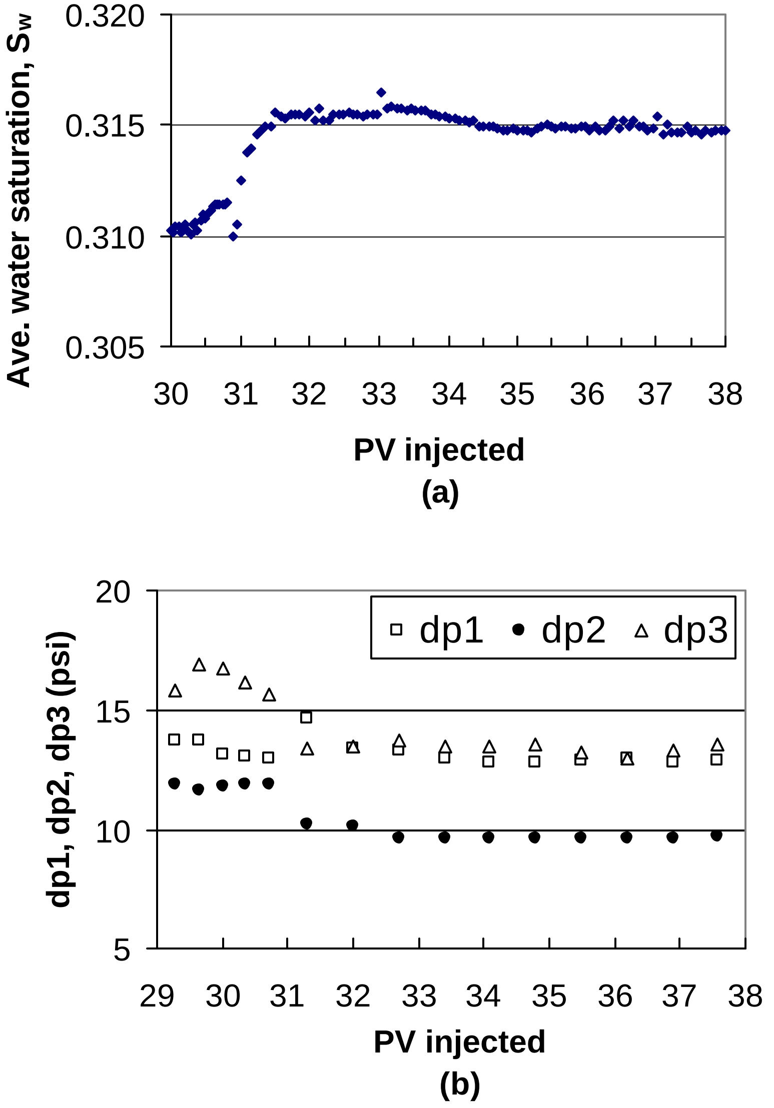

Figure 4.23 Results of Experiment II, with 0.075 wt% Shell NEODOL 91-8 surfactant solution injection at $f_w = 0.0189$ starts at 29 PV injected. (a) Average water saturation vs. pore volume injected. (b) Pressure drop in three sections of the core vs. pore volume injected.

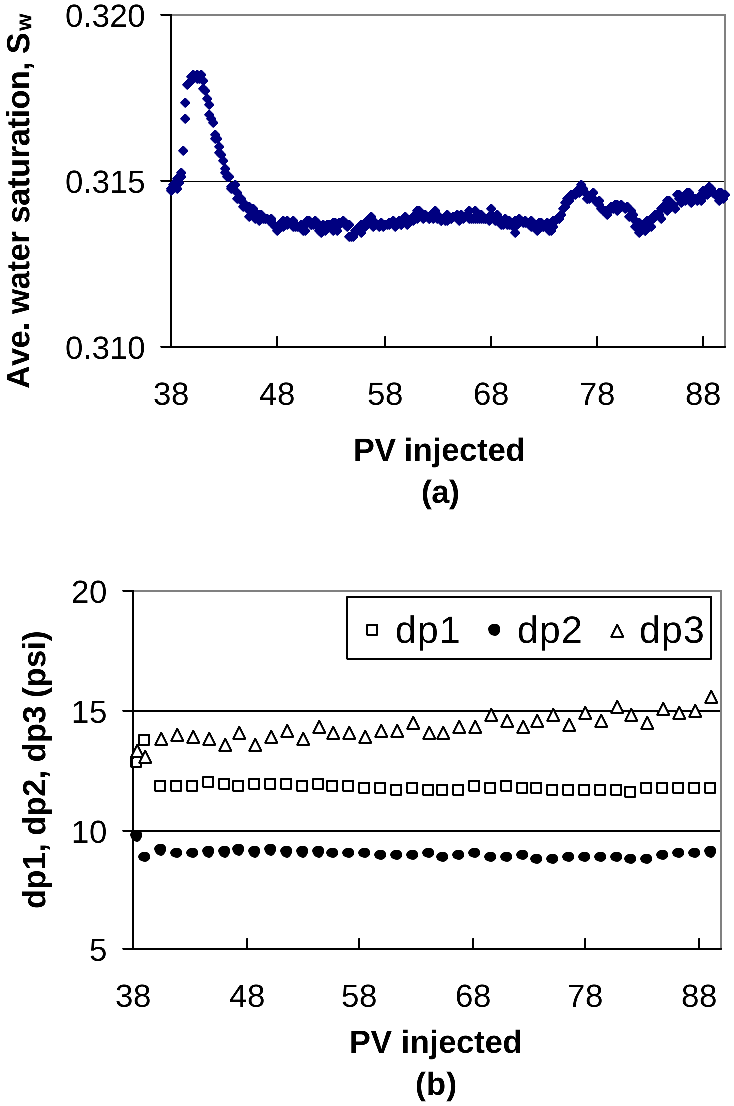

Figure 4.24 Results of Experiment II, with 0.075 wt% Shell NEODOL 91-8 surfactant solution injection at $f_w = 0.0098$ starts at 38 PV injected. (a) Average water saturation vs. pore volume injected. (b) Pressure drop in three sections of the core vs. pore volume injected.

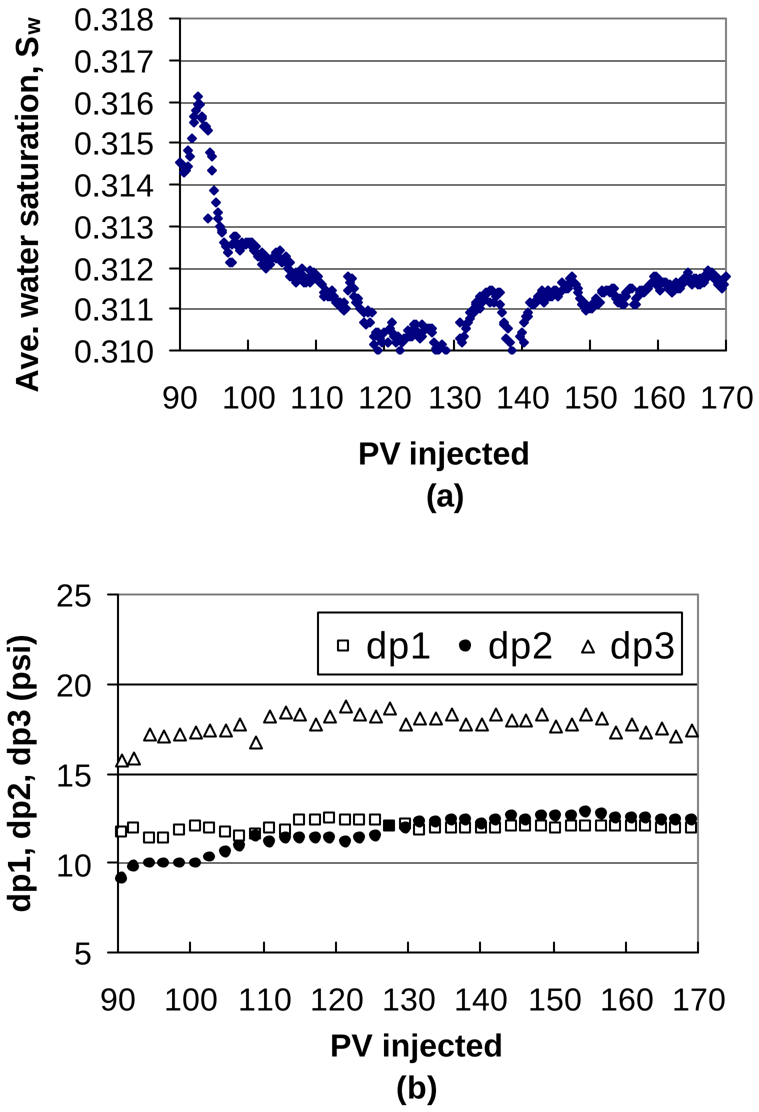

Figure 4.25 Results of Experiment II, with 0.075 wt% Shell NEODOL 91-8 surfactant solution injection at f_w = 0.0068 starts at 90 PV injected. (a) Average water saturation vs. pore volume injected. (b) Pressure drop in three sections of the core vs. pore volume injected.

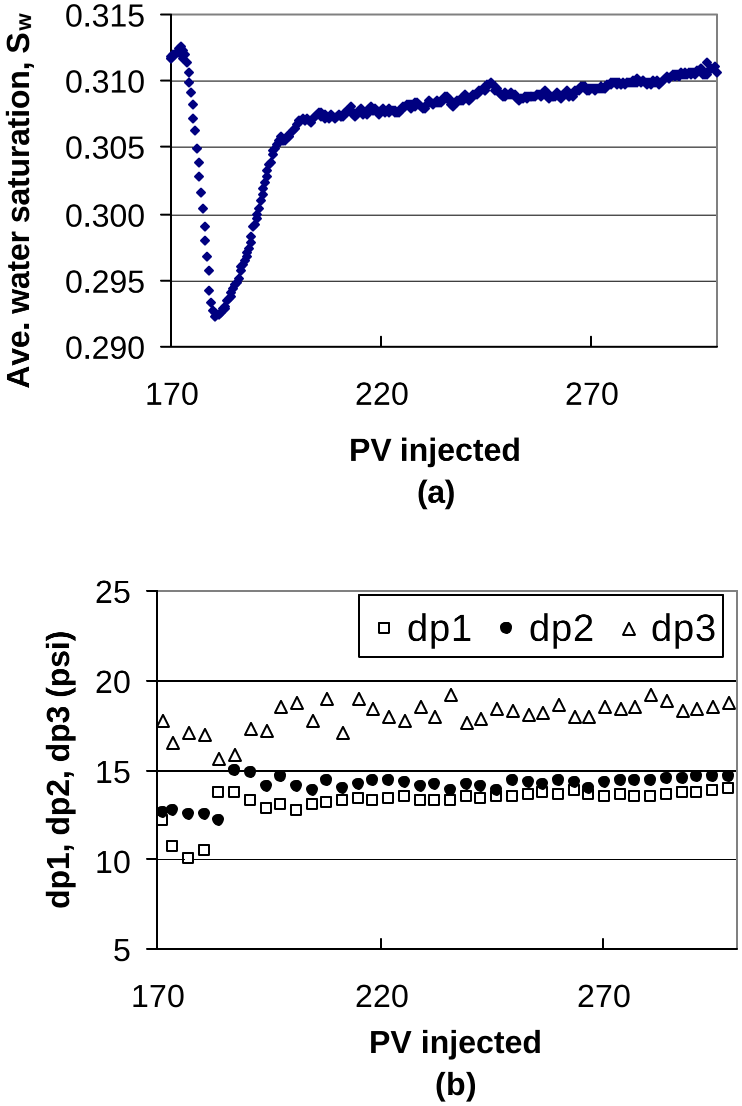

Figure 4.26 Results of Experiment II, with 0.075 wt% Shell NEODOL 91-8 surfactant solution injection at $f_w = 0.0041$ starts at 170 PV injected. (a) Average water saturation vs. pore volume injected. (b) Pressure drop in three sections of the core vs. pore volume injected.

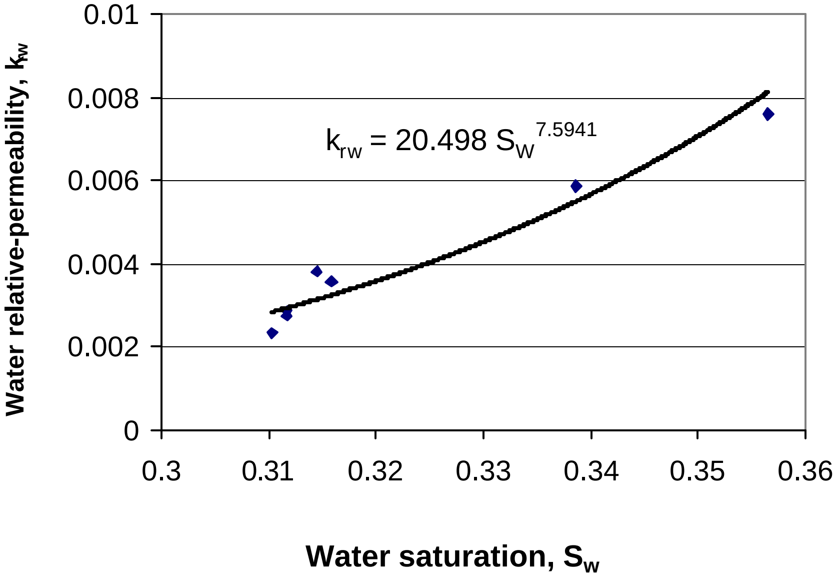

Figure 4.27 Water relative-permeability data and curve for Experiment II, with 0.075 wt% Shell NEODOL 91-8 surfactant.

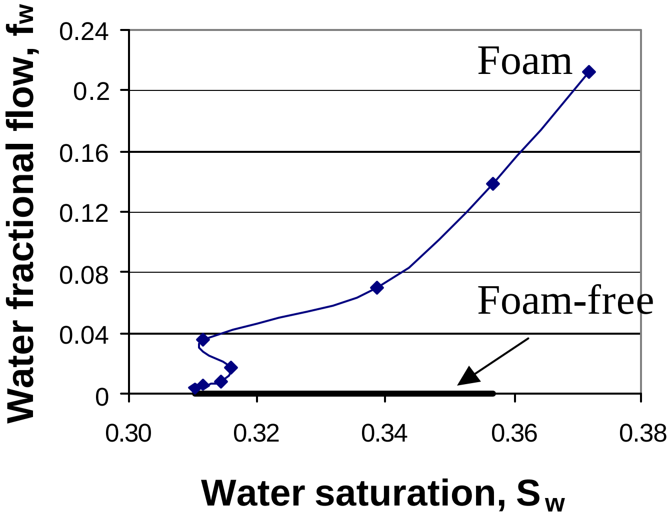

(a)

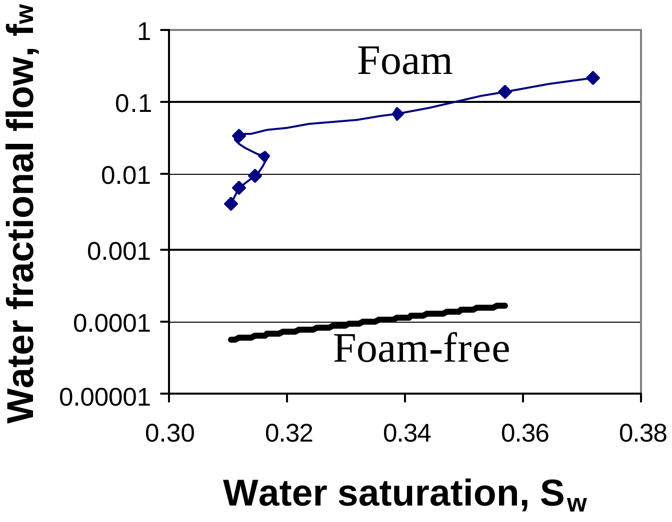

(b)

Figure 4.28 (a) Fractional flow curves from Experiment II, with 0.075 wt% Shell NEODOL 91-8 surfactant, viewed on a linear scale. (b) Comparison of foam fractional-flow curve and foam-free curve on log scale.

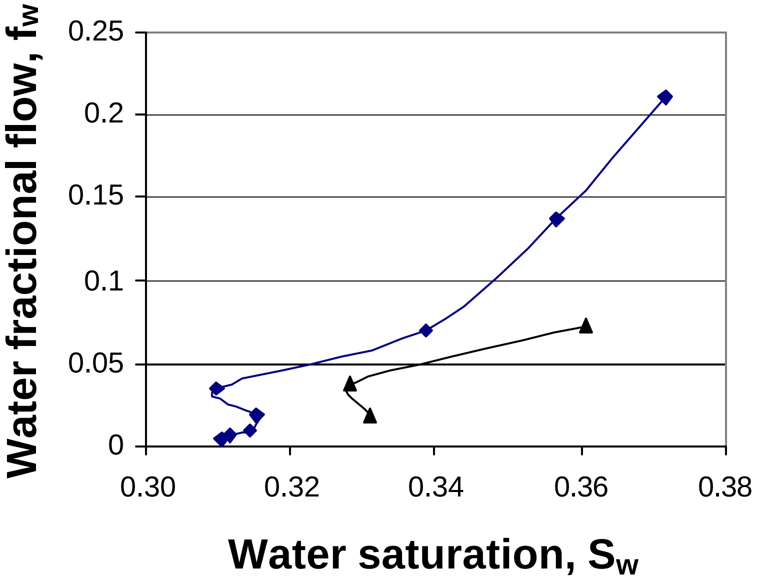

Figure 4.29 Data for fractional-flow curve from a repeat test of Experiment II, along with data for Experiment II, with 0.075 wt% Shell NEODOL 91-8 surfactant. Difference in S_w between curves may reflect in part failure to expel all gas in core at start of repeat experiment.

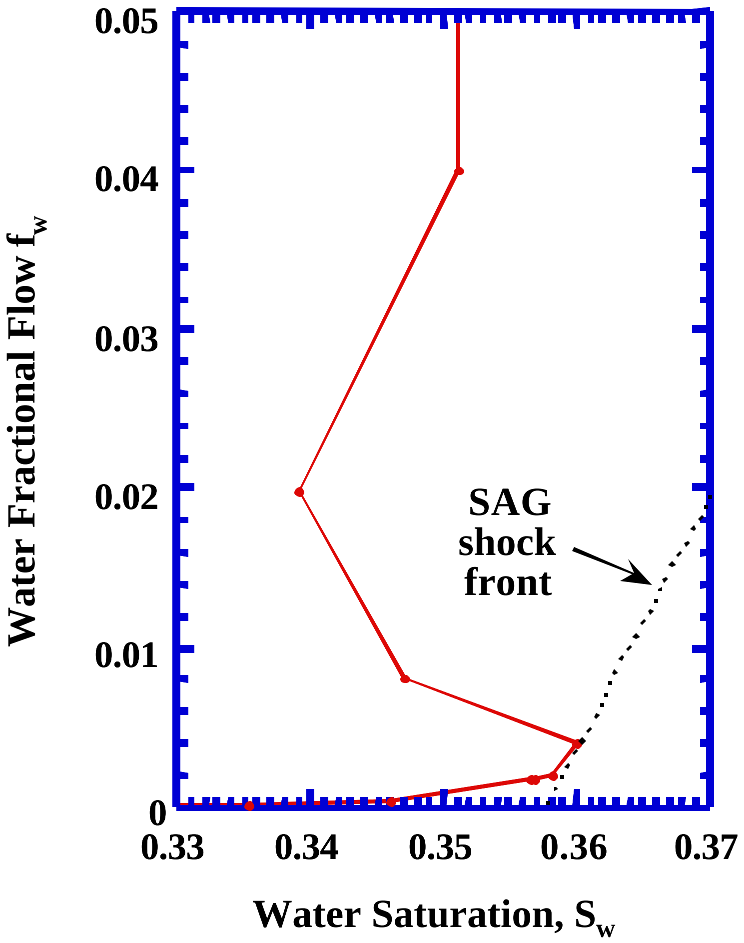

Figure 4.30 Fractional-flow curve for foam derived from coreflood data, from Kibodeaux and Rossen (1997).

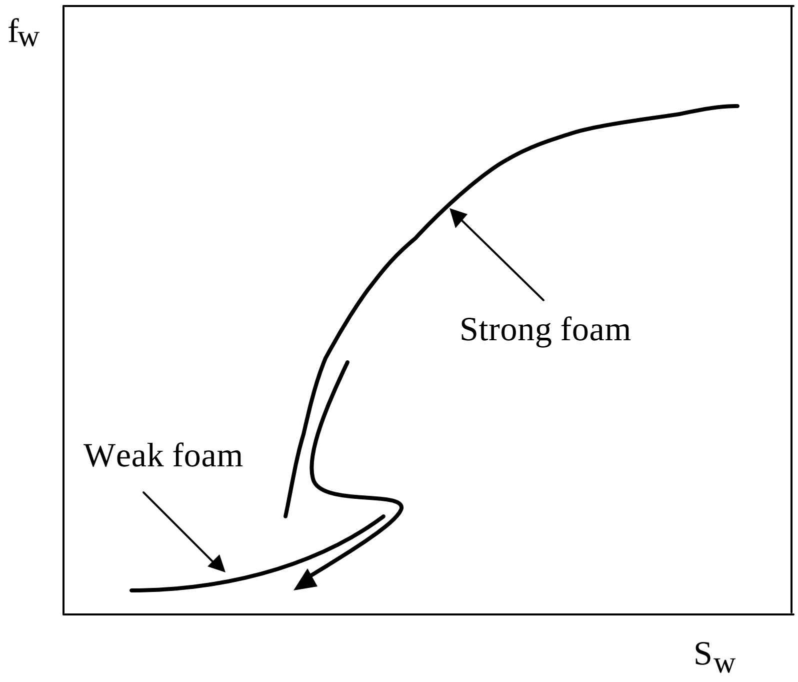

Figure 4.31 Schematic of fractional-flow curves for a foam transition from a strong foam to a weak foam.

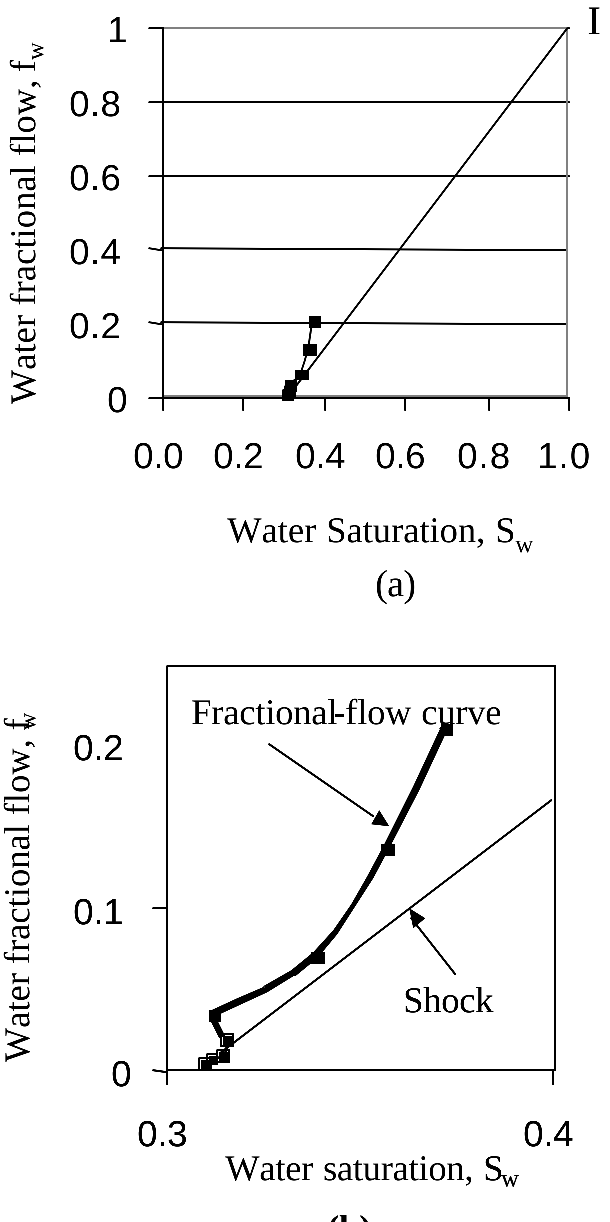

(a)

(b)

Figure 4.32 (a) Fractional-flow curve from Experiment II, with 0.075 wt% Shell NEODOL 91-8 surfactant. (b) Enlarged fractional-flow curve from Experiment II.

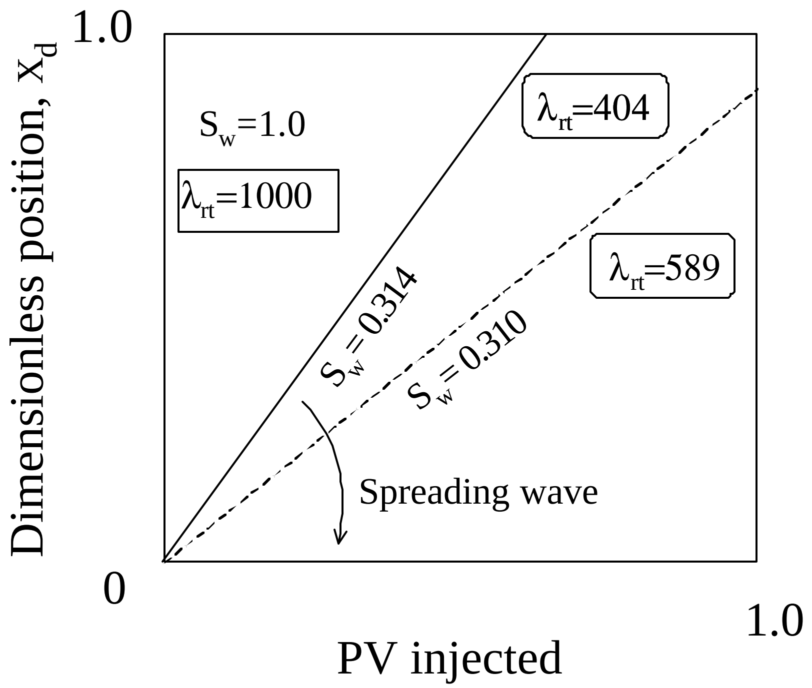

Figure 4.33 Time-distance diagram from Experiment II, with 0.075 wt% Shell NEODOL 91-8 surfactant. Numbers in boxes are total relative mobility in (Pa s)$^{-1}$.

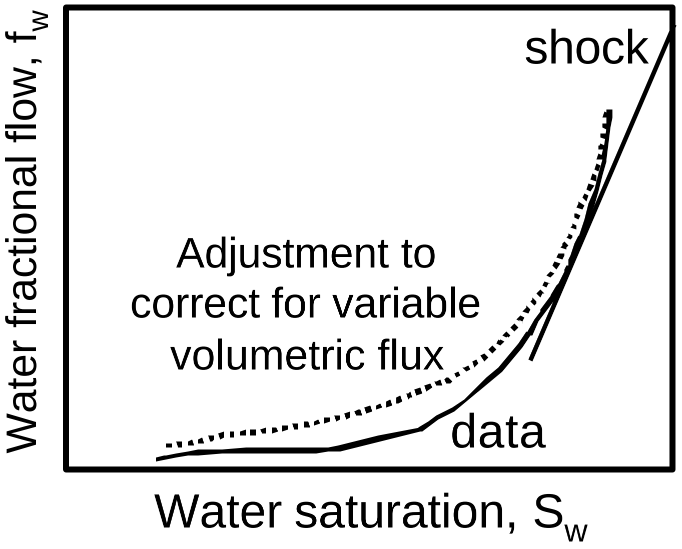

Figure 4.34 Schematic of effect of increasing total volumetric flux on data in this experiment.

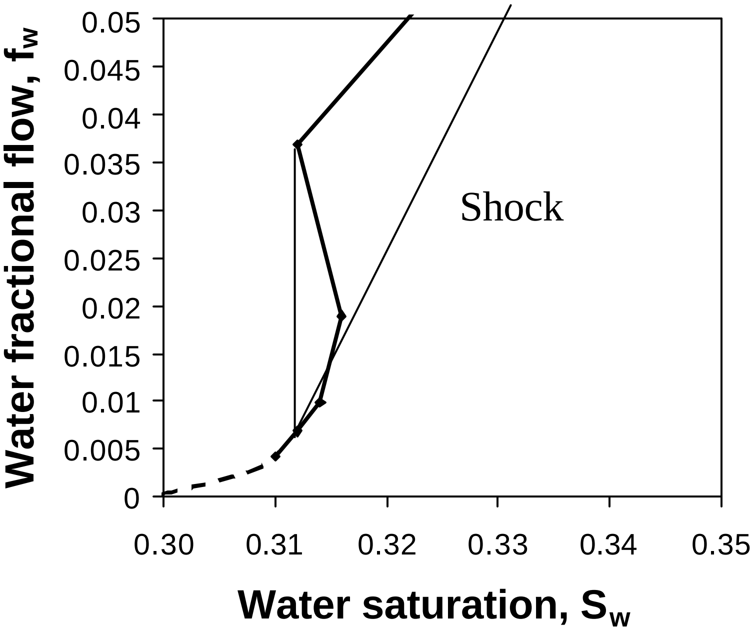

Figure 4.35 Illustration of shock construction for multi-valued fractional-flow curve from Experiment II.

Chapter 5: Experimental Investigation on Post-foam Liquid Injection

5.1 INTRODUCTION

5.1.1 Matrix acidizing process

Foams have been routinely used in matrix acidizing treatments in the petroleum industry, but with inconsistent results (Smith *et al*., 1969; Kennedy *et al*., 1992; Bernardiner *et al*., 1992; Gdanski, 1993; Thompson and Gdanski, 1993; Zerhboub *et al*., 1994; Robert and Rossen, 1995; Thomas *et al*., 1998). Matrix acidizing is a treatment for damaged sandstone or carbonate formations. Formation damage can be caused by drilling, completion, workover, or production processes. A damaged formation has plugged or constricted pore spaces, reduced permeability and reduced productivity. In an acidizing process, reactive acid is used to dissolve material in the matrix, thus increasing porosity, permeability and productivity. Acidizing reverses damage, in the sense that acidizing cleans up damage and restores productivity in the formation.

A formation may have layers that have different porosity, permeability and rock types. Layers may also have different degrees of damage. In matrix acidizing, all damaged layers need to be treated, especially the most damaged layers. However, fluid naturally flows into the most permeable zones, and may leave less-permeable and most-damaged layers un-treated or less treated. To solve this problem, foam is used to partially block the high-permeability and undamaged layers and divert acid into the less-permeable layers.

5.1.2 Foam for acid diversion

Form can greatly reduce fluid mobility. Foam does not directly alter water viscosity or the relation between water relative permeability k_{rw} and water saturation S_w, according to many studies (Bernard *et al*., 1965; Friedmann and Jensen, 1986; Huh and Handy, 1989; Sanchez and Schechter, 1989; de Vries and Wit, 1990; Friedmann *et al*., 1991), although these studies of k_{rw} with foam concern steady foam flow, not liquid injection after foam. Foam does directly reduce gas mobility, thus reducing water saturation, relative permeability and mobility greatly. Foam reduces gas mobility in part by trapping a large percentage of gas; up to 80- 99% of gas is trapped even if foam flows at high pressure gradient (Gillis and Radke, 1990; Friedmann *et al*., 1991). Foam reduces gas mobility also by increasing the effective viscosity of flowing gas (Bretherton, 1961; Hirasaki and Lawson, 1985; Falls *et al*., 1989; Rossen, 1990a,b,c,d; see also Chapter 2). These two effects are related; both depend on capillary forces, bubble size, and pressure gradient. The presence of foam in a high-permeability layer keeps liquid saturation low, so relative permeability of liquid $k_{rw}(S_w)$ is low, and this prevents too much liquid from entering the foam zone during liquid injection.

On the other hand, foam is less stable in low-permeability zones (Hirasaki, 1989; Rossen, 1996). Therefore it is possible to place foam mostly in high-permeability zones during foam injection, and maintain it during acid injection. At the same time, only weaker foam is present in low-permeability or damaged zones. Acid can then be diverted into the lower-permeability or damaged zones.

There are several choices with acidizing procedures. One can pre-flush the formation with surfactant, inject foam, and then inject foam-compatible acid. A foam-compatible acid must also contain surfactant to maintain the foam. Alternatively, one can inject alternating slugs of surfactant and gas to create foam *in-situ*. Zerhboub *et al.* (1994) also report a shut-in after foam treatment maybe beneficial. Finally, one could follow a surfactant pre-flush with a continuous injection of foamed acid. This study focuses on a process of injecting foam followed by acid. According to Kibodeaux *et al.* (1994), the key in a successful acidizing treatment is the effectiveness of gas trapping during liquid injection. The goal of foam acidizing is to trap as much gas as possible during acid injection to reduce liquid mobility in high-permeability and undamaged layers and thus facilitate diversion.

5.1.3 Previous experimental studies on gas trapping

There are several studies focused on foam behavior during post-foam liquid injection (Kibodeaux, *et al.*, 1994; Parlar, *et al*., 1995; Robert and Mack, 1995; Zeilinger, *et al*., 1995; Rossen and Wang 1999). In all these studies damage has been equated with low permeability. Low-permeability undamaged rock has been used as a surrogate for damaged rock, and high-permeability rock represents undamaged rock. This study also follows this convention.

These studies agree with each other in principle. In a typical laboratory test (Figure 5.1, from Kibodeaux *et al*., 1994), during liquid injection after foam, there is a rapid decline in pressure gradient simultaneously throughout the core to a stable plateau value as liquid injection starts. This decline is often referred to as the transition period. Pressure gradient then remains unchanged for a while before it declines further to an even lower value. This last slow decline is apparently caused by dissolution of trapped gas into the injected unsaturated liquid (Robert and Mack, 1995; Zeilinger *et al*., 1995). Unlike the first decline in pressure gradient, this second decline starts near the inlet of the core and progresses steadily downstream to the outlet.

Kibodeaux *et al*. (1994) tested both “high permeability” (847 md) and “low- permeability” (92 md) Berea cores. Their sensitivity study indicates that foam strength and especially gas trapping following foam injection are the keys to successful application. The decline in ∇p between foam and liquid injection makes the process less effective. Kibodeaux *et al.* (1994) conclude that subsequent injection of surfactant solution trapped some, but not all, of the gas in the foam in place. Gas appears to be trapped a little more effectively in the lower-permeability core, partly offsetting the benefits of foam.

Parlar *et al*. (1995) report no increase in pressure gradient upon increasing liquid injection velocity during post-foam liquid injection. In some of their results the pressure gradient was higher during the liquid-injection stage compared to the foam stage. Robert and Mack (1995) discuss these same coreflood experiments. They conclude that pressure gradient during the liquid stage following foam injection is invariant over a large range of liquid injection rates.

Zeilinger *et al*. (1995) conclude from calculation of saturation and mobilities during post-foam liquid injection that the first decline in pressure gradient ∇p observed during post-foam liquid injection corresponds to an increase in water saturation S_w of only a few percent. Some gas escapes, and gas saturation and mobility fall during this time, as expected in an environment of low capillary pressure P_c. The plateau value of ∇p does not depend on shut-in period but does weakly depend on post-foam liquid injection rate. The second decline in ∇p reflects a larger rise in S_w of about 0.2. If this decline is due to mobilization of gas bubbles, it should reflect a rise in gas mobility, which would correspond to a rise in gas saturation, not a decrease. Therefore, it is more likely that the decline in gas saturation S_g during this period reflects dissolution of gas in the flowing liquid, and the drop in S_g does roughly correspond to solubility of N_2 in the liquid. Additionally, injecting a small amount of gas with the liquid, designed to compensate for the dissolution of gas into the injected liquid, caused the second decline to disappear.

Rossen and Wang (1999) conclude that the gas that escapes during the initial period of post-foam liquid injection moves as free gas, not as foam. The foam front, which was half-way through the core after foam injection in this experiment, did not advance into the last section of core during liquid injection. Gas trapping during liquid injection is controlled by pressure gradient, and the pressure gradient required to mobilize additional trapped gas does not increase much as liquid flow rate increases greatly.

Based on these experimental and modeling studies, the following consensus has been reached on foam flow and post-foam liquid injection:

Water relative permeability k_{rw} is a unique function of water saturation S_w, even with foam. Thus, liquid flows in same narrow pores with or without foam at same liquid saturation.

In the transition period after foam injection, water saturation rises about 5% or less as k_{rw} rises; meanwhile the pressure gradient drops by up to 80%. This rise in S_w was inferred indirectly from pressure drop, not measured directly.

After the transition, a steady-state condition is reached. All gas is trapped, immobile, and evenly distributed along the core. Experiment result shows that trapped-gas saturation during post-foam injection is sensitive to pressure gradient. Cheng *et al*., (2002) take this one step further and assume that trapped-gas saturation is an unique function of pressure gradient.

The second decline in pressure gradient from the steady-state value is a result of gas dissolution into the injected unsaturated liquid. As unsaturated liquid is injected into the trapped-gas zone, with an ambient pressure of hundreds of psi, gas solubility in liquid is significant. Moreover, the second decline in pressure gradient is wave-like, moving from inlet to outlet, consistent with a dissolution process.

This consensus is the basis for foam simulators (Robert and Mack, 1995; Cheng *et al*., 2002). The model of Cheng *et al.* explicitly accounts for the effects of gas trapping on liquid mobility and the effect of pressure gradient on gas trapping. Simulations based on these assumptions fit the transition period in a qualitative way (Cheng *et al.*, 2002).

Despite these studies, post-foam liquid injection is still not fully understood. Simulations don't fit the transition period quantitatively. Specifically, the transition period lasted longer in experiments than in simulations. Attempts to quantitatively derive gas mobility and saturation changes in the transition period from pressure-gradient data have so far failed (Witteveld, 1997).

None of the above experiments measured water saturation directly. For instance, Zeilinger *et al.* (1995) inferred water saturation from pressure-gradient measurements, using a plausible water relative-permeability function for a similar rock. It is not clear whether the liquid relative-permeability function behaves the same in steady foam flow and during the displacement of foam by liquid (Rossen, and Wang, 1999). Without reliable measurement of saturation changes during liquid injection, gas trapping, gas mobility and even gas flow rate are unknown.

Dissolution has been considered the mechanism responsible for the second pressure decline, although evidence for this is not without controversy. In Kibodeaux *et al.* (1994), the second decline in pressure gradient is too rapid to represent dissolution of all the gas present (Figure 5.1). That is, the volume of injected liquid is not enough to dissolve all the gas present at the rate at which pressure gradient declines. The solubility of N_2 in water (Fogg and Gerrand,

1991) suggests that 11 PV of liquid could dissolve enough gas to raise S_g by about 0.14. In Figures 5.1 this is sufficient to move the dissolution wave through the core, but it represents only about one-quarter of the gas present at the start of liquid injection.

In one experiment, Zeilinger *et al*. (1995) co-injected a small amount of gas with liquid during liquid injection. However, due to equipment limitations, gas injection rate was a little more than enough to saturate the liquid. Thus, there was free gas moving as well as liquid, and the test was imperfect.

An alternative explanation is that another mechanism, like mobilization, may be responsible as well for the second decline in pressure gradient in Figure 5.1.

Motivated by trying to close the above gaps in previous studies, a new experimental study was conducted, with water saturation measured directly. The water relative-permeability function was obtained in previous experiments (Chapter 4). Therefore, the accuracy of the water relative-permeability function during post-foam liquid injection can be verified. Gas trapping and gas flow rate during the transition period can also be estimated with greater confidence, since water (and therefore gas) saturations are known.

5.2 EXPERIMENTAL DESIGN

As in previous experimental studies (e.g., Kibodeaux *et al*., 1994), there were two stages in our experiments. The first was steady-state foam injection, then liquid injection only. Flow velocities and foam formulation differed from previous studies. Most important, saturation was measured directly.

The total nominal superficial velocity during foam injection was 5.827 ft/d, with the gas superficial velocity estimated at the back-pressure of 150 psi; gas superficial velocity was lower upstream. Post-foam liquid superficial velocity was 4.66 ft/d, approximately the same as total superficial velocity at the inlet during foam injection. By matching total superficial velocities during foam and liquid injection, the foam in flow lines (dead volume) upstream of the core flows into the core at the start period of liquid injection at the same velocity as during foam injection. This reduces the impact of the dead volume on the results (Cheng *et al*., 2002).

It also makes sense to inject foam and post-foam liquid at same volumetric rate from a field prospective. In the field, one slug may be only part-way down the tubing when the next slug is initiated at the surface (Gdanski, 1993). Even if pumping rates for slugs differ at the surface, this would not correspond to the time at which slugs reach the rock face.

Knowing how saturation changes during post-foam liquid injection is essential for understanding this process. Among methods of saturation measurement, MRI and CT scans are expensive and inconvenient, and no facilities for such scanning were available to this research. A mass-balance method is not sufficiently accurate for experiments that involve large liquid volumes and last many days, due to possible evaporation, among other problems. Weighing the core to determine average saturation on a moment-by-moment basis was used in these experiments.

The surfactant used was Shell NEODOL 91-8. No acid was used in these experiments, because the objective was to investigate mechanisms of gas trapping, not acid dissolution of damage.

The experimental procedure in these experiments included the following steps: First, measure porosity and permeability of a new core according to the procedure in Chapter 3. Then establish the initial state of 100% water saturation. Inject surfactant and gas to generate foam, and reach steady-state foam flow. Then inject surfactant solution only, until the second decline in pressure gradient (Figure 5.1) has moved to the end of the core. Throughout, measure average water saturation in the core and pressure gradient in three sections along the core.

Three experiments were conducted. Experiment I was conducted with the following conditions: During foam injection, nominal gas superficial velocity u_g was 5.83 ft/d (at core back-pressure and room temperature), and liquid superficial velocity u_w was 0.583 ft/d (15 cc/hr). Nominal foam quality was 90.9%. The concentration of Shell NEODOL 91-8 was 0.2%. During liquid injection after foam, nominal superficial velocity of liquid was 4.584 ft/d (120 cc/hr).

Experiment II was conducted with u_w =0.0583 ft/d (1.5 cc/hr), u_g= 5.83 ft/d at the core back-pressure during foam injection. surfactant concentration was the same as in Experiment I. Nominal foam quality was at 99%, but, due to gas compression, true foam quality was lower in most of the core. During liquid injection, u_w was 4.584 ft/d (120 cc/hr). Notice that liquid injection rate increased 80 fold during liquid injection after foam.

Experiment III was conducted with the same injection rates as in Experiment I, except surfactant concentration was 0.8 wt% instead of 0.2 wt%. In addition, the effluent was weighed instead of the core itself. Part of the objectives of this experiment was to verify the surprising saturation behavior observed in experiments I and II.

Injection rates and surfactant concentrations were relatively low to avoid building pressure above the limits of the apparatus, as discussed in Chapter 3.

5.3 EXPERIMENTAL RESULTS

5.3.1 Experiment I

Steady-state foam injection

Results of Experiment I are shown in Figure 5.2. During steady-state foam injection, average water saturation in the core S_w was 0.337. Pressure drops were 22.0 psi in sections 1 and 2 (∇p = 66.0 psi/ft). Pressure drop in section 3 was higher than the limit of the pressure transducer (80 psi) during the unsteady-state foam-generation period. To protect the transducer, the transducer line was closed and pressure drop in section 3 wasn't recorded until shortly (10 minutes) before switching to liquid-only injection. Recorded pressure drop in section 3 was about 32.0 psi (96.0 psi/ft) during steady-state foam injection just before liquid injection (Figure 5.2(b)). The deviation of pressure drop in section 3 from that in the other sections may be a result of the capillary end-effect and/or variation of gas flow velocity along the core, due to gas compressibility. Due to the variation of pressure along the core, pressure at the middle of section 3 was 166.0 psi; pressure at the middle of section 1 was 215.0 psi. Thus, volumetric gas flow rate in section 3 was 1.3 times of that in section 1. If the variation of gas flow velocity caused the higher pressure drop in section 3, however, it is unclear why it did not affect section 2.

A water relative-permeability function,

$$k_{rw} = 20.0\, S_w^{\,7.59} \tag{5.1}$$

obtained from a previous experiment for the same core "B" (Chapter 4) fits the steady-state pressure gradient and pressure drop well. Predicted pressure gradient is 61.15 psi/ft from Darcy's law at $S_w = 0.337$, close to the measured pressure gradient of 66.0 psi/ft in sections 1 and 2. To fit ∇p exactly, one would need $S_w = 0.333$. This good agreement with $k_{rw}(S_w)$ determined with a different foam formulation in the same core supports the finding of previous studies that $k_{rw}(S_w)$ is independent of foam. It also suggests that both experiment were conducted with the same initial gas saturation (presumably, zero), though the core was re-used.

The stable sectional pressure drops and stable average saturation indicates that steady-state foam flow had been established.

The transition period

The transition period between steady-state foam injection and the later period is very short, as shown in Figure 5.2(a). In this experiment, as liquid injection rate increased and gas injection ceased at about 39.75 PV (pore volume injected), a rapid increase in average water saturation and pressure was observed. S_w increased from 0.337 to 0.42 in about 0.18 PV (*i.e.*, 14 minutes). Such a rapid transition would be difficult to resolve in a CT or MRI scan.

The measured increase in water saturation (0.083) was larger than that inferred indirectly in previous studies (Kibodeaux, *et al*. 1994, Zeilinger *et al*. 1995) with stronger foam. Inferred from pressure-gradient data, water saturation increased during the transition in the experiment of Kibodeaux *et al*. (1997) by about 0.05.

After the transition period, water saturation changed much more slowly. The injected liquid broke through at core outlet at the end of the transition period, as observed visually in the plastic flow line at the core outlet.

Pressure gradient in all three sections *increased* during the transition (Figure 5.2(b); *cf*. Figure 5.1). Pressure drop increased to 26.0 and 33.0 psi (∇p = 78.0 and 99.0 psi/ft) in sections 1 and 2, respectively; whereas pressure drop increased to 53.0 psi (∇p = 159 psi/ft) in section 3. An increase in pressure drop during post-foam liquid injection has been reported only by Parlar *et al*. (1995). Kibodeaux et al. (1994) concluded that the decline in ∇p during liquid injection in their experiments (Figure 5.1) would harm foam effectiveness in the field.

An increase in pressure gradient upon liquid injection is consistent with the model of Cheng *et al*. (2002), though this possibility is not noted by Cheng *et al.* From the data of Rossen and Wang (1999) for pressure gradient ∇p as a function of liquid superficial velocity u_w, combined with the relative-permeability function of Persoff *et al*. (1991), Cheng *et al*. (2002) inferred the trapped-gas saturation S_{gr}^f as a function of ∇p, shown in Figure 5.3. Here we use $S_{gr}^f(\nabla p)$ from Figure 5.3 as a plausible function for our core and surfactant formulation, along with the relative-permeability function in Eq. 5.1, to estimate S_{gr}^f and ∇p during liquid injection after foam in our experiment. The two constraints to be satisfied by S_{gr}^f and ∇p are the relationship in Figure 5.2 and Darcy's law applied to the liquid phase (using $k_{rw}(S_w)$ from Eq. 5.1). For u_w = 4.59 ft/d, one obtains S_{gr}^f = 0.594 and ∇p = 112.2 psi/ft: close to the averate for the three sections of our core. a remarkably good match to our data given all the assumptions involved. ∇p increases during liquid injection because the increase in u_w is so large, which in turn reflects the high foam quality (low u_w) during foam injection in these experiments. Cheng *et al.* (2002) missed this possibility because the experiments they matched mostly held u_w constant during foam and post-foam liquid injection, and in all cases used lower foam qualities.

Liquid superficial velocity increased by a factor of 7.86 from that of the foam injection period during liquid-only injection. Pressure gradient however, increased by a factor of 1.45 in section 1 and 1.65 in section 3. Thus, though ∇p increased, liquid mobility actually increased by a factor of 5.42 in section 1 and 4.75 in section 3. Therefore, the increase in pressure gradient during liquid injection in Experiment I results mainly from the increases in liquid superficial velocity.

The transition took place in 0.1 PV to 0.15 PV (14 to 19 minutes) for both sectional pressure drops and average water saturation (Figure 5.2(b)). The pressure drop peaked in sections 1 and 2 before decreasing but rose monotonically in section 3. In Kibodeaux *et al*. (1994), ∇p declined in the transition period and the transition took about 1-3 PV (Figure 5.1).

There is good agreement between the measured change in water saturation and that inferred from measured ∇p. Average water saturation increased from 0.337 to 0.42, as determined from core weight. Calculated from pressure-gradient data and Eq. 5.1, water saturation was 0.429, 0.414, and 0.390 in sections 1, 2 and 3, respectively, after the transition; average water saturation in the core was then 0.41, inferred from the ∇p data. The good agreement between S_w measured directly and inferred from ∇p data using the $k_{rw}(S_w)$ (Eq. 5.1) function suggests that the same $k_{rw}(S_w)$ function applies to foam flow and post-foam liquid injection. This is the first experimental confirmation of this point (*cf*. Rossen and Wang, 1997). These same results are expressed in terms of gas saturations in Table 5.1, lines 7-9.

In most previous studies (Figure 5.1), pressure declined during liquid injection after foam. Most of the gas that escapes during the transition period in those studies represents the increase in gas volume resulting from gas compressibility and the decrease in pressure. Cheng *et al*. (2002) show that gas expansion and outflow considerably lengthens the transition period. With an increase in pressure in Experiment I, the transition is much shorter, and gas saturation falls due both to compression and to any outflow of gas. Table 5.1 shows that most of the decrease in gas saturation during the transition in Experiment I results from gas compression; very little gas leaves the core. That is, if all gas were trapped and gas volume simply shrank from compression, the final gas saturation (line 7 of Table 5.1) would be only a little higher than that measured directly from core weight (line 9). This inference is supported by the fact that little or no gas was observed passing through the translucent plastic tubing near the core outlet during the transition period. Table 5.1, lines 5 and 6, imply that gas escapes the core during the transition period originates primarily from section 3.

Later period

Pressure drops in section 1 and 3 held steady before they declined (Figure 5.2), as in previous studies (*cf*. Figure 5.1).

In section 2, pressure drop dp2 rose until the presumed dissolution wave hit at 42.5 PV, when it declined sharply. Pressure drops declined to low level sequentially in the three sections (Figure 5.2(a)).

Average water saturation, S_w, continued to rise as dp2 rose, then fell starting at 42.5 PV as the dissolution wave passed through sections 2 and 3, then slowly rose again starting at 50.0 PV.

Liquid superficial velocity inside the core stayed almost unchanged during this period. Specifically S_w rose slowly by 0.025 (from 0.425 to 0.45, or 3.6 cc liquid accumulation in the core) over an injection period of 2.5 PV (3 hrs). From a mass-balance over the 3-hour period of liquid injection in the core, we have

Effluent = Injection (114 cc/hr x 3 hr) – change in saturation (3.6 cc)
= (112. 8 cc/hr x 3 hr)

Thus, liquid flow rate inside the core didn't vary much; between 112.8 cc/hr (4.370 ft/d) and 114 cc/hr (4.428 ft/d), or about 1%.

During the later period, in each section pressure gradient is at first either steady or rising, then declines sharply, then declines much more slowly. If under-saturated injected liquid reached equilibrium with resident gas at each position before advancing through the core, the liquid wave would dissolve all gas in the core at each position before advancing. As in previous studies, the rate of advance of the dissolution wave is too rapid to account for all the gas in the core. It appears therefore that liquid dissolves all or most gas within some portion of the core as it advances, e.g. in a higher-permeability streak. Meanwhile it bypasses most trapped gas in the core. Once a channel were cleared of gas, most liquid would flow through this channel rather than sweep the core evenly. The advance of under-saturated liquid through this channel is reflected in the decline in ∇p in our data. Slowly, bypassed gas diffuses to the channel and is removed.

This hypothesis explains the sharp, sequential decline in ∇p in the three sections of the core in Figure 5.2 and the slower decline in ∇p after the front passes each section. It also implies that water saturation is very non-uniform behind the front. That in turn implies that a $k_{rw}(S_w)$ function derived from uniform flow (Eq. 5.1) would perform poorly in relating ∇p to S_w once the dissolution wave has passed.

Tables 5.1 to 5.3 show calculations of the potential effects of changing ∇p and absolute pressure, gas dissolution and gas expansion on flow during the later period. The processes involved are complex: Gas dissolves, some gas may escape, ∇p declines, and trapped gas expands. But since dissolution reduces S_g, and S_{gr}^f increases as ∇p decreases (Figure 5.3), this expanding trapped gas may or may not be able to escape. The calculations in Tables 5.1 to 5.3 assume that trapped gas does not escape, and that Eq. 5.1 continues to define $k_{rw}(S_w)$, and therefore to relate ∇p to S_w, during this entire period.

Some conclusions from Tables 5.1 to 5.3 are as follows.

1) Eq. 5.1 does not describe liquid flow after the dissolution front passes. The most glaring failure is evident from the comparison in Table 5.3 of S_g estimated from sectional ∇p's and from core weight: while falling ∇p suggests a rise in S_w as the dissolution wave passes through section 3, in fact S_w decreases during this period. The deviation between core-average S_w inferred from ∇p and Eq. 5.1 and determined from core weight increases as the dissolution wave moves through the core (*cf*. Table 5.2, lines 6 and 7; lines 11 and 12; and Table 5.3, lines 6 and 7.)

2) Therefore, it is infeasible to back-calculate the changes in saturation in each section during this period from ∇p in that section; Eq. 5.1 does not describe liquid flow behind the dissolution front.

3) A qualitative explanation for the unexpected fall in S_w is possible, however. There is a sufficient trapped gas behind the dissolution front to account for the decrease in S_w as pressure falls throughout the core and this trapped gas expands (*cf*. line 4, Table 5.3). A rise, fall, and rise in core-average water saturation is plausible, reflecting a competition between gas removal at the

dissolution front and a large increase in trapped-gas saturation behind the front, due to declining pressure there. We hypothesize that all gas is trapped at the end of the transition period. Then as the dissolution front passes, dissolution reduces S_g, and ∇p declines, which increases the maximum trapped-gas saturation S_{gr}^f (Figure 5.3). Both effects mean that the remaining gas can expand and remain trapped. The expanding gas in sections 1 and 2 accounts for the decreasing average water saturation in the core as the dissolution wave passes through section 3 and pressure declines significantly upstream of this section.

Experiment III, described below, is a direct test whether the change in S_w inferred from core weight in this experiment is real or an artifact.

It is tempting to conjecture that section 3 is at the maximum trapped-gas saturation S_{gr}^f immediately after the transition period; section 2 ends the transition period below S_{gr}^f and then accumulates gas, for a time, before the dissolution wave arrives; and section 1 is below S_{gr}^f throughout. Without further evidence, however, this remains a conjecture.

5.3.2 Experiment II

Steady-state foam injection

The total nominal superficial velocity during foam and post-foam liquid injection was the same in Experiment II as in Experiment I, but nominal foam quality was 99%. Results are shown in Figure 5.4. Water saturation was 0.268 during the steady-state foam injection. The lower S_w is consistent with the higher foam quality. Pressure drops in section 1 and 2 were about 10 psi (∇p = 30 psi/ft). Pressure drop in section 3 slightly fluctuated around an average of 17 psi

(∇p = 51 psi/ft). Pressure gradient predicted at S_w = 0.268 (Eq. 5.1) is 34.8 psi/ft, close to the core-average of 37 psi/ft. The fit is especially remarkable since S_w = 0.268 lines well outside the range of the $k_{rw}(S_w)$ data on which Eq.1 was based (Table 5.2).

It is not clear why pressure drop fluctuates in section 3. Though foam flow in section 3 was drier than that upstream, due to gas expansion. At the middle of section 3, pressure was 158.5 psi; at the middle of section 2, pressure was 172 psi; at the middle of section 1, pressure was 182 psi. Thus, average gas flow rate was 1.15 times higher in section 3 than in section 1.

The stable pressure drops in the first two sections, and stable average water saturation suggests that a steady state had been established.

The transition period

As liquid injection rate increased by a factor of 78.6 and gas injection ceased at about 16.0 PV, a rapid increase in water saturation and pressure gradient was observed. S_w increased from 0.268 to 0.45. The transition took place in about 0.24 PV (18 minutes).

Pressure drops in all three sections increased during the transition (Figure 5.4(b)). Pressure drop increased to 16.0, 26.0 and 36.0 psi (∇p = 48, 78 and 108 psi/ft) in sections 1, 2 and section 3, respectively.

Liquid superficial velocity increased by a factor of 78.6 between the foam-flow period and post-foam liquid injection. Pressure drops, however, increased by a factor of 1.6, 2.6 and 2.1 in sections 1, 2 and 3 respectively. Thus, liquid mobility increased by a factor of 49.0, 30.2 and 37.4 in sections 1, 2 and 3 respectively. Mobility increases were much higher compared to that in Experiment I. With lower pressure gradient (78.0 psi/ft vs. 110.0 psi/ft in Experiment I) at same liquid superficial velocity after the transition, the liquid mobility during post-foam liquid injection in this experiment was 1.4 times higher than that in the Experiment I. This suggests that the 99% quality foam was less effective in trapping gas than the 90% quality foam in Experiment I, even at a lower pressure gradient than Experiment I. In the model of Cheng *et al.* (2002), foam quality during foam injection does not affect trapped-gas saturation in post-foam liquid injection. This model may need to be revised. Further investigation on optimization of foam quality for acid diversion is needed.

The transition took place in 0.24 PV (18 minutes) (Figure 5.4(b)), which is slower than in Experiment I. This is reasonable because the change in water saturation was larger here.

A mass-balance on gas saturations indicates that only a small amount of gas escaped during the transition period (Table 5.4). Measured average water saturation in the core increased from 0.26 to 0.45 during the transition. Water saturations inferred from ∇p data and Eq. 5.1 are 0.589, 0.513, and 0.546 in sections 1, 2 and 3 respectively, for an average of 0.569. This suggests that, again, the $k_{rw}(S_w)$ function derived from steady-state foam flow works reasonably well during liquid injection after foam. The fit to S_w determined from core weight (0.543) is not quite as good as in Experiment I. One should note that in both cases, however, the values of S_w lie outside the range of the original $k_{rw}(S_w)$ data in Table 5.2.

Later period

Pressure drops in sections 1 and 2 held mostly steady, as in previous studies, though declining a little, after the transition. In section 3, dp3 rose until the presumed dissolution wave hit, when it declined sharply.

Average S_w continued to rise as dp2 rose, then fell as the dissolution wave passed through sections 2 and 3, then slowly rose again. Average water saturation decreased as pressure gradient in section 3 declined later after 22.5 PV. This trend is similar to that in Experiment I (Figure 5.2).

After 30 PV, ∇p was low throughout the core. Injection of surfactant solution continued until 50 PV. The increase of water saturation during this time provides insight into the gas-dissolution process. From 35 to 50 PV, S_w increased from 0.53 to 0.65 (Figure 5.5). Therefore, the average volumetric rate of gas dissolution during this time was 0.12 PV /15 PV = 0.008 = 8 cc/L. This is a little less than the equilibrium solubility of N_2 in water derived from data in Fogg and Gerrand (1991), *i.e.*, 12.6 (cc/L atm) (see Appendix D for more details). Mass solubility is linearly related to pressure. Thus, a unit volume of liquid dissolves same volume of N_2 at any pressure.

Water passing through the core late in the experiment absorbed about 2/3 of the equilibrium solubility of N_2, and left the core still unsaturated. Earlier in the experiment, injected liquid dissolved some gas near the core inlet but then came rapidly to equilibrium in a relatively narrow dissolution front as the liquid passed through that front downstream.

In principle, some of this gas should come back out of solution at lower pressure downstream of the dissolution front. It is possible that this explains the rise in dp3 in Experiment II and in dp2 in Experiment I. But if so, we have still no explanation why this rise did not occur in other sections.

5.3.3 Experiment III

Steady-state foam injection

Experiment III was conducted with the same 90% foam quality but a higher surfactant concentration (0.8 wt%) than Experiment I. More important, however, the core wasn't weighed. Instead, the effluent was weighed in this experiment. Results are shown in Figure 5.6. Pressure drops were 20.0, 25.0 and 28.0 psi (∇p = 60, 75, and 84 psi/ft) respectively in the three sections (see Figure 5.6). Pressure gradients were not too different from those in Experiment I, despite the difference in surfactant concentration. Stable pressure drops in the sections indicated steady-state foam flow.

The transition period

As liquid injection rate increased and gas injection ceased at about 7.89 PV, a rapid increase in pressure drops was observed. Pressure drop increased to 27.0, 45.0 and 41.5 psi (∇p = 81, 135, and 124.5 psi/ft) in sections 1, 2 and 3 respectively (see Figure 5.6(b)). The transition in pressure drops took place in about 0.18 PV (14 minutes).

Average water saturation can be inferred from weighing the effluent; the result is illustrated in Figure 5.7. The vertical axis represents the mass difference between injected liquid (known from pump rate) and produced liquid (known from effluent weight); it represents the liquid accumulated in the core plus the flow lines from the core outlet to the outlet of apparatus. Effluent was weighed from the start of post-foam liquid injection, when injected liquid reached the core, as shown at point "A" in Figure 5.7. The transition period ended at point "B", where liquid broke through at apparatus outlet and the rate of effluent suddenly increased.

A mass balance can be performed to estimate the change in average liquid saturation in core as follows: Liquid injection rate was 1.9 cc/min. The total liquid injection during the transition period (20 minutes) was 1.9 x 20 = 38 cc or 38 grams (assuming the density of the surfactant solution was approximately 1 g/cc). The produced liquid was 6.91 g at point "B". The difference, 31.09 g, is what was left in the core and the flow lines. The volume of the flow lines was measured separately to be 15 cc using a graduated cylinder, and we assume that at point "B" the flow line was filled with liquid. Then, a total of (31.09-15) = 16.09 g of liquid was left in the core during the first twenty minutes.

This represents an increasing average water saturation S_w of 0.11 during the transition. This increase in water saturation is similar to the increase of 0.09 in Experiment I. The difference may be partly due to the difference in surfactant concentration in the two experiments.

Later period

Pressure drop in section 2 held steady, as in previous studies, while dp1 declined just slightly before the dissolution wave started.

In section 3, dp3 rose until the dissolution wave hit, when it declined sharply. Pressure drops behaved similarly to Experiment I, except that pressure drop in section 3 increased for a while instead of section 2.

The average water saturation in the core inferred from the effluent weight, increased by 0.07 from 8 to 12.5 PV (5.7 hrs). S_w increased by only 0.025 from 40 to 42.5 PV (3 hrs) in Experiment I (Figure 5.2). If evaporation reduced the mass of effluent in its beaker over a period of 5.7 hours, this could explain part of the difference. But the effluent beaker was loosely sealed with plastic wrap, so we don’t believe this can explain the difference. Moreover, the decrease in S_w from 13 to 17 PV (Figure 5.7) is also larger than in Experiment I. Presumably the difference in surfactant concentrations between Experiments I and III accounts for these differences.

The trend in Experiment III (Figure 5.7) matches that in Experiment I (Figure 5.2) and II (Figure 5.4): liquid saturation rises, then falls, then rises as the dissolution wave passes through the core. Two different methods of determining water saturation in the core agree. The trend is real.

5.4 CONCLUSIONS

For the first time, the average water saturation during post-foam liquid injection has been measured. Water saturation increased by a larger amount than in previous studies.

Pressure gradient can be larger during liquid injection than during foam injection if liquid injection rate increases sufficiently during post-foam liquid injection: that is, if foam quality is high enough. Further work is needed to determine what advantage this offer, and the optimal quality for foam injection.

The ultimate trapped-gas saturation and liquid mobility during post-foam liquid injection depend on injected foam quality. This implies that the model of Cheng *et al*. (2002) for foam-acid diversion may need to be refined.

In these experiments, a water relative-permeability function that fit foam flow also roughly fit post-foam liquid injection before dissolution starts to alter the process. After gas dissolution, however, the relative-permeability function is no longer accurate.

In these experiments, water saturation rose, then fell, then rose again after the initial transition period after foam injection. These results are consistent with water saturation changes by gas dissolution and expansion of trapped gas.

Table 5.1 Effect of compression on gas saturation at start of liquid injection (Experiment I)

		notes	Sect. 1	Sect. 2	Sect. 3
1	S_g from ∇p data[1]	s.s. foam (35-39 PV)	0.666	0.666	0.683
2	ave. p (psi)[2]	"	215	193	166
3	ave. p (psi)[2]	end transition (40 PV)	251	221	177
4	ratio of pressures before and after transition		0.857	0.873	0.938
5	S_g inferred from p change alone[3]	end transition (40 PV)	0.570	0.581	0.641
6	S_g from ∇p data[1]	"	0.571	0.586	0.610
7	core-ave. S_g inferred from pressure change alone (row 5)	"	0.597		
8	core-ave. S_g from ∇p data (row 6)	"	0.589		
9	core-ave. S_g from core wt.	"	0.575		

[1] - inferred from ∇p data and $k_{rw}(S_w)$ from Eq. 5.1

[2] - from ∇p data

[3] - assuming all gas in s.s. foam (line 1) is trapped and is compressed by change in pressure

Table 5.2 Effect of decompression as dissolution wave passes through sections 1 and 2 (Experiment I)

		notes	Sect. 1	Sect. 2	Sect. 3
1	S_g from ∇p data[1]	end transition (40 PV)	0.570	0.581	0.610
2	ave. p (psi)[2]	"	251	221	177
3	ave. p (psi)[2]	dissoln. wave exits sect. 1 (42.6 PV)	246	222	176
4	S_g inferred from pressure change alone[3]	"		0.578	0.613
5	S_g from ∇p data[1]	"	0.499	0.594	0.608
6	core-ave. S_g from ∇p data (row 5)	"	0.567		
7	core-ave. S_g from core wt.	"	0.550		
8	ave. p (psi)[2]	dissoln. wave exits sect. 2 (44.5 PV)	215	208	176
9	S_g inferred from pressure change alone[4]	"	0.570		0.613
10	S_g from ∇p data[1]	"	0.451	0.519	0.608
11	core-ave. S_g from ∇p data (row 10)	"	0.526		
12	core-ave. S_g from core wt.	"	0.570		

[1] - inferred from ∇p data and $k_{rw}(S_w)$ from Eq. 5.1

[2] - from ∇p data

[3] - assuming all gas in present at end of transition (line 1) is trapped and is altered by change in pressure. This only makes sense for sections 2 and 3; in section 1, dissolution is reducing S_g.

[4] - assuming all gas in present as dissolution wave exits section 1 (line 5) is trapped and is altered only by change in pressure. This only makes sense for sections 1 and 3; in section 2, dissolution is reducing S_g.

Table 5.3 Effect of decompression as dissolution wave passes through section 3 (Experiment I)

		notes	Sect. 1	Sect. 2	Sect. 3
1	S_g from ∇p data[1]	dissoln. wave exits sect. 2 (44.5 PV)	0.451	0.519	0.608
2	ave. p (psi)[2]	"	215	208	176
3	ave. p (psi)[2]	dissoln. wave exits sect. 3 (50.0 PV)	166	163.5	155.5
4	S_g inferred from pressure change alone[3]	"	0.584	0.660	
5	S_g from ∇p data[3]	"	0.341	0.451	0.520
6	Ave. S_g from ∇p data (Row 5)	"		0.437	
7	core-ave. S_g from core wt.	"		0.654	

[1] - inferred from ∇p data and $k_{rw}(S_w)$ from Eq. 5.1

[2] - from ∇p data

[3] - assuming all gas in present as dissolution wave exits section 2 (line 1) is trapped and is altered only by change in pressure. This only makes sense for sections 1 and 2; in section 3, dissolution is reducing S_g

Table 5.4 Effect of compression on gas saturation at start of liquid injection (Experiment II)

		notes	Sect. 1	Sect. 2	Sect. 3
1	S_g from ∇p data[1]	s.s. foam (10-16 PV)	0.727	0.727	0.747
2	ave. p (psi)[2]	"	182	172	158.5
3	ave. p (psi)[2]	end transition (16.3 PV)	228	212	186
4	ratio of pressures before and after transition		0.798	0.811	0.852
5	S_g inferred from p change alone[3]	end transition (16.3 PV)	0.580	0.590	0.636
6	S_g from ∇p data[1]	"	0.542	0.571	0.589
7	core-ave. S_g inferred from pressure change alone (row 5)	"	0.602		
8	core-ave. S_g from ∇p data (row 6)	"	0.567		
9	core-ave. S_g from core wt.	"	0.543		

[1] - inferred from ∇p data and $k_{rw}(S_w)$ from Eq. 5.1

[2] - from ∇p data

[3] - assuming all gas in s.s. foam (line 1) is trapped and is compressed by change in pressure

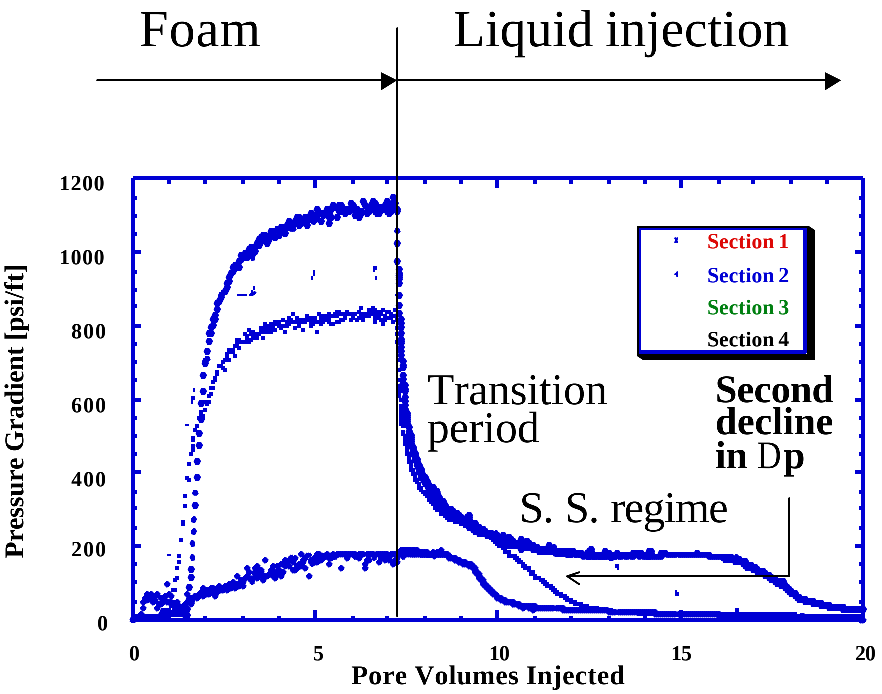

Figure 5.1. A typical result of a post-foam liquid-injection experiment (after Kibodeaux *et al*., 1994).

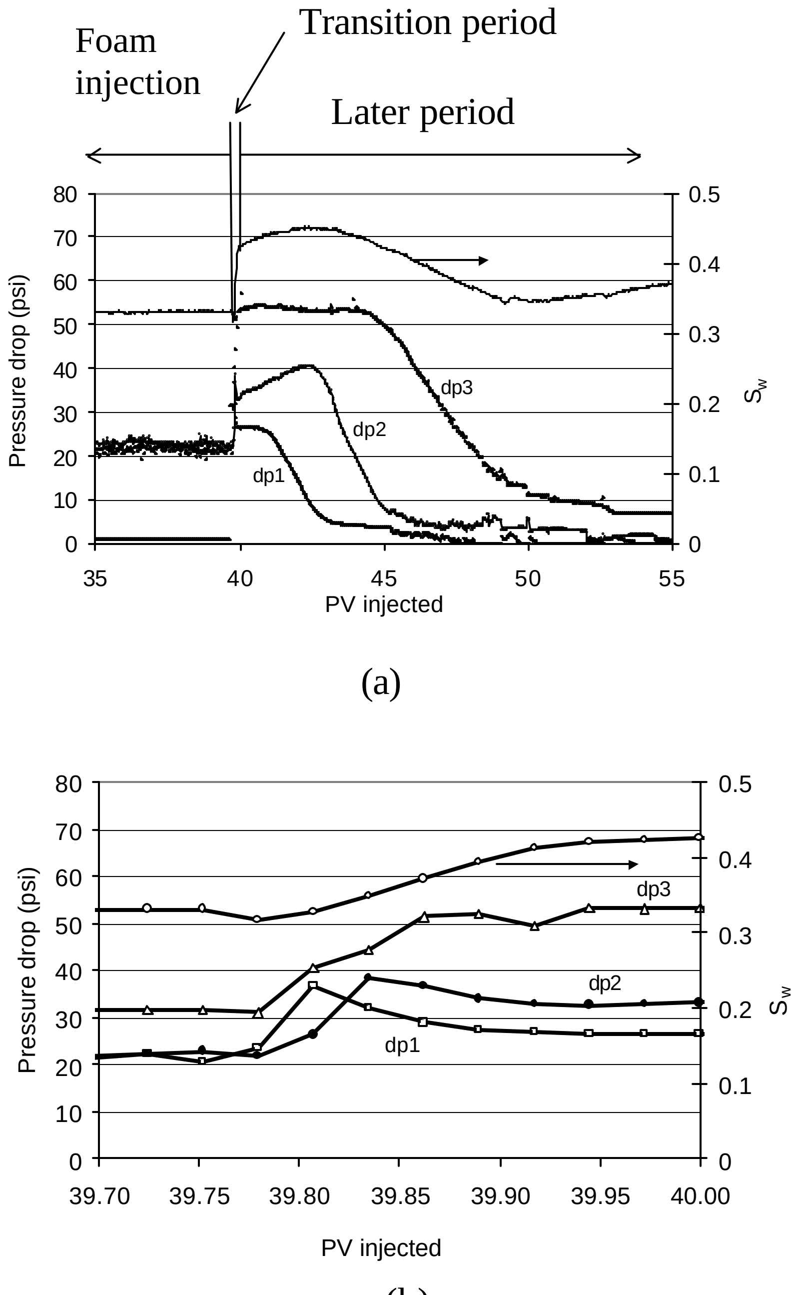

(a)

(b)

Figure 5.2 (a) Results of Experiment I. (b) Expanded view of the transition period. Each 0.1 PV injected corresponds to 7.25 minutes.

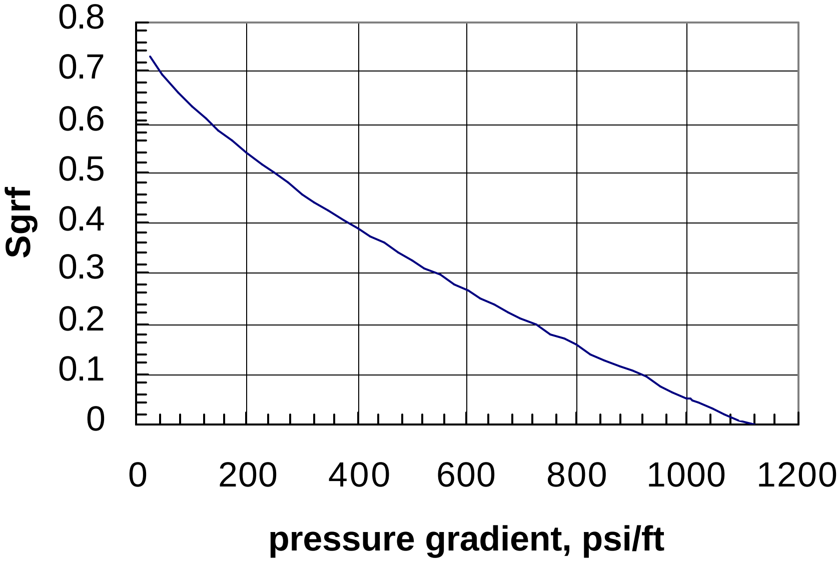

Figure 5.3 Trapped-gas saturation S_{gr}^{f} as a function of pressure gradient ∇p, from Cheng *et al.* (2002).

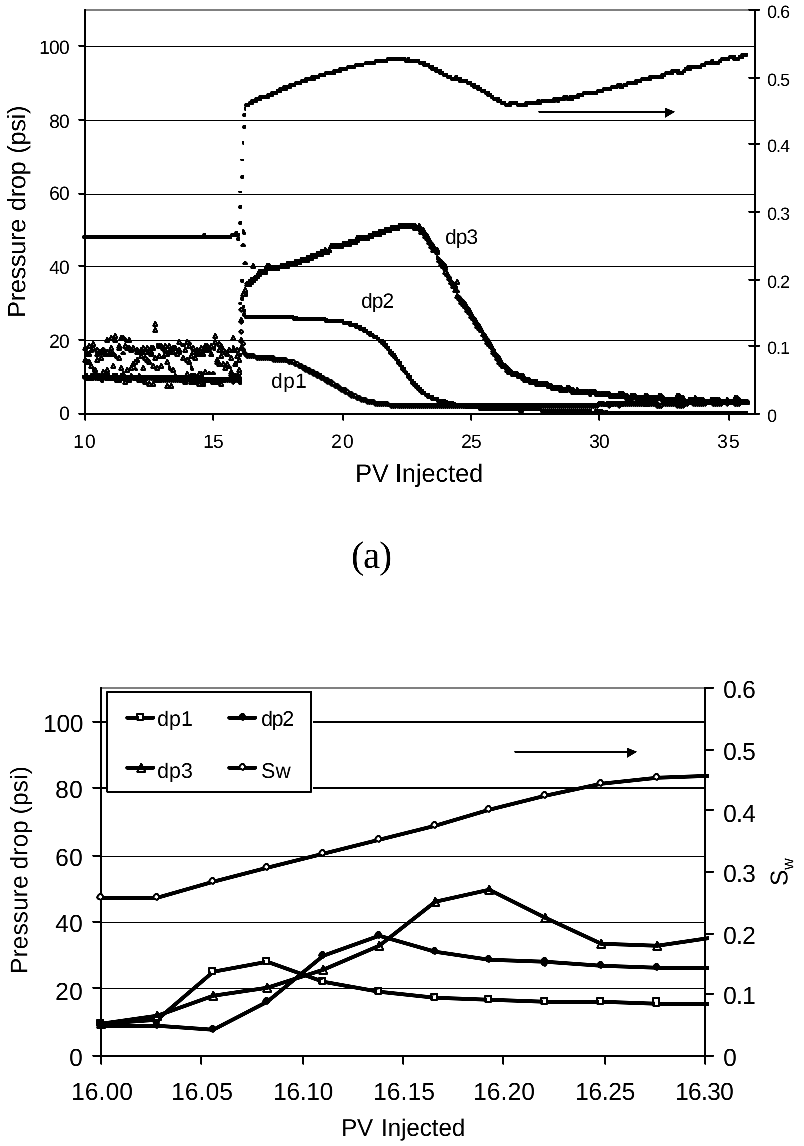

(a)

(b)

Figure 5.4 (a) Results of Experiment II. (b) Expanded view of the transition period. Each PV injected corresponds to 7.25 minutes.

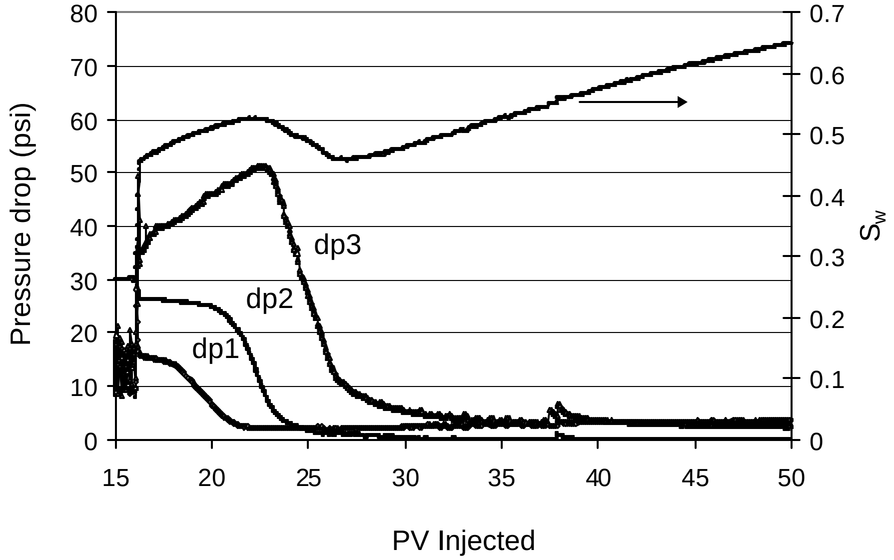

Figure 5.5 Late-time saturation increase in Experiment II.

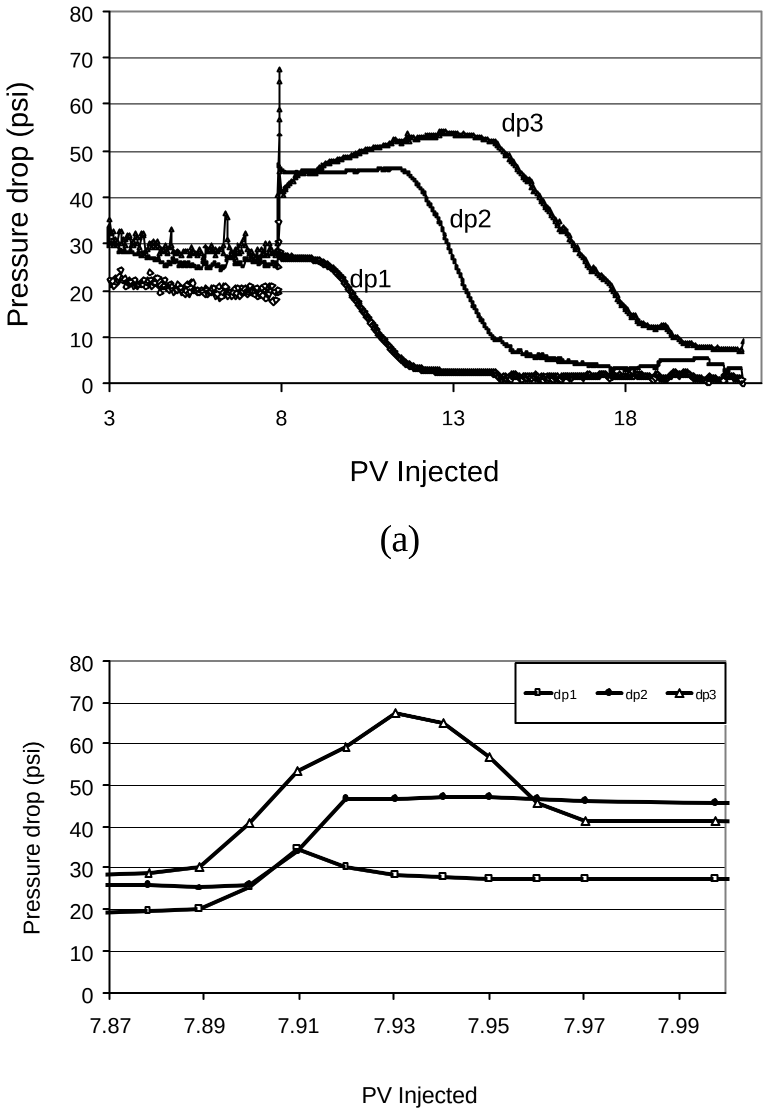

(a)

(b)

Figure 5.6 (a) Results of Experiment III. (b) Expanded view of the transition period. Each 0.1 PV injected corresponds to 7.25 minutes.

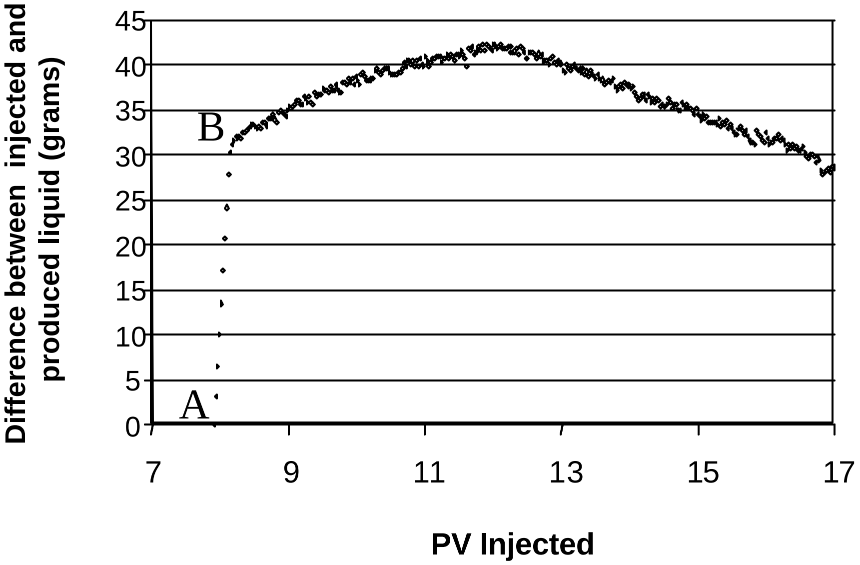

Figure 5.7 Measurement of the effluent liquid in Experiment III.

Chapter 6: Conclusions and Recommendations

This dissertation includes foam studies at disparate scales, with disparate goals. Chapter 2 is an attempt to better understand the microscopic mechanisms of foam apparent viscosity. Once quantified, the algorithm for apparent gas viscosity in foam would form a part of a much larger fully mechanistic simulation model for foam. The fruits of this work can be fully realized only in the context of that fully mechanistic foam simulator, which is beyond the scope of this study. Chapters 3 through 5 describe two experimental studies designed to answer specific questions important to foam applications for EOR and acid diversion: specifically, does foam completely collapse at a single limiting capillary pressure or water saturation in a foam SAG process for EOR; and what are the extents of gas trapping and rise in liquid mobility during acid injection in foam-acid diversion.

Below are some further reflections on these studies and suggestions for further work.

Foam reduces gas mobility by trapping some gas and resisting the flow of the gas that does flow. The latter is studied in Chapter 2 in the context of a simplified 2D model.

The most important simplification of the model in Chapter 2 (besides its 2D geometry) is the assumption of a single pore size. As a first-order correction, one could average the behavior of foam in variety of pores thought to characterize the pores through which foam flows in the porous medium. As noted in Chapter 2, the transition in behavior, with the drop in pressure gradient, would occur in different velocities in different pores. Averaged over many pores, one would expect to observe strongly shear-thinning behavior but probably not an actual drop in pressure gradient with an increase in flow rate.

Possible further refinements to the model are as follows: A bubble-train model that includes multiple pores and multiple lamellae, and bubbles of different volumes between then, can be developed using the method of Chapter 2. A more realistic pore geometry could be introduced to represent the porous medium. At this point, there is no quantitative relationship between the pore-size distribution of the medium as a whole and the pores through which the bubble train flows. One could include the effect of gas compressibility using method developed by Rossen (1990b). Such a simulation would require much more computing power and time, but is feasible in principle with a similar numerical approach to that used in this study.

This bubble-train model for apparent gas viscosity could form a part of a fully mechanistic foam simulator. With a realistic value of K, description of pore shapes, and pore-size distribution along the bubble train, the effective yield stress for gas can be determined. Even with this model, solving for gas flow rate as a function of pressure gradient is complex. As pressure gradient increases, gas is mobilized in more pores, which opens more pores to flow but also changes the size distribution of the pores through which foam flows. Current versions of fully mechanistic models use plausible but empirical expressions for effective gas relative permeability and viscosity with foam, which attempt to address the two issues of yield stress and effective viscosity of flowing gas. Making the gas-mobility algorithm in such a model truly fully mechanistic would be a complex task. A fully mechanistic model must of course also include the mechanisms of lamella generation and rupture to determine number and locations of lamellae in the pore space.

To verify the theoretical results, one would need a microscopic laboratory pore model in which pressure drop across the curved lamella is large enough to be measurable. In such a microscopic-model experiment, the value of K, which characterizes viscous drag of the Plateau border, could be obtained experimentally with a second experiment in a straight capillary tube, but only if one knows the width of the Plateau border and can keep it constant in both experiments. In principle the experimental results could then be compared quantitatively to the model.

SAG injection is a promising means of foam injection for EOR. Although the laboratory conditions in Chapter 4 differ from reservoir conditions, the study demonstrates a laboratory method for evaluating a SAG process for field applications. In particular, the technique can answer the question of whether foam collapses at a fixed water saturation and capillary pressure or over a range of water saturations. The answer to this question is crucial to success with a SAG process.

The experimental results of Chapter 4 indicate good injectivity for the SAG process under the laboratory conditions. It also suggests success in mobility control in a homogeneous reservoir, as indicated by the fractional-flow predictions based on the data. It is important to determine the effectiveness of foam in rocks of varying permeability, however, to predict the success of a SAG process in heterogeneous reservoirs. In a gas-injection EOR process, reservoir heterogeneity is often the reason for poor sweep efficiency.

It is pointed out in Chapter 4 that total superficial velocity of injected fluids should be kept constant in future experiments to allow a more reliable fractional-flow prediction based on the data. Also, the core should be vacuum-saturated with brine at the start of each experiment, to give greater confidence in the overall saturation during the experiment.

The study of post-foam liquid injection found a larger initial change in liquid saturation than expected and also an increase rather than a decrease in pressure gradient during liquid injection. There was also a rise, then fall, then rise in average liquid saturation in the core that was unexpected but that can be rationalized as the results of gas trapping and expansion as pressure varies in the core. The rise in pressure gradient during liquid injection may be favorable for the success of foam-acid injection. Kibodeaux *et al*. (1994) concluded that the fall in pressure gradient they observed during liquid injection was detrimental to foam effectiveness.

It is not clear to what extent the unexpected results may reflect the use of a weaker foam in these experiments than in those of Kibodeaux *et al*. On the other hand, one could argue that foam is usually weaker in the field than in laboratory experiments, so use of a weaker foam here may actually better reflect field conditions than use of a stronger foam in the laboratory.

Gas expansion and dissolution had surprising effects in our experimental results in Chapter 5, especially in the later period. Since gas doesn't expand very much at the high pressures in the field, higher back-pressure in the laboratory should be used if the apparatus allows. The effect of gas dissolution is not fully understood. In the laboratory, properly pre-saturating injected liquid with gas can help to eliminate this effect, although it is not simple to inject just the right amount of gas. In the field, the problems of gas dissolution could be avoided by injecting a small fraction of gas with the post-foam acid. The effects of gas dissolution cannot be eliminated entirely in the laboratory, because pressure varies along the core. If sufficient gas is included to saturate the core at the inlet pressure, then some of this gas will come out of solution at lower pressure downstream.

In the future, it would be useful to combine results from the method of weighing the core used here to CT or MRI scans of the same core material in similar experiments. The CT and MRI scans would allow resolution of the distribution of liquid saturation in the core. For instance, we conjecture in Chapter 5 that liquid saturation is non-uniform during the period of gas dissolution late in the experiment. CT or MRI scans could resolve this question.

Appendices

Appendix A. Value of K'

Hirasaki and Lawson (1985) derive the apparent viscosity of foams in cylindrical capillary tubes

$$\mu_{app} = \mu L_s n_L + \left(0.85 \frac{(\mu n_L R)}{(r_c/R)} (3\mu U/\sigma)^{-1/3} [(r_c/R)^2 + 1] \right) + \left((\mu n_L R)\, (3\mu U/\sigma)^{-1/3} \sqrt{N_s}\, \frac{(1 - e^{-N_L})}{(1 + e^{-N_L})} \right) \qquad \text{(A1)}$$

where L_s, R, and r_c are the length of liquid slug, radius of the capillary tube and radius of curvature of gas-liquid interface (Plateau border), respectively; n_L is the number of lamella per unit length; U is the velocity of bubbles; and N_s and N_L are dimensionless groups. The three terms in Eq. A1 represent three sources of resistance, namely, the liquid slug, the distortion of the interface under flow, and surface-tension gradients. In the thin-film limit, the liquid slug shrinks to zero thickness; *i.e.* $L_s = 0$. Therefore, the first term in the equation disappears, and Eq. A1 becomes

$$\mu_{app} = \left(0.85 \frac{(\mu n_L R)}{(r_c/R)} (3\mu/\sigma)^{-1/3} [(r_c/R)^2 + 1] + (\mu n_L R)\, (3\mu/\sigma)^{-1/3} \sqrt{N_s}\, \frac{(1 - e^{-N_L})}{(1 + e^{-N_L})} \right) U^{-1/3} \qquad \text{(A2)}$$

Thus $\mu_{app} \propto U^{-1/3}$. From the definition of apparent viscosity (Hirasaki and Lawson, 1985),

$$\mu_{app} = R^2 \nabla p/(8\ U), \tag{A3}$$

with

$$\nabla p = n_L\ \Delta p; \tag{A4}$$

we have

$$\Delta p = 8U\mu_{app}/(R^2 n_L)\ . \tag{A5}$$

By inserting μ_{app} in Eq. A2 and $\Delta p_D \equiv (\Delta p) / (\sigma/R)$ into Eq. A5 one gets

$$(\Delta p)_D = K'(U)^{2/3}$$

with

$$\begin{aligned}
K' &= 8/(R^2 n_L)/(\sigma/R)\left(0.85\frac{\mu n_L R}{(r_c/R)}(3\mu/\sigma)^{-1/3}[(r_c/R)^2+1]+(\mu n_L R)\,(3\mu/\sigma)^{-1/3}\sqrt{N_s}\,\frac{(1-e^{-N_L})}{(1+e^{-N_L})}\right)\\
&=(8\mu/\sigma)\left(\frac{0.85}{(r_c/R)}(3\mu/\sigma)^{-1/3}[(r_c/R)^2+1]+(3\mu/\sigma)^{-1/3}\sqrt{N_s}\,\frac{(1-e^{-N_L})}{(1+e^{-N_L})}\right)\\
&=8(3)^{-1/3}(\mu/\sigma)^{2/3}\left(\frac{0.85}{(r_c/R)}[(r_c/R)^2+1]+\sqrt{N_s}\,\frac{(1-e^{-N_L})}{(1+e^{-N_L})}\right)
\end{aligned} \tag{A6}$$

The value of K' is sensitive to r_c and R. As an example, we assume $R = 10^{-4}$ m, $r_c = 0.1R$, equivalent bubble radius $r_B = 3R$, $\mu = 0.001$Pa s and $\sigma = 30$ mN/m. This implies a value of capillary pressure $P_c \approx 3{,}000$ Pa. Then foam quality in gas-filled pores can be determined by Eq. A7:

$$r_c/R = \left(\frac{1}{3(1-\pi/4)}\frac{1-\Gamma}{\Gamma}\right)^{1/2}\left(\frac{r_B}{R}\right)^{3/2} , \qquad \text{(A7)}$$

which gives $\Gamma = 99.975\%$.

In Eq. A6, $N_s = \eta/r_c$, where the empirical factor $\eta = 0.05$ m (Hirasaki and Lawson, 1985). For long bubbles, $N_L>5$, so $\left((1-e^{-N_L})\big/(1+e^{-N_L})\right) \approx 1$. Thus we have:

$K' \approx 44.9\ (s/m)^{2/3}$.

For comparison, if $R = 10^{-5}$ and $r_c = 0.1R$, which implies a value of capillary pressure $P_c \approx 30{,}000$ Pa, keeping all other parameters unchanged from the previous case, we get

$K' \approx 131.7\ (s/m)^{2/3}$.

With $R = 10^{-3}$ m, a value which is close to capillary-tube radius in Hirasaki and Lawson's experiments, and with $\Gamma = 99.0\ \%$, $r_B= 3R$, one gets

$K' \approx 5.79\ (s/m)^{2/3}$.

The model of Ratulowski and Chang (1989) gives

$$\Delta p_D = 9.4\ (\mu V/\sigma)^{2/3} \qquad \text{(A8)}$$

at low Ca. Taking same parameter values for μ and σ as above, we have

$K' = 9.4\ (\mu/\sigma)^{2/3}$

$= 0.973\ (s/m)^{2/3}$.

The model of Wong *et al*. (1995) gives

$$(\Delta p)_D = p_b - p_f = (C_D/A)\,Ca^{2/3} \qquad \text{(A9)}$$

(C_D/A) is a parameter that depends on capillary-tube geometry. For a tube of circular cross-section, $(C_D/A) = 10.02$ and $(\Delta p)_D = 10.02\,Ca^{2/3}$. Again taking the same parameters for μ and σ as above, we have:

$$K' = ((10.02)\,(\mu/\sigma\,)^{2/3}$$
$$= 1.037\ (s/m)^{2/3}\,.$$

The model of Kovscek *et al*. (1995) gives

$$\mu_f = \mu_g + \frac{a\ n_f}{v_f^c}, \qquad \text{(A10)}$$

where μ_f is apparent viscosity, μ_g is gas viscosity, n_f is number density of lamellae, v_f is interstitial gas velocity and α and c are parameters. c is taken as 1/3 in their model based on Hirasaki and Lawson (1985). In the case of a strong foam, μ_g is relatively small and can be neglected. To derive K' from Eq. A10, applying this equation to a buddle-of-capillary-tubes model with radius R, we have:

$$\frac{\nabla p R^2}{8 v_f} = \frac{\alpha n_f}{v_f^c}$$

$$\nabla p = \frac{8\alpha n_f}{R^2} v_f^{2/3}$$

$$\Delta pn_L = \frac{8\alpha n_L}{R^2 \pi R^2} v_f^{2/3}$$

$$\Delta p = \frac{8\alpha}{\pi R^4} v_f^{2/3}$$

$$(\Delta p)_D = \frac{8\alpha}{\pi \sigma R^3} v_f^{2/3}$$

$$K' = \frac{8\alpha}{\pi \sigma R^3} \ .$$

Taking σ =30 mN/m, R = 10^{-4} m, and α = 8.6 E-16 Pa $s^{2/3}$ $m^{10/3}$ (from the fit to coreflood data of Kavscek, *et al*. (1995)), K' = 0.073 $(s/m)^{2/3}$. Value of K' derived from this model is very sensitive to the value of R, the capillary radius, however. Taking R=10^{-5} m instead, for instance, K'=73. since this model is fit to coreflood data and not derived for tube flow, there is no unique value of R.

Appendix B. Stability of symmetric lamella shape

Referring to Figure 2.12, consider how θ_1 and θ_2 change under a small perturbation $\Delta x = x_1 - x_2 > 0$. Assume that initially the lamella is at a symmetric position ($x_1 = x_2$) on the straight converging pore wall. θ_1 and θ_2 change with the inclination of the lamella arc induced by the perturbation, which is

$$P \equiv \arctan(\Delta x/(y_1 - y_2)) \ .$$

From the geometric relation in Figure 2.12(a), we have

$$\theta_{12} + \gamma/2 = \lambda_a + P \quad \text{(B1)}$$

$$\theta_{22} + \gamma/2 + P = \lambda_a \quad \text{(B2)}$$

where λ_a is the angle between pore-wall direction and a vertical line, equal to $(\beta + \pi/2)$. From eqs. B1 and B2, we have

$$\theta_{12}\text{-}\theta_{22} = 2\ P > 0 \quad . \qquad \text{(B3)}$$

Therefore Plateau border 2 will advance faster than Plateau border 1 in the next time step, and the perturbation is suppressed. The above derivation is conducted on the diverging portion of the pore, but it is also valid for the converging portion of the pore due to the symmetry. Therefore, the symmetric lamella shape at pore wall is intrinsically stable on the straight portions of the pore wall.

In Figure 2.12(b), at the pore corner, in addition to the above, pore-wall direction changes, and this affects θ_1 and θ_2. The equation for y(x) along the pore-wall in the corner region is given by

$$y = R_b - 2\varepsilon(R_b - R) + [4e\,(R_b - R)/\pi]\sin[(x/L - (0.5 - e))p/(2e)]. \qquad \text{(B4)}$$

Therefore

$$y' = \tan(\beta)\cos[(x/L - (0.5 - e))p/(2e)]$$
$$y'' = -\tan(\beta)\pi/(2L\,\varepsilon)\sin[(x/L - (0.5 - e))p/(2e)]$$
$$y''' = -\tan(\beta)\,(\pi/(2L\,\varepsilon))^2\cos[(x/L - (0.5 - e))p/(2e)] \ .$$

Also

$$a \equiv \arctan(y')$$

is the angle of the tangent to the pore wall to the x axis; then

$$d\alpha/dx = (y''/(1 + (y')^2)), \qquad \text{(B5)}$$

$$d^2a/dx^2 = y'''/(1 + (y')^2) - y''2y'y''/((1 + (y')^2)^2. \qquad \text{(B6)}$$

As the two Plateau borders enter the rounded region, θ_1 and θ_2 change not only with P, but also with the change of the pore-wall direction, N. Over a small perturbation Δx, the total change of pore-wall direction is

$$N = \int \mathrm{abs}(d\alpha/dx)\, dx \approx \mathrm{abs}\,(y(\xi)'/(1+(y(\xi)')^2))\,\Delta x, \qquad \text{(B7)}$$

where $x_1 < \xi < (x_1+\Delta x)$. Under this perturbation, the angle θ_1 decreases by N due to the change in pore-wall direction. Similarly,

$$\theta_{12} + N + \gamma/2 = \lambda_b + P \qquad \text{(B8)}$$

$$\theta_{22} + \gamma/2 = \lambda_b - P\ . \qquad \text{(B9)}$$

From eqs. B8 and B9, we have

$$\theta_{12} - \theta_{22} = 2\,P - N \qquad \text{(B10)}$$

$$= 2\arctan(\Delta x/(y_1-y_2)) - \int \mathrm{abs}(d\alpha/dx)\, dx$$

$$\approx (2/(y_1-y_2) - \mathrm{abs}(y'/(1+(y')^2)))\,\Delta x\ . \qquad \text{(B11)}$$

This is the net difference between θ_1 and θ_2 after a small perturbation, and it depends only on pore geometry. Since N equals zero when both Plateau borders are on the straight portion of the pore wall, eqs. B3 and B10 are consistent and Eq. B10 applies under all conditions. If the expression in Eq. B10 is less than zero, it means that Plateau border 1 moves faster than Plateau border 2 in the next time step, the separation of Plateau borders becomes greater, and the symmetric shape is unstable at this point. If the value is greater than zero, the tendency is that the existing perturbation will be suppressed and therefore the symmetric lamella sequence is stable at this point.

When Plateau border 1 is in the first half of the rounded corner region as shown in Figure 2.12(b), i.e. when

$$0 < [(x_1/L) - (0.5 - e)] < e,$$

the term inside the sin or cos in the derivatives after Eq. B4 varies from 0 to $\pi/2$. Thus, the expression in eqs. B5 and B6 is less than zero, and $d\alpha/dx$ is monotonically decreasing with increasing x, *i.e.* abs($d\alpha/dx$) is increasing in this range. This means the pore-wall direction changes more quickly as the Plateau border moves closer to the center of the pore.

Since $x_1 = 0.5$ L gives the maximum value to abs($d\alpha/dx$), or maximum asymmetric driving force N, for a sinusoidal pore-wall at the pore-body, the mid-point is the most unstable point. Therefore, if (2P-N) > 0 at this point, then (2P–N) > 0 throughout the pore and lamella symmetric sequence shape is stable, as in case of $\varepsilon > 0.20$, $\beta = 22.5°$, R/L = 0.125.

The term $[2/(y_1-y_2)]$ in Eq. B11 increases stability. The factor (y_1-y_2) closely relates to pore-body width. Therefore, the bigger the pore width, the smaller the value and the less stable the lamella is, and vice-versa. The sharper the corner (smaller ε, larger β, or larger $d\alpha/dx$), the larger is N and the greater the instability near the center of the pore.

Appendix C. Energy and work calculations

An apparent paradox of the analysis of $(\Delta p_D)^{ave}$ from plots like Figure 2.4(c) is that the net work required to push the lamella through the pore is the integral $\int \Delta p \, dv$, where v is volume behind a lamella; this implies that work is lost continuously. But in the quasi-static limit one senses that the energy dissipates in jumps, when $\delta v = 0$. Here we show that the energy dissipated in the jumps results from the instantaneous reduction in lamella area at the jump with no useful work derived, and that this is the same as $\int \Delta p \, dv$ for passage through the pore. For simplicity we limit our scope to wedge-shaped (2D) pores with $\varepsilon = 0$. First we show that the reversible work is stored in lamella area, and then by implication, that work dissipation occurs when lamella the jumps to shapes of lower area with no useful work derived.

The net work done by the pistons equals $\int \Delta p \, dv$. The volume increment dv in the pore equals the volume increment of the piston, (2 R W V dt), where V is the piston advance velocity. Since (2 R W V) is a constant, the time-average pressure difference $(\Delta p_D)^{ave}$ is proportional to work done by the piston.

In quasi-static limit, other than at jumps, all processes are reversible, and the work done by the piston between any two positions a and b during smooth advance is equal to energy gain by the lamella. Work done can be written as:

$$w = \int_a^b ?\, p dv . \tag{C1}$$

For two sufficiently close positions c and d in the conical diverging section of the pore,

$$W ß r_d^{\,2} = W ß r_c^2 + \delta v$$
$$W ß (r_d^{\,2} - r_c^{\,2}) = \delta v$$
$$dv \approx 2W ß r dr \quad .$$

where W, and β are defined in Figure 2.2. For a cylindrical lamella, $\Delta p = 2\ \sigma/r$, and work done from arbitrary positions a to b is

$$w = \int_a^b \Delta p dv$$
$$= \int_a^b \frac{2s}{r} 2W ß\ rdr$$
$$= 2\ \sigma W\ (2\ ß r_b - 2ß\ r_a).$$

For a cylindrical lamella, its area is $2W\beta r$, so

$$w = 2s(A_b - A_a)\ . \tag{C2}$$

The factor 2 accounts for the two gas-liquid surfaces of lamella. Thus during the smooth reversible advance of the lamella in the diverging section of the pore, the work of the piston is stored in the area and surface tension of the lamella. Similarly, in the converging part of the pore, with $\Delta p < 0$, the energy released by decreasing lamella area is returned to the pistons.

The work done in the diverging portion of the pore (A-B in Figure 2.4(a)) is stored in the increase in lamella area from its minimum to its maximum value just before the jump. In quasi-static movement in a pore with a sharp corner ($\varepsilon = 0$), the lamella is flat in the asymmetric sequence of shapes (C-D) in Figure 2.4(a)); there is no change in lamella area there and also no work done. In the converging portion of the pore (E-F in Figure 2.4(a)), the work released is that from decreasing area from its value at point E to the same minimum at which it began. Therefore difference between work input and output equals surface tension times the change in lamella area at the jumps.

Appendix D. Solubility of N_2 in water

In Fogg and Gerrand (1991), a function relationship is given for solubility of N_2 in water. Solubility in mole fraction is

$$\text{Exp}\,[-107.176+4852.4/(T)+13.9321\ \ln(T)+0.97001\ \ln(p)-0.000483\ (p)] \tag{D1}$$

where T is absolute temperature; and p is pressure in unit of atm. Calculated solubility at room temperature (298 K^o or 25 C^o) and 1 atmosphere pressure is $1.01\text{x}\ 10^{-5}$ in mole fraction from Eq. D1, meaning 1.01×10^{-5} mole of N_2 dissolves into 1 mole of H_2O liquid.

N_2 molar mass is 28.01 and molar mass for water is 18. One kgmol N_2 corresponds to 22.4 m^3 at standard condition; whereas 1 kgmol water corresponds to 18 kg = 18,000 g = 18,000 cc in volume. Thus the volume solubility at 1 atmosphere pressure is,

$$1.01 \times 10^{-5} \times 22.4 \times 10^{6} / 18000 = 0.01256 = 12.5 \text{ cc/L} .$$

ince solubility increases almost linearly with pressure, a more general expression for solubility of N_2 gas in water is: 12.5 cc/L atm.

References

Aarra, M. G., Skauge, A., Soegnesand, S. and Stenhaug, M., "A foam pilot test aimed at reducing gas inflow in a production well at the Oseberg field," presented at the 8th European IOR Symposium, Vienna, Austria, May 1-17, (1995)

Akin, S., Demiral, M. R. B. and Okandan, E., "A novel method of porosity measurement utilizing computerized tomography," *In situ* **20**(4), 347-365 (1996)

Alvarez, J.M., Rivas, H., Rossen, W.R., "A unified model for steady-state foam behavior at high and low foam qualities," *SPE J* **6**(Sept. 2001), 325-333

Apaydin, O. G., and Kovscek, A. R., "Surfactant concentration and end effects on foam flow in porous media," *Transport in porous media* **43**: 511-536 (2001)

Bartko, K. M., Newhouse, D. P., Anderson C. A., and Treinen, R. J., "The use of CT scanning in the investigation of acid damage to sandstone core," SPE 30457, prepared for presentation at the SPE Annual technical conference & exhibition held in Dallas, U. S. A., 22-25 October (1995)

Bernadiner, M. G., Thompson, K. E., and Fogler, H. S., "Effect of foams used during carbonate acidizing," *SPEPE* (Nov. 1992) 350-356

Bernard, G. G., Holm, L. w., and Harvey, C. P., "Use of surfactant to reduce CO_2 mobility in oil displacement," *SPE J* (Aug. 1980) 281-292

Bernard, G.G., Holm, L.W. and Jacobs, W.L., "Effective of foam on trapped gas saturation and on permeability of porous media to water," *SPE J.* 295-300 (1965)

Bertin, H. J., and Quintard, M. Y., "Modeling transient foam flow in porous media using a bubble population correlation," SPE 49020, prepared for presentation at the 1998 SPE Annual Technical Conference and Exhibition held in New Orleans, Louisiana, 27-30 September (1998)

Bertin, H. J., Apaydin, O. G., and Kovscek, A. R., "Foam flow in heterogeneous porous media: Effect of crossflow," SPE 39678, prepared for presentation at the 1998 SPE/DOE improved oil recovery symposium held in Tulsa, Oklahoma, 19-22 April (1998)

Blaker, T, Aarra, M. G., Skauge, A., Rasmussen, L., Celius, H. K.Martinsen, H. A., and Vassenden, F., “Foam for gas mobility control in the Snorre field: The FAWAG project,” (SPE 78824), August 2002 *SPE Reservoir Evaluation & Engineering*, p317-323 (2002)

Blaker, T., Celius, H. K., Lie, T., Martinsen, H. A., Rasmussen, L. and Vassenden, F., (1999), “Foam for gas mobility control in the Snorre field: the FAWAG project,” SPE 56478, presented at the 1999 SPE Annual Technical Conference and Exhibition, Houston, TX, Oct. 3-6

Bretherton, F. P., “The motion of long bubbles in tubes,” *J. Fluid Mech.*, **10**, 166-188 (1961)

Buckley, S. E. and Leverett, M. C., “Mechanism of fluid displacement in sands,” *Trans., AIME* **146**, 107 (1941)

Chad, J., Matsalla, P. and Novosad, J.J., “Foam forming surfactants in pembina/Ostracod “G” pool,” presented at the 39th Annual technical meeting of the petroleum society of CIM held in Calgary, June 12-16, 1988

Chen, L. H., Lucas, L. R., Nogaret, L. A. D., Yang, H. D., and Kenyon, D. E., “Laboratory monitoring of surfactant imbibition using computerized tomography,” SPE 59006, prepared for presentation at the 2000 SPE international Petroleum Conference and exhibition in Mexico held in Villahermosa, Mexico, 1-3 February 2000

Cheng, L., Kam, S. I., Delshad, M. and Rossen, W.R., "Simulation of Dynamic Foam-Acid Diversion Processes," accepted by *SPE J* (2002)

Cheng, L., Reme, A. B., Shan, D., Coombe, D. A., and Rossen, W. R., "Simulating foam processes at high and low foam qualities," SPE 59287, presented at the 2000 SPE/DOE Symposium on Improved Oil Recovery, Tulsa, OK, 3-5 April (2000)

Chou, S. I., “Conditions for generating foam in porous media,” SPE 22628, presented at the 1991 SPE Annual Technical Conference and Exhibition, Dallas, Oct. 6-9 (1991)

Chou, S. I., “Conditions for generating foam in porous media,” SPE 22628, presented at the Annual Technical Conference and Exhibition of the SPE, Dallas (1995)

Chou, S. I., Jasek D. E. and Goodgame, J. A., (1992), “CO_2 foam field trial at north ward-estes,” SPE 24643, presented at the 1992 SPE conference, Washington, DC, October 5-7 (1992)

Chukwueke, V.O., Bouts, M.N., van Dijkum, C.E., “Gas shut-off foam treatments,” Proceedings of the 1998 11th Symposium on Improved Oil Recovery. Part 1 (of 2), Apr 19-22 1998, Tulsa, OK, USA, SPE 39650, p 459-472 (1998)

de Vries, A.S. and Wit, K., “Rheology of gas/water foam in the quality range relevant to steam foam,” *SPE Reservoir Eng.*, 185-192 (1990)

Donald, J. M., Miller, K. C, Graham, S. K., and Yang, C., “Application of X-Ray CT Scanning to determine gas/water relative permeabilities,” SPE 20494, *SPE formation evaluation*, September (1993)

Ettinger, R. A., and Radke, C. J., "The Influence of Texture on Steady Foam Flow in Berea Sandstone," *SPERE* (Feb. 1992) 83-90

Falls, A. H., Hirasaki, G. J., Patzek, T. W., Gauglitz, D. A., Miller, D. D., and Ratulowski, J., “Development of a mechanistic foam simulator: The population balance and generation by snap-off,” *SPERE* (Aug. 1988) 884-892

Falls, A.H., Musters, J.J., and Ratulowski, J.,”The apparent viscosity of foams in homogeneous bead packs,” *SPE Reservoir Eng.*, 155-164 (1989)

Fisher, A. W., Foulser, R. W. S., and Goodyear, S. G., “Mathematical modeling of foam flooding,” SPE 20195 presented at the 1990 SPE/DOE Symposium on Improved Oil Recovery, Tulsa, OK

Fogg, P.G.T. and Gerrand, W., “Solubility of gases in liquids,” John Wiley & Sons, Ltd. Baffins Lane, Chichester West Sussex PO 19 1UD, England (1991)

Friedmann, F. and Jensen, J.A., ”Some parameters influencing the formation and propagation of foams in porous media,” SPE 15087, SPE California Regional Meeting, Oakland, CA, (1986)

Friedmann, F., Chen, W.H. and Gauglitz, P.A., ’Experimental and simulation study of high-temperature foam displacement in porous media,” *SPE Reser. Eng.*, **6**, 37-45 (1991)

Gauglitz, P.A., Friedmann, F., Kam, S.I, and Rossen, W.R., “Foam generation in homogeneous porous media,” accepted by *Chem. Eng. Sci*. (2002)

Gdanski, R. D., (1993), "Experience and research show best designs for foam-diverted acidizing," *Oil and Gas Journal* (Sept. 6, 1993), 85

Gillis, J.V. and Radke, C.J., "A Dual-Gas Tracer Technique for Determining Trapped Gas Saturation during Steady Foam Flow in Porous Media," SPE 20519, presented at the 65th SPE Annual Technical Conference, New Orleans, LA September (1990)

Harris, P.C., (1992), "Application of foam fluids to minimize damage during fracturing," Proceedings of the International Meeting on Petroleum Engineering, Mar 24-27 1992, Beijing, China, p 673-678

Heller, J. P., "CO2 foams in enhanced oil recovery," In foams: Fundamentals and applications in the petroleum industry, Schramm, L. L. (ed.), *ACS advances in Chemistry Series*, 3, No. 242, Am. Chemical Soc., Washington, D. C. (1994)

Hill, A. D., and Rossen, W. R., "Fluid placement and diversion in matrix acidizing," SPE 27982, presented at the 1994 Tulsa/SPE Centennial Petroleum Eng. Symposium, Tulsa, OK., Aug. 29-31

Hirasaki, G. J. Miller, C. A., Szafranski, R. , Lawson, B. J., and Akiya, N., SPE International Symposium on Oilfield Chemistry, Houston, TX, 18-21 February 1997.

Hirasaki, G. J., (1989), "The steam foam process," *JPT* (May1989) 449-456

Hirasaki, G.J. and Lawson, J.B., "Mechanisms of Foam Flow in Porous Media: Apparent Viscosity in Smooth Capillaries," *SPE J*, 176, Trans., AIME 279 (1985)

Hoefner, M. L., Evans, E. M., Buckles, J. j., and Jones, T. A., "CO2 foam: Results from four developmental field trials," SPE/DOE 27787, presented at ninth symposium on Improved Oil Recovery, Tulsa, OK, April 17-20, (1994)

Holm, L. W., "Foam injection test in the Siggins field, Illinois," SPE 2750 presented at 40th Annual California Regional Fall Meeting, San Francisco, Nov. 6-7, (1969)

Huh, D.G. and Handy, L.L., "Comparison of Steady- and Unsteady-State Flow of Gas and Foaming Solution in Porous Media," *SPERE*, Feb., 77-84 (1989)

Islam, M. R., and Farouq Ali, S. SM., "Nummerical simulation of foam flow in porous media," *JCPT* (August 1990), 29, No 4, 47-51

Jonas, T. M., Chou, S. I., and Vasicek, S. L., “Evaluation of a CO_2 foam field trial: Rangely weber sand unit,” SPE 20468, presented at the 63th Annul Technical Conference and Exhibition, Houston, TX, Oct. 2-5, (1988)

Kam, S. I., and Rossen, W. R., “A model for foam generation in homogeneous media,” SPE 77689, prepared for presentation at the SPE Annual Technical Conference and Exhibition held in San Antonio, Texas, 29 September- 2 October (2002)

Kennedy, D. K., Kitziger, F. W., and Hall, B. E., “Case study on the effectiveness of nitrogen foams and water-zone diverting agents in multistage Matrix acid treatments,” *SPEPE* (May 1992) 203-211

Khatib, Z. J., Hirasaki, G. J., and Falls, A. H., “Effects of capillary pressure on coalescence and phase mobilities in foams flowing through porous media,” *SPE Reser. Engr.* (Aug. 1988), 919-926

Kibodeaux, K. R., and Rossen, W. R. “Coreflood study of surfactant-Alternating-Gas foam processes,” SPE 38318, prepared for presentation at the 1997 SPE Western Regional Meeting held in Long Beach, Californian, 25-27 June (1997)

Kibodeaux, K. R., Zeilinger, S. C., and Rossen, W. R., "Sensitivity Study of Foam Diversion Processes for Matrix Acidization," SPE 28550, Proc. 1994 SPE Annual Technical Conference and Exhibition, New Orleans, LA, Sept. 26-28, (1994)

Kovscek, A. R. and Radke, C. J., “Simulation of foam displacement in porous media,” SPE 26402, presented at the 1993 SPE Annual Technical Conference and Exhibition, Houston, TX, Oct. 3-6 (1993)

Kovscek, A. R., Patzek, T. W. and Radke, C.J., "A mechanistic population balance model for one-dimensional foam flow in Boise sandstone," *Chemical Engineering Science* **50**(23), p. 3783-3799 (1995)

Kovscek, A. R., Patzek, T. W., Radke, C. J., “Mechanistic foam flow simulation in heterogeneous and multi-dimensional porous media,” *SPE J.* Dec. 1997, 2, 511-526

Krause, R. E., Lane, R. H., Kuehne, D. L. and Bain, G. F., “Foam treatment of producing wells to increase oil production at Prudhoe Bay,” SPE 24191, presented at the SPE/DOE eighth symposium on EOR, Tulsa, OK, April 22-24, (1992)

Kuehne, D. L., Ehman, D. I., Emanuel, A. S., Magnani, C. F., “Design and evaluation of a Nitrogen-foam field trial,” *JPT* (1990), 504

Lake, L. W., "Enhanced oil recovery," Prentice Hall, Englewood Cliffs, NJ (1989)

Ligthelm, D.J., van Eijden, G.J.M., Gronsveld, J., "Gas shut off using foam: The solution for unwanted gas production?," SPE 65125, prepared for presentation at the 2000 SPE European Petroleum Conference held in Paris, France, 24-25 October (2000)

Liu, P. C. and Besserer, G. J., "Application of foam injection in Triassic pool, Canada: Laboratory and field test results," SPE 18080, presented at the 63th Annul Technical Conference and Exhibition, Houston, TX, Oct. 2-5, (1988)

Mamun, C. K., Rong, J. G., Kam, S. I., Liljestrand, H. M., and Rossen, W. R., "Extending foam technology from improved oil recovery to environmental remediation," SPE 77557, prepared for presentation at the SPE Annual Technical conference and Exhibition held in San Antonio, Texas, 29 Septermber-2 October (2002)

Marfoe, C. H., and Kazemi, H., "Numerical simulation of foam flow in porous media," SPE 16790, presented at the 1987 Annual Technical Conference and Exhibition of the SPE, Dallas, TX 27-30

Martin, F. D., Stevens, J. E. and Harpole, K. J., "CO_2 foa field test at the east vacuum Grayburg/San Andres Unit," *SPERE* (Nov. 1995), 266-272

Mattews, C. S., "Carbon dioxide flooding," in Enhanced oil recovery II, processes and operations, Donaldson, E. C., Chilingarian, G. V., and Yen, T. F. (eds.), Elsevier Science Publ. Co., New York, (1989)

Moritis, G., "California Steam EOR Produces Less; Other EOR Continues," *Oil Gas J*. (April 15, 2002), 43-47 and 71-83.

Myers, T. J., and Radke, C. J., "Transient foam displacement in the presence of residual oil: experiment and simulation using a population-balance model," SPE 56412, presented at the 1999 Annual Technical Conference and Exhibition of the SPE, Houston

Osterloh, W. T. and Jante, M. J., "Effects of gas and liquid velocity on steady-state foam flow at high temperature," SPE 24179, SPE/DOE on EOR, Tulsa, OK, April 22-24 (1992)

Parlar, M. Parris, M.D., Jasinski, R.J. and Robert, J.A., "An Experimental Study of Foam Flow through Berea Sandstone with Application to Foam Diversion in Matrix Acidizing," SPE 29678, presented at the SPE Western Regional Meeting, Bakersfield, CA, March 8-10 (1995)

Perry, R. H., and Chilton, C. H., eds., "Chemical Engineer's Handbook," 5th Ed., McGraw-Hill, New York, p. 3-211ff (1973)

Persoff, P., Radke, C. J., Pruess, K., Benson, S. M., and Witherspoon, P. A., “A laboratory investigation of foam flow in sandstone at elevated pressure,” *SPE Reservoir Eng*. (Aug. 1991) 6, 365-372

Picket, S.L.; Cole, S.W., “Foamed cementing technique for liners yields cost-effective results,” Proceedings of the Permian Basin Oil & Gas Recovery Conference, Mar 16-18 1994, Midland, TX, USA, p 523-529

Prieditis, J., and Paulett, G. S., “CO_2 foam mobility tests at reservoir conditions in San Andres Cores,” SPE/DOE 24178, presented at the 1992 SPE/DOE Symp. On EOR, Tulsa, OK, April 22-24

Ratulowski, J., Chang, H., “Transport of gas bubbles in capillaries,” *Phys. Fluids A* **1** (1989),1642-1655

Robert, J. A. and Rossen, W. R., “Fluid placement diversion and pumping strategy,” in M. J. Economides and N. G. Nolte, eds., *Reservoir Stimulation*, 3rd ed., Prentice Hall, Englewood Cliffs, NJ (1997)

Robert, J.A. and Mack, M.G., “Foam Diversion Modeling and Simulation,” SPE 29676, presented at SPE Western Regional Meeting, Bakersfield, CA, Mar. 8-10 (1995)

Rong, J. G., “Experimental evaluation of foam in environmental remediation,” Ph. D. dissertation, the University of Texas at Austin, (2002)

Rossen, W. R., “Theory of mobilization pressure gradient of flowing foams in porous media, I. Incompressible foam,” *J. Colloid Interface Sci*. **136**, 1-53. (1990a)

Rossen, W. R., “Theory of mobilization pressure gradient of flowing foams in porous media. II. Effect of compressibility,” *J. Colloid Interface Sci.* **136**, 1-53 (1990b)

Rossen, W. R. “Theory of mobilization pressure gradient of flowing foams in porous media. III. Asymmetric lamella shapes,” *J. Colloid Interface Sci.* **136**, 1-53. (1990c)

Rossen, W. R., “Theory of mobilization pressure gradient for foam flow in porous media: Effect of interactions with stationary lamellae,” *J. Colloid Interface Sci*. **139**, 457- 467 (1990d)

Rossen, W. R. and Gauglitz, P. A., (1990) “Percolation theory of creation and mobilization of foam in porous media,” *AIChE J*. **36** (1990), 1176-1188

Rossen, W. R.,"Theories of foam mobilization pressure gradient," Proc. SPE/DOE EOR Symp. Tulsa, OK, April 17-20. (1988)

Rossen, W. R., "Foams in enhanced oil recovery," in Foams: Theory, measurement, and applications, Prud'homme, R. K. and Khan, S. (eds.), Marcel Dekker, New York City (1996)

Rossen, W.R. and Wang, M.-W., "Modeling foams for acid diversion," *SPE J*, **4**, 92-100 (June 1999).

Rossen, W.R., Zhou, Z.H., "Modeling foam mobility at the 'limiting capillary pressure'," *SPE Advanced Technology Series*, **v3**, n1, Mar, 1995, p 146-153

Sanchez, J. M., and Schechter, R. S., "Surfactant effects on the two-phase flow of steam-water and Nitrogen-water through permeable media," *J. Petr. Sci. Eng.* **3**, 185-199, (1989)

Schramm, L. L. (Eds.): "Foams: Fundamentals and Applications in the Petroleum Industry," ACS Advances in Chemistry Series No. 242, Am. Chem. Soc., Washington, D. C. (1994)

Scott, S.L.; Wu, Y., and Bridges, T.J., "Air foam improves efficiency of completion and workover operations in low-pressure gas wells," *SPE Drilling and Completion*, **v10,** n4, Dec, 1995, p 219-225

Shan, D., "Simulation study of gravity override for foam processes," M. S. thesis, 2001, The University of Texas at Austin

Shan, D., and Rossen, W. R., "Optimal injection strategies for foam IOR," SPE 75180, prepared for presentation at the SPE/DOE Thirteenth Symposium on IOR held in Tulsa, Oklahoma, 13-17 April (2002)

Shi, J.-X., and Rossen, W. R., "Improved surfactant-alternating-gas foam process to control gravity override," SPE 39653, prepared for presentation at the 1998 SPE/DOE Improved Oil Recovery Symposium held in Tulsa, Oklahoma, 19-22 April (1998)

Skauge, A., Aarra, M. G., Surguchev, L., Martinsen, H. A., and Rasmussen, L., "Foam-Assisted WAG: Experience from the Snorre field," SPE 75157, prepared for presentation at the SPE/DOE Thirteenth Improved Oil Recovery Symposium held in Tulsa, Oklahoma, 13-17 April (2002)

Smith, C. L., Anderson, J. L., and Roberts, P. G., (1969), "New diverting techniques for acidizing and fracturing," SPE 2751, presented at 1969 Annual Technical Conference and Exhibition, San Francisco, CA, Nov. 6-7. (1969)

Svorstol, I., Vassenden, F., and Mannhardt, K., “Laboratory studies for design of a foam pilot in the Snorre field,” SPE/DOE 35400, presented at the 1996 SPE/DOE 10th symposium on Improved Oil Recovery, Tulsa, OK, April 21-24 (1996)

Techrob, R.R., and Manuel, J.J., “Underbalanced foam drilling reduces hole problems and costs,” Oil and Gas Journal, v 95, n 33, Aug 18, 1997, p 52-55

Thomas, R. L., Ali, S. A., Robert, J. A., and Acock, A. M., “Field validation of a foam diversion model: A matrix stimulation case study,” paper 39422, presented at the 1998 international symposium on formation damage control held in Lafayette, Louisiana, 18-19 February (1998)

Thompson, K. and Gdanski, R. D., “Laboratory study provides guidelines for diverting acid with foam,” *SPEPF* (Nov. 1993) 285

Toney, F.L., Mack, D.J., “Next generation of foam: A field study of Northwestern Oklahoma foam fracturing,” Proceedings of the SPE Production Operations Symposium, Apr 7-9 1991, Oklahoma City, OK, USA, p 113-123

Wassmuth, F. R., Green, K. A., and Randall, L.: "Details of in-situ foam propagation exposed with Magnetic Resonance Imaging," *SPEREE* (April 2001), 135-145

Wegener, D. C. and Harpole, K. J., “Determine of relative permeability and trapped gas saturation for predictions of WAG performance in the south Cowden CO_2 flood,” SPE/DOE 35429, this paper was selected for presentation at the 1996 SPE/DOE tenth Symposium on Improved Oil Recovery held in Tulsa OK, 21-24 April (1996)

Witteveld, A., "Analyses of Post-Foam Liquid Injection," unpublished student report, 1997

Wong, H. Radke, C. J., Morris, S., “The motion of log bubbles in polygonal capillaries. Part 2. Drag, fluid pressure and fluid flow,” *J. Fluid Mech.* **292** (1995) 95-110

Xu, Q. and Rossen, W.R., "Dynamic viscosity of foam in porous media," Proc. EuroConference on Foams, Emulsions and Applications, Delft, The Netherlands, 5-8 June (2000)

Xu, Q., and Rossen, W. R., "Effective viscosity of foams in periodically constricted tubes," *Colloids and Surfaces A*: Physicochem Eng. Aspects, in press (2003)

Yang, S. H. and Reed, R. L., “Mobility control using CO2 foams,” SPE 19689, presented at the 1989 SPE Annual Technical Conference and Exhibition, San Antonio, TX, Oct. 8-11 (1989)

Zeilinger, S. C., “A modeling and experimental study of foam in acid diversion and enhanced oil recovery,” Ph. D Thesis, The university of Texas at Austin (1996)

Zeilinger, S. C., Wang, M. Kibodeaux, K. R., and Rossen, W. R., "Improved Prediction of Foam Diversion in Matrix Acidization," SPE 29529, Proc. 1995 SPE Production Operations Symposium, Oklahoma City, OK, April 2-4, (1995)

Zerhboub, M., Touboul, E. and Ben Naceur, K., “Matrix acidizing: A novel approach to foam diversion,” *SPEPF* (May 1994) 121-126

Zhou, Z. H., Rossen, W.R., “Applying fractional-flow theory to foam processes at the 'limiting capillary pressure',” *SPE Advanced Technology Series*, **v3**,n1, Mar, 1995, p 154-162

Vita

Qiang Xu was born on September 18, 1964 in Jia county, China, to Fenglou Xu and Cuihua Yao. He graduated from Yulin high-school, Yulin, Shaanxi, China, in 1981. He went to Xian Jiaotong University, where he graduated in 1985 with a B.S. in mechanical engineering. He joined China National Petroleum Corporation from 1985 to 1996. During the time, he obtained M.S. in engineering mechanics in 1991 from Northwestern Polytechnical University in China. In 1996 Qiang Xu attended the University of Kentucky, then transferred to the University of Texas at Austin in 1998 to pursue a Ph.D. degree.

Permanent address: 119 North street, Yulin, Shaanxi, China

This dissertation was typed by the author.